Light scattering study of irregular particles with arbitrary size, shape, and complex refractive index

by

Prakash Gautam

M.Sc., Tribhuvan University, Nepal, 2015

AN ABSTRACT OF A DISSERTATION

submitted in partial fulfillment of the
requirements for the degree

DOCTOR OF PHILOSOPHY

Department of Physics
College of Arts and Science

KANSAS STATE UNIVERSITY
Manhattan, Kansas

2022

Abstract

We investigated light scattering due to irregularly shaped aerosol particles with diverse shapes, sizes, and complex refractive indices. We have designed and developed a light scattering setup based on a novel optical scheme that can detect light from 0.32° and 177.6°, from an extreme forward to the backscattering regime, involving 46 angles. Our setup was able to measure all six independent scattering matrix elements; however, we focused on measuring the scattering intensity and the linear depolarization ratio for different dust particles. Given the extremely small and large angles, the data obtained for our setup are plotted on both: versus scattering angle, θ linearly, and scattering wave vector, q or qR with R the radius of a particle, on a log-log scale, called θ and Q-space respectively. The Q-space analysis best represents the data at the extreme forward scattering regime; however, it compresses the data at the large scattering angles, θ , where useful data also reside. At large scattering angles, the scattered intensity is best viewed by θ-space analysis.

We scattered the light from different aerosol particles viz; silicon dioxide (SiO_2), aluminum abrasive (Al_2O_3), a highly refractive molybdenum disulfide (MoS_2), a highly absorptive hematite particle ($\alpha - Fe_2O_3$), arizona road dust and Soot particles. The measured scattered intensity was interpreted by applying both analysis methods. Light scattering for all particle types was compared to theoretical Mie scattering calculations using size distributions determined by an Aerodynamic Particle Sizer (APS 3321), an aerosol measuring instrument. The compared results between the experimentally measured data and Mie calculations showed a close agreement at the forward scattering regime and poorly at the side and backscattering regimes. Effects of the intensity-weighted size distribution were discussed. We applied Guinier analysis on light scattering measured data to compare light scattering inferred size to the intensity-weighted mean sizes for all shape particles. The

light scattering sizes were consistent with the intensity-weighted mean sizes of reasonable accuracy for any shape and refractive index. This result has demonstrated the importance of intensity weighting of the size distribution in light scattering.

We measured and studied the linear depolarization ratio for different dust particles. They all displayed a common pattern. The measured values were negligibly small at the forward scattering regime. They increased with increasing the scattering angle and reached a maximum at the side scattering regime that generally droped off at the backscattering regime. The effects of particle asphericity, size, and refractive index on the linear depolarization ratio were investigated.

We further investigate the light scattering from fractal soot and non-fractal hematite aggregates. The results showed an enhancement in the backscattering despite a large imaginary refractive index. We found that enhancement backscattering for the non-fractal aggregate is due to internal multiple scattering between the grains within the aggregate. In contrast, enhancement backscattering is yet to be understood for fractal soot aggregates. Furthermore, the results presented in this work showed the sensitive of light backscattering with the change in particles' shapes, sizes, and refractive indices and warn the experimentalist to use the backscattering measured data with great caution.

Light scattering study of irregular particles with arbitrary size, shape, and complex refractive index

by

Prakash Gautam

M.Sc., Tribhuvan University, Nepal, 2015

A DISSERTATION

submitted in partial fulfillment of the
requirements for the degree

DOCTOR OF PHILOSOPHY

Department of Physics
College of Arts and Sciences

KANSAS STATE UNIVERSITY
Manhattan, Kansas

2022

Approved by:

Major Professor
Dr. Christopher M. Sorensen

Copyright

Abstract

We investigated light scattering due to irregularly shaped aerosol particles with diverse shapes, sizes, and complex refractive indices. We have designed and developed a light scattering setup based on a novel optical scheme that can detect light from 0.32° and 177.6°, from an extreme forward to the backscattering regime, involving 46 angles. Our setup was able to measure all six independent scattering matrix elements; however, we focused on measuring the scattering intensity and the linear depolarization ratio for different dust particles. Given the extremely small and large angles, the data obtained for our setup are plotted on both: versus scattering angle, θ linearly, and scattering wave vector, q or qR with R the radius of a particle, on a log-log scale, called θ and Q-space respectively. The Q-space analysis best represents the data at the extreme forward scattering regime; however, it compresses the data at the large scattering angles, θ , where useful data also reside. At large scattering angles, the scattered intensity is best viewed by θ-space analysis.

We scattered the light from different aerosol particles viz; silicon dioxide (SiO_2), aluminum abrasive (Al_2O_3), a highly refractive molybdenum disulfide (MoS_2), a highly absorptive hematite particle ($\alpha - Fe_2O_3$), arizona road dust and Soot particles. The measured scattered intensity was interpreted by applying both analysis methods. Light scattering for all particle types was compared to theoretical Mie scattering calculations using size distributions determined by an Aerodynamic Particle Sizer (APS 3321), an aerosol measuring instrument. The compared results between the experimentally measured data and Mie calculations showed a close agreement at the forward scattering regime and poorly at the side and backscattering regimes. Effects of the intensity-weighted size distribution were discussed. We applied Guinier analysis on light scattering measured data to compare light scattering inferred size to the intensity-weighted mean sizes for all shape particles. The

light scattering sizes were consistent with the intensity-weighted mean sizes of reasonable accuracy for any shape and refractive index. This result has demonstrated the importance of intensity weighting of the size distribution in light scattering.

We measured and studied the linear depolarization ratio for different dust particles. They all displayed a common pattern. The measured values were negligibly small at the forward scattering regime. They increased with increasing the scattering angle and reached a maximum at the side scattering regime that generally droped off at the backscattering regime. The effects of particle asphericity, size, and refractive index on the linear depolarization ratio were investigated.

We further investigate the light scattering from fractal soot and non-fractal hematite aggregates. The results showed an enhancement in the backscattering despite a large imaginary refractive index. We found that enhancement backscattering for the non-fractal aggregate is due to internal multiple scattering between the grains within the aggregate. In contrast, enhancement backscattering is yet to be understood for fractal soot aggregates. Furthermore, the results presented in this work showed the sensitive of light backscattering with the change in particles' shapes, sizes, and refractive indices and warn the experimentalist to use the backscattering measured data with great caution.

Table of Contents

List of Figures

Acknowledgments

First and foremost, I would like to express my sincere gratitude to my advisor, Dr. Chris Sorensen, for providing the opportunity to grow as a researcher. You taught me how to see and solve a problem. Professor Chris, you are a model researcher, physicist, and a great human being. Your integrity, ability to deconstruct problems, and your creativity are inspiring. This research and dissertation would not have happened without your help, advice, expertise, and encouragement. Utmost respect!

I want to express my thanks to Assoc. Prof. Dr. Matthew Berg, Prof. Dr. Bret Flanders, and Prof. Dr. Terry Beck for being my committee members. Special thanks go to Dr. Berg for being always available and ready to help.

I want to thank Dr. Justin Maughan, a person of superior intellect, for his theoretical support of this work. Likewise, I would also like to thank Dr. Yuli Heinson and Dr. Raiya Ebini for their early experimental support. I would like to remember Mr. Blaine Fry like my own brother. Thank you so much for providing the company in and outside the lab. Likewise, I am thankful to my friend Dr. Bikash Bhandari, who gave important advice while writing the dissertation and for sharing his post-Ph.D. experience.

A bunch of thanks goes to the Department of Physics, Kansas State University (KSU), faculties and staffs, especially Kim Coy.

My special thanks go to Felisa Osburn and Jim, who acted as my guardian and remembered me on every special occasion. Thank you so much for your love and care.

I want to express my gratitude to my brother, Mr. Dipak Gautam, who has supported me in every step of my career. I would like to remember my maternal uncle, Mr. Kiran Basnet; without him, I could not be here. I would like to remember these kiddos, Karmista, Disam, and Pawan, whom I love the most. Similarly, I would like to remember the other

two lovely ladies, Bindra Basnet and Durga Gautam, who always cared for me like their kids.

Furthermore, I would love to remember Uncle Mr. Bhakta Bahadur Gautam, who always motivated me to do better in life. Likewise, I would love to remember Baje: Mr. Netra khatri, who motivated me to study hard. Most importantly, I would like to express my sincere gratitude to my primary school math teacher Mr. Devnarayan Chaudhary who taught me very first thing in mathematics "Numbers And Counting".

I thank my wife, Roshani Pokharel, for her love and care. Finally, I would like to acknowledge with gratitude, the support and love of my parents, Yaksha Gautam and Dambar Kumari Gautam, especially my mother, who did everything she could for my study. This is for you, Mamas. . .

Dedication

To My Family...

Chapter 1

Introduction

Light scattering is a physical process that involves the interaction of light with matter. The scattering of light gives rise to many spectacular phenomena such as the rainbow, glory, and the red hues of sunrise and sunset. In addition, it is an essential technique for *in-situ*, non-invasive, and real-time characterization of scattering particles. Thus, understanding light scattering phenomena is critical from intellectual and practical points of view. The study of how particles interact with light has been a subject of interest for many years. The very first known experimental study of light scattering was carried out by John Tyndall (1868) [1], who designed and performed an apparatus that explained why the sky is blue in the day but red at sunset. JW Strutt published important work on light scattering titled "Light from the sky and its polarization and color" in 1871 [2]. His theory explained light scattering by particles with sizes less than the wavelength of light used. Gustav Mie (1908) developed a well-known theory, called Mie theory, to study the light scattering due to spherical homogeneous particles for a wide range of sizes by solving Maxwell's equations [3]. A series of well-known books on light scattering was published by Kerker [4], van de Hulst [5], Bohren and Huffman [6], and recently from Mishchenko and Co. [7, 8].

Although light scattering from spherical particles was solved long ago and is well understood [3, 5–7], a coherent description and understanding of light scattering by irregularly

shaped particles has not been achieved. The aerosols in the atmosphere are primarily irregular in shape, viz., mineral dust, volcanic ash, snow and ice crystals, soot, soot coated with water, forest fires, interstellar dust particles, biological micro-organisms, pollens, etc. How they scatter and absorb light has implications for the radiative forcing component of climate models and satellite remote sensing.

For the past few decades, studies have been carried out for describing and calculating scattering from irregularly shaped particles, including aggregates, both fractal, and non-fractal. Despite significant advancement in theory, there are still has some limitations in the ability to simulate precisely the non-spherical shape and size of the atmospherically available aerosol particles. So, an experimentally designed setup can help measure the light scattering from any size, morphology, and complex refractive index of the particles. Many setups had already been built to perform an experimental study of light scattering from particles of arbitrary size and shape, but none could measure the scattered light throughout the whole scattering angular range, i.e., from an extreme forward scattering angle to the backscattering. This dissertation aims to develop a static light scattering setup that can cover a wide scattering angle range and study non-spherical particle light scattering. In static light scattering, the angle-dependent light pattern is measured and evaluated. Moreover, the light scattering pattern does not change over time. Therefore, it helps identify the shape, structure, size distributions, and concentrations of particles involved in the scattering based on the magnitude of the scattered intensity.

My work is mainly devoted to developing a setup that can measure the scattering intensity over a wide angular range and study the optical properties of particles with diverse sizes, shapes, and complex refractive indices. This includes measuring such particles' scattered intensity, and depolarization ratio. This was carried out by shining a laser beam through ensembles of particles. Since we obtain the data over a wide-angle range with this setup, we advocate plotting the scattering data linearly when plotting versus the scattering angle and logarithmically when plotting versus the scattering wave vector, q, a method that we

call Q-space analysis.

1.1 The Q-space Analysis of Scattering

The Q-space analysis is a new perspective on light scattering to view the angular scattering patterns. Generally, angular scattering patterns are plotted versus the scattering angle, θ, linearly. But this new perspective plots the scattered intensity versus the magnitude of the scattering wave vector q or dimensionless quantity qR, on a log-log scale. This method is called a "Q-space analysis". Here R represents the size of the scatterer. This method is not entirely new. It has a long application history to small-angle X-ray and neutron scattering [9–12]. Sorensen first applied it to Mie scattering from spheres and discovered a pattern in the scattering that involved power laws that had never been described before 1.1[13–15]. Not only for spherical particles, this analysis also proved to be useful in describing the scattering from non-spherical particle geometries [15–17].

Overall, the Q-space analysis method describes quantitatively how particles of all shapes and sizes scatter light. The significant difference between the θ-space analysis with the Q-space analysis lies in these two characteristics: 1) The magnitude of the scattering wave vector, q has the dimension of inverse length; hence can uncover length scales in the scattering object, whereas θ is dimensionless and thus has no such ability. 2) In Q-space analysis, we plot on a log-log scale, whereas linearly in θ-space. In general, plotting logarithmically uncovers the universe's geometric nature, which usually prevails over its arithmetic nature. Figure 1.1(b) shows an example of how the Q-space analysis can do a better job in illustrating the angular pattern of the light scattering over θ-space analysis. However, Q-space analysis misses the detail past 90°, such as the rainbows and glory.

On the other hand, the compression that Q-space provides at large θ accentuates the hump and demonstrates the ultimate approach to the Rayleigh-Debye-Gans (RDG) limit, i.e., 3d diffraction limit . It holds under the condition $kR|m-1| << 1$ where k, R, and

m are the wave vector, the overall size of the particle, and refractive index, respectively [5, 15, 18].

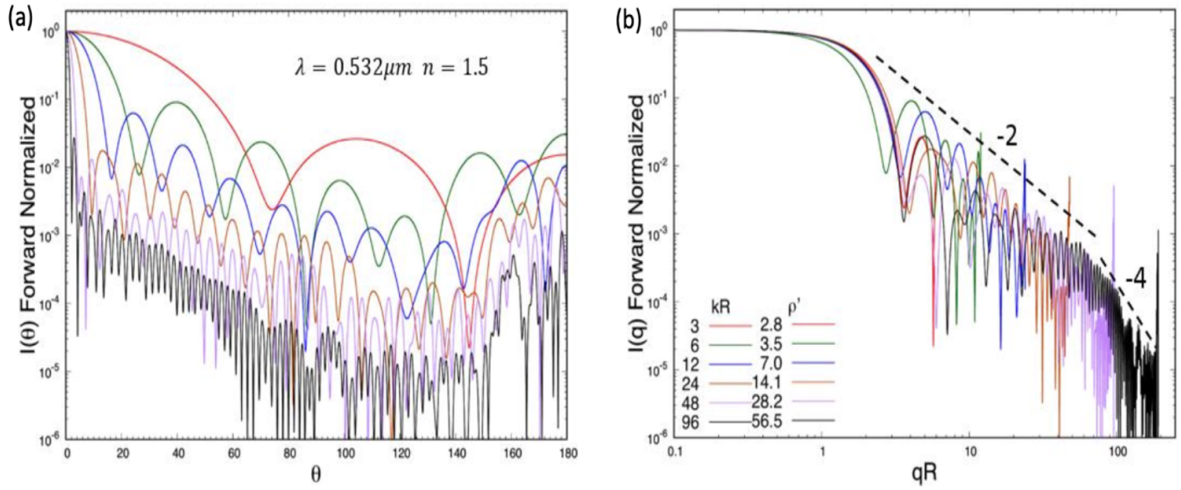

Figure 1.1: *Comparison of forward normalized scattered intensity for spheres with different sizes for the refractive index* $m = n+i\kappa = 1.5 + i0$*, plotted versus (a) conventional scattering angle,* θ *and (b) versus the dimensionless parameter* qR *called Q-space analysis [13]. Figure 1.1(a) shows no definable pattern, whereas 1.1(b) shows a forward scattering regime followed by a Guinier regime and a power-law regime with quantifiable exponents. The incident light is vertically polarized perpendicular to the scattering plane containing the scattering angle—the size parameters* $x = kR$ *ranging from 3 to 96 corresponding diameters* $\simeq$ *0.5 to 16 microns, respectively.*

Figure 1.1 shows forward normalized Mie scattering intensity (I(θ))/(I(0)) for vertically polarized incident light for a sphere with refractive index $m = n + i\kappa = 1.5 + 0$i and many spheres with different sizes kR. The same data is plotted versus scattering angle, θ (θ-space) and the dimensionless quantity qR (Q-space). Plotting versus the scattering angle, θ shows a series of bumps and wiggles with some periodicities but with no coherent pattern, whereas plotting versus the dimensionless quantity, qR logarithmically shows a

coherent pattern for the different size parameters. At small qR, the Q-space plot showed a universal "forward scattering lobe", followed by a Guinier regime near qR $\simeq$ 1, and power-law envelopes appear with -2 and -4 exponents at large qR. Finally, the enhanced backscattering, the "glory". A complete description of the Q-space uncovered pattern and its refinement would be obtained by the inclusion of the internal coupling parameter ρ', very similar to the phase shift parameter [19].

1.1.1 The Scattering Wave Vector

The foundation of the light scattering is found in the phase relations of the waves scattered from the different volume elements of the scattering objects. The phase relation between the incident wave and the scattered wave is given by the scattering wave vector, q, the fundamental Q-space analysis variable.

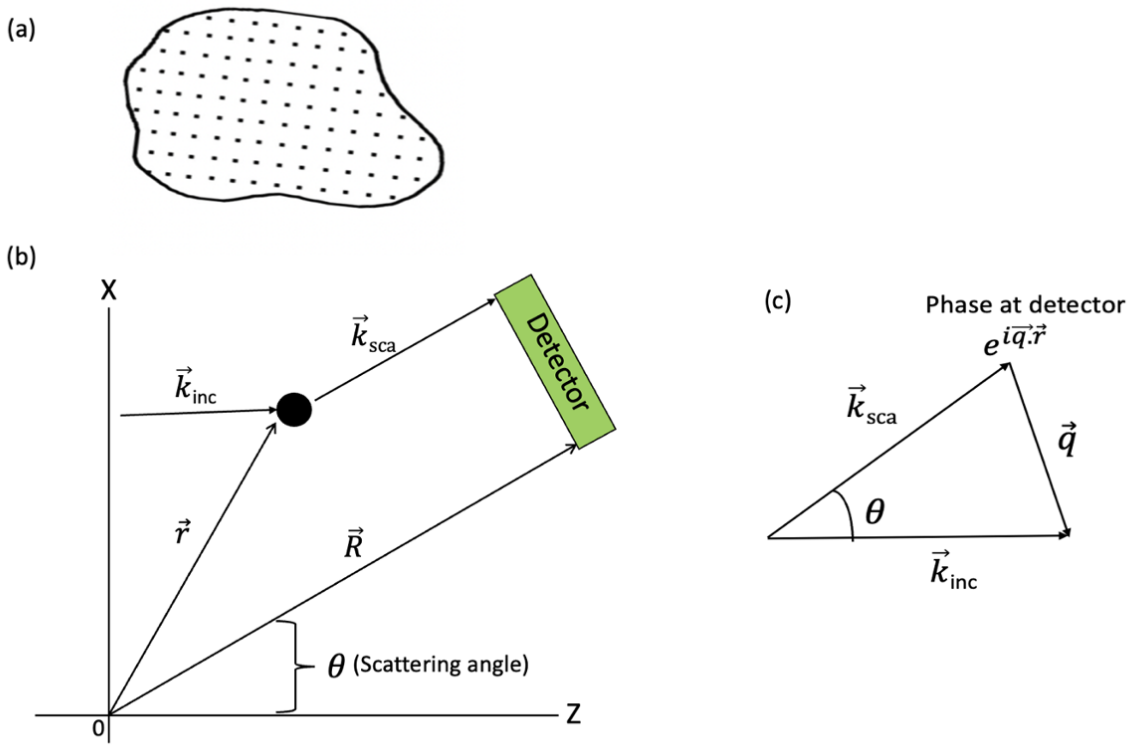

Figure 1.2: *Graphical representation of light scattering measurements (a) system of scatterers (b) light incident upon a point scatterer at $\vec{r}$ and then scattered towards a detector on the far-field at $\vec{R}$. (c) diagram of the scattering wave vector $\vec{q}$. The detector measures the scattered light in the direction, θ.*

Any particle can be represented by its geometric shape filled with the vacuum and point scatterers. Figure 1.2(a) is an example of an arbitrarily shaped object in which the point scatterers represent infinitesimal volume elements. Consider a light wave incident upon a point-like scatterer, at $\vec{r}$ as, drawn in Fig. 1.2(b). Since we assumed that the scatterer is point-like, it scatters light in the plane perpendicular to the incident polarization. The incident field at a position $\vec{r}$ can be written as

$$E(\vec{r}) = E_0 e^{i\vec{k_i}.\vec{r}} \tag{1.1}$$

where $\vec{k_i}$ is the incident wave vector that gives the direction of propagation of the incident wave, with magnitude $|\vec{k_i}| = 2\pi/\lambda$. The light is scattered off the particle towards a detector at position R from the origin, and the scattered wave vector describes its propagation $\vec{k_s}$ such that R >> r. Then the field at the detector is a plane wave given by

$$E(\vec{R}) \sim E(\vec{r}) e^{i\vec{k_s}.(\vec{R}-\vec{r})} \tag{1.2}$$

With the substitution of values of E($\vec{r}$) from Eq. 1.1 to 1.2

$$E(\vec{R}) \sim e^{i\vec{k_s}.\vec{R}} e^{i(\vec{k_i}-\vec{k_s}).\vec{r}} \tag{1.3}$$

Note that the equality sign is replaced by proportionality because the field at the detector is the strength of the scattering element at $\vec{r}$. The second term in Eq. 1.3 shows that the phase at the detector is a function of the position of the scattering element, and the vector $\vec{q} = \vec{k_i} - \vec{k_s}$ called the scattering wave vector. The direction of the scattering wave vector is in the scattering plane from $\vec{k_s}$ to $\vec{k_i}$, as shown in Fig. 1.2(c). If the scattering is elastic, i.e.,$|\vec{k_s}| = |\vec{k_i}|$, the magnitude of q is given by

$$q = 2ksin(\theta/2) \tag{1.4}$$

where $k = 2\pi/\lambda$ with λ is the wavelength and θ is the scattering angle

$$q = (4\pi/\lambda)sin(\theta/2) \tag{1.5}$$

Equation 1.5 defines the scattering wave vector, which has the dimension of inverse length q^{-1}. That represents the length scale, or the probe length, of the scattering experiment. From Eq. 1.3, the amplitude of the scattered wave is

$$E_{sca}(\vec{q}, \vec{r}) \sim E_0 e^{i\vec{q}.\vec{r}} \tag{1.6}$$

Equation 1.6 indicates that when the variation of r is small compared to q^{-1}, the magnitude of the scattered field will not significantly change; whereas if r varies significantly compared to q^{-1}, the scattered field will significantly change. That means q^{-1} represents a length scale to be compared to the length scales of the scatterer. As such, the scattering experiment cannot resolve anything less than q^{-1}. Therefore, this comparison determined the scattered field.

1.1.2 The Structure Factor

The structure factor is the square of the Fourier transform of the real space structure of the object that is scattering the wave radiation. In other words, it is the far-field, Fraunhofer diffraction of the scattering object. The structure factor describes mathematically how material scatterers incident radiation. The total scattered field for a system of N scatterers in an object is given by Eq. 1.6 such that

$$E_{sca}(\vec{q},\vec{r}) \sim \sum_{i}^{N} e^{i\vec{q}.\vec{r_i}} \tag{1.7}$$

Then the scattered intensity I= EE* is

$$I_{sca}(\vec{q}) \sim \sum_{i}^{N}\sum_{j}^{N} e^{i\vec{q}.(\vec{r_i}-\vec{r_j})} \tag{1.8}$$

Now the structure factor is defined as

$$S(\vec{q}) = \frac{1}{N^2}\sum_{i}^{N}\sum_{j}^{N} e^{i\vec{q}.(\vec{r_i}-\vec{r_j})} = \frac{1}{N^2}|\sum_{i}^{N} e^{i\vec{q}.\vec{r_i}}|^2 \tag{1.9}$$

The structure factor is dimensionless such that S (0) = 1. On comparing Eq. 1.8 and 1.9,

$$I_{sca}(\vec{q}) \sim N^2 S(\vec{q}) \tag{1.10}$$

Thus, the scattered intensity has proportionality with the structure factor. That determines the relationship between the scattered intensity, I(q), and structure factor, S(q). Any scattering object can be assumed to be made up of many small sub-volumes that act as point-like scatterers at various positions $\vec{r}$. Thus, the total scattered intensity at the detector is the sum of all the waves from these point-like scatterers that make up the object, which is given by Eq. 1.7. On converting the sum to an integral,

$$\sum e^{i\vec{q},\vec{r_i}} = \int e^{i\vec{q},\vec{r_i}} n(\vec{r}) dr \tag{1.11}$$

where, $n(\vec{r}) = \sum \delta(\vec{r} - \vec{r_i})$ is the Dirac delta function

$$E_{sca}(\vec{q}, \vec{r}) \sim E_0 \int e^{i\vec{q}.\vec{r}}.n(\vec{r}) d\vec{r} \tag{1.12}$$

This indicates the experimental situation where scattering will take place from an ensemble of particles of random orientations, eliminating the vector nature of the scattering wave vector, q.

Now, Eq. 1.9 and 1.11 lead to

$$S(\vec{q}) = \frac{1}{N^2} |\int e^{i\vec{q}.\vec{r}}.n(\vec{r}) d\vec{r}|^2 \tag{1.13}$$

Equation 1.13 shows that the structure factor is the normalized Fourier transform squared of the density distribution of the particle. Here, the position vector $\vec{r}$ is relative to the center of mass of the system of scatterers. Figure 1.3 shows an example of a diffraction pattern (structure factor) for 1, 2, and 3−dimensional objects. Each structure factor has a constant forward scattering lobe, followed by the Guinier regime and then the Porod, or power law, regime. The Porod's law says that the slope of the power law will go as -$(2D_m - D_s)$, where D_m is the mass scaling dimension and D_s is the surface scaling dimension [20]. For a thin wire, $D_m = 1$ and $D_s = 0$, giving a slope of -2, while for a thin disk, $D_m = 2$ and $D_s = 1$, leading to a slope of -3. Similarly, for a sphere, $D_m = 3$ and $D_s = 2$, giving a slope of -4.

The slopes are marked in Fig. 1.3(b). Figure 1.3(b) shows a distinct spike in the structure factor at large qR_{eq} for the thin wire and disk whereas Fig. 1.3(a) shows the structure factor is symmetric about $\theta = 90°$ for the thin wire and disk, leading to the spike. This feature is not readily available from Fig. 1.3(b), which shows both analysis methods and views are required to get the complete information.

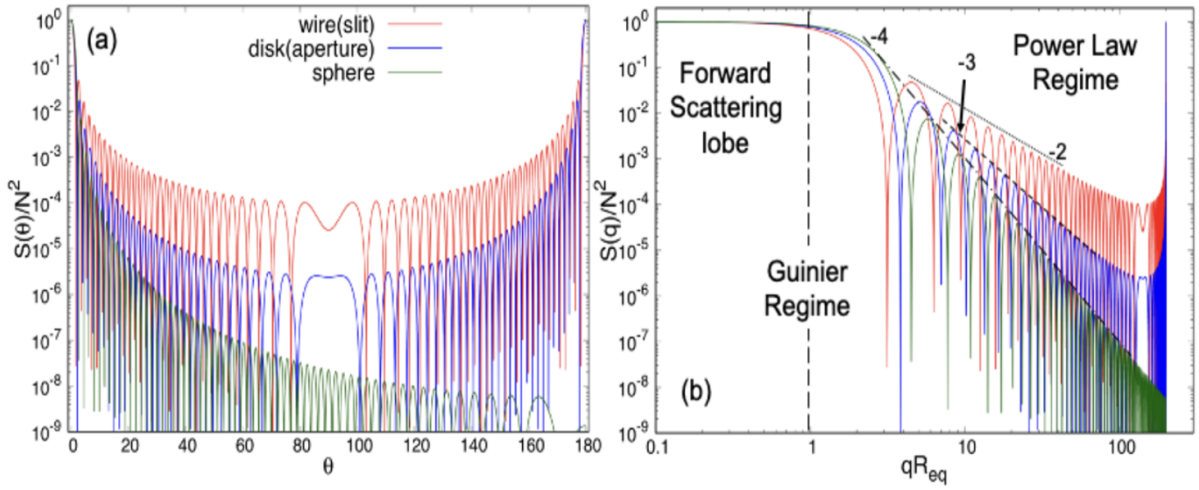

Figure 1.3: *The structure factor (i.e., the diffraction pattern) of a wire (1−d), disk (2−d), and sphere (3−d) are plotted (a) versus scattering angle, θ on a linear scale and (b) versus the dimensionless quantity, qR_{eq} on a double log scale, called Q-space. The Q-space plot uncovers the different regimes, indicating Q-space analysis's benefit over conventional θ-space plotting [17].*

1.1.3 The Q-space Applied to Sphere

Properties universal to scattering by all particles become more apparent by plotting the scattered intensity versus the dimensionless variable, qR, where R is the effective radius of the particles. Improvement can also be made by normalizing the differential scattering cross section by the Rayleigh differential cross section of the particle. Note that the differential scattering cross section is proportional to the scattered intensity and the phase function

[4–6]. Thus,

$$dC_{sca,Ray,Sph}/d\omega = k^4 R^6 F(m) \tag{1.14}$$

where $k = 2\pi/\lambda$, and F(m) $= |(m^2-1)/(m^2+2)|^2$. The function F(m) is the square of the Lorentz-Lorenz function of the particle's refractive index $m = n + i\kappa$. It has been shown that the scattering by spheres is well parameterized by the internal coupling parameter and is given by [21]

$$\rho' = 2kR|(m^2-1)/(m^2+2)|^2 \tag{1.15}$$

This parameter is similar to the well-known phase shift parameter, $\rho = 2\text{kR}|m-1|$, which was used in previous works [13–15]. The phase shift parameter describes the phase difference between a beam of light traveling through the sphere's diameter and another beam that travels the same distance outside the sphere. In contrast, the internal coupling parameter, ρ' is related to the Lorentz-Lorenz factor, which is directly involved in the radiative coupling between the subvolumes that comprise the particle. When the coupling is strong, the field within the particle is no longer equal to the incident field. Then, the scattering is no longer in the purely diffraction regime and this is called the Rayleigh Debye-Gans (RDG) limit. The internal coupling parameter does a better job in explaining the light scattering pattern away from the diffraction limit, where $\rho' = \rho = 0$. The ρ' provides a quasi-universal description of the evolution of scattering by unifying the size parameter kR and the refractive index m, which is shown in Fig. 1.5. For the same ρ', the scattering pattern will be very similar. Note that the Lorentz-Lorenz term involved in ρ' reduces to $|m-1|$, the functionality of ρ in the m$\rightarrow$1 limit.

Figure 1.1, above, shows forward normalized scattered intensity for spheres with different sizes, plotting the same data versus scattering angle, θ linearly (Fig. 1.1(a)) and the dimensionless quantity qR, on a log-log scale, i.e., Q-space (Fig. 1.1(b)). Based on the Q-space plot, the total angular scattering can be studied by dividing it into three regimes, namely: a) forward scattering lobe including Guinier regime, (b) side scattering, and (c)

backscattering.

1.1.4 Forward Scattering Lobe Including Guinier Regime

The forward scattering regime is known for a flat, constant intensity regime independent of scattering angle, θ and hence is q independent. The forward scattering lobe lies in the region qR $<$ 1 that ends near qR $\simeq$ 1 ($\theta \approx \lambda/2\pi$R), where R is the effective radius of the particle. In Fig. 1.1, the data were normalized to illustrate the effect of the scattering angle. Theoretical calculations show that larger particles have more intense scattering with a narrow angular range in the forward scattering regime than smaller particles. This regime is diffraction-dominated, hence, only weakly dependent on particle refractive index and shape. Figure 1.4 plots the forward scattering intensity as the differential cross section for spherical particles at $\theta = 0$ versus the sphere radius R for various values of real parts of the refractive indices, n. The figure shows two major regimes with a crossover near $R \simeq \lambda$. In one regime, scattering goes to the sixth power of radius R with n dependence when R $\simeq \lambda$, called the Rayleigh regime. In the other regime, scattering goes to the fourth power of radius R and becomes independent of n when $R \geq \lambda$, i.e., 2d diffraction limit, called a Geometric regime. That shows that the differential scattering cross-section has two functionalities on R, hence on λ as shown from dimensional analysis.

The Guinier regime lies in the region qR $\simeq$ 1. The Guinier equation was derived for X-ray scattering, which has a refractive index of essentially one. This means that X-ray scattering is simply wave diffraction. Guinier's analysis of scattering data allows for determining the radius of gyration, R_g, of any arbitrarily shaped particles. It is applicable for q$R_g \leq 1$ [22]. The Guinier formula is based on a second-order expansion of the structure factor of the particle. For example, the structure factor for a sphere is given by $S(q) = (1 - (qR_g)^2/3)$. Here, R_g is the radius of gyration of the scattering object. For a uniform sphere, $\mathrm{R}_g{}^2 = (3/5)R^2$. Here R represents the radius of the sphere. If we compare light scattering determined Mueller matrix elements like phase function F_{11} to theory, we need

the light scattering inferred size distribution of the scatterer rather than the microscopic size distribution.

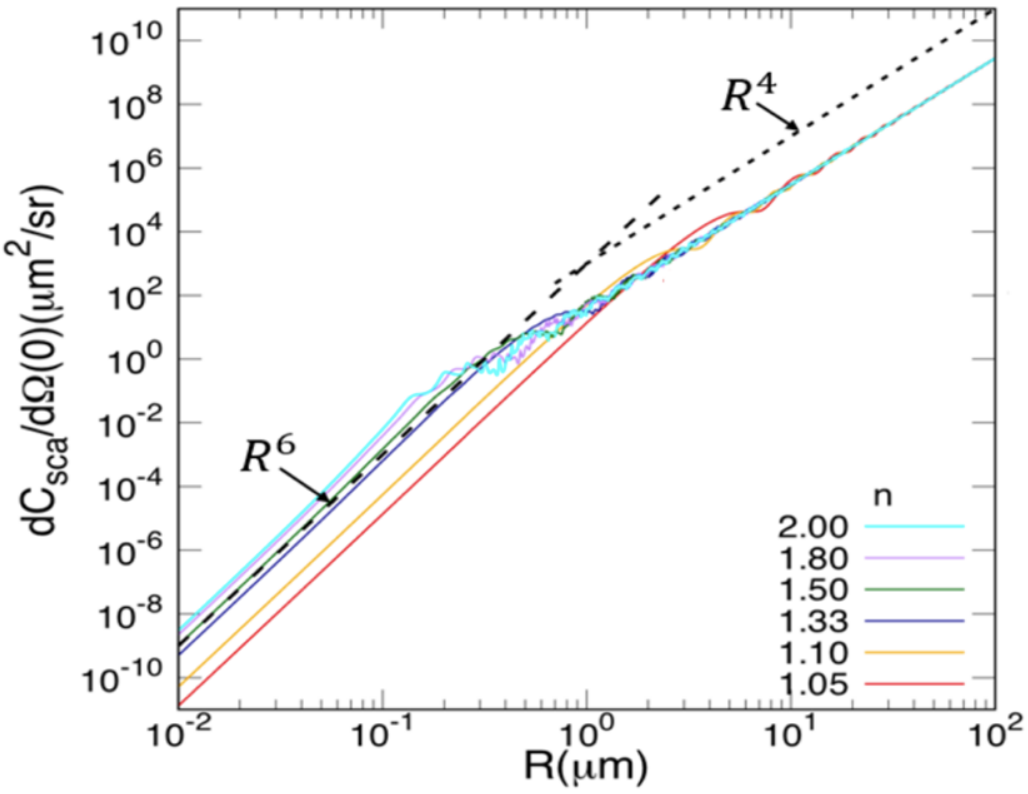

Figure 1.4: *The differential scattering cross-section at $\theta = 0$ for spherical particles versus radius for a systematic variety of real parts of the refractive indices n. The wavelength of light used is $\lambda = 532nm$ [14].*

1.1.5 Side Scattering Regime

The side scattering regime can be interpreted as a crossover from diffraction to refraction dominated. This regime is complex beyond the Guinier regime when $1 \leq qR < 2kR$, which evolves with increasing ρ'. This regime is also called a power law regime. Figure 1.5(a) shows, Q-space schematic diagram of the unnormalized scattering envelopes for an arbitrary sphere, ignoring the ripples, plotted versus q (not qR). Figure 1.5(b) demonstrates the quasi-

universality of Rayleigh-normalized Mie scattering on the internal coupling parameter. For $\rho' < 1$ and $qR > 1$, the RDG limit holds $(qR)^{-4}$ power law. As ρ' increases above unity, the forward scattering falls relative to the Rayleigh limit with three semi-power laws. For $3 < \rho' < 30$, three power-law regimes evolve with the exponents of 0, -2, and -4. Likewise, when $\rho' \geq 100$, a fourth power law is quite apparent with a -3 exponent. Figure 1.5(b) shows that the -2 power law extends from the Guinier regime (hump) to another hump centered near $qR \approx \rho'$. The power law envelope of -3 (for large ρ') can be explained by 2d diffraction from the projection of particle shape, i.e., spherical particle acting as a two-dimensional, circular aperture. At large $qR \geq \rho'$, there is a tendency to reach the 3d spherical diffraction limit of $9(qR)^{-4}$ functionality regardless of ρ' [21]. Figure 1.5 (b) shows that for a given ρ', even though the refractive indices and size parameters vary widely, all the plots fall together except for within the backscattering regime. This demonstrates the quasi-universal parameterization provided by ρ'. Note that size parameters were determined from known values of internal coupling parameter ρ' and the refractive index, m. The power law regime is quite diverse among the different shapes. This diversity broadens when one includes spheres and fractal aggregates, and it deepens with increasing ρ' [17, 19].

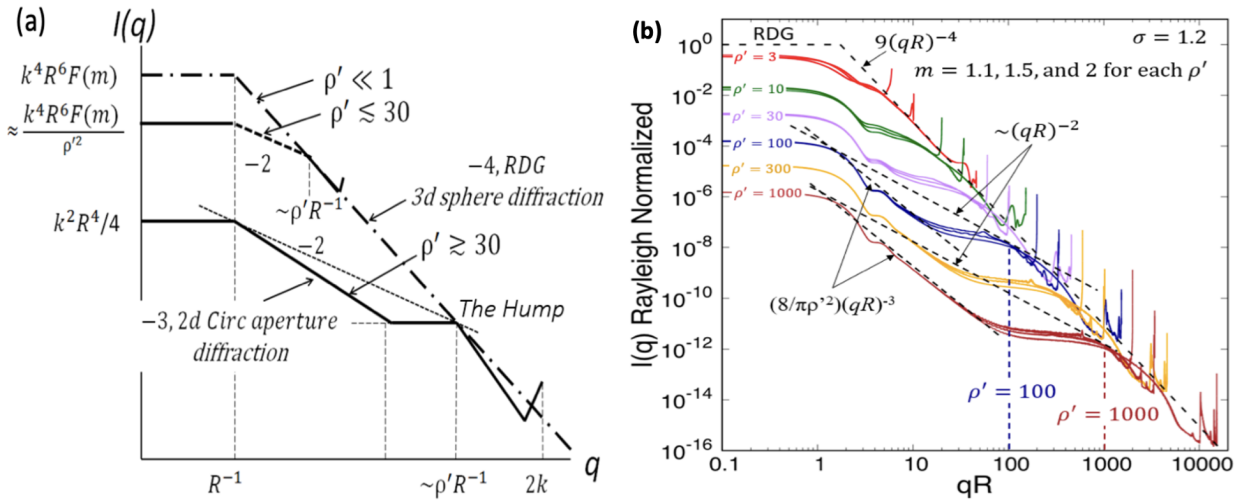

Figure 1.5: *(a) Q-space schematic diagram of the unnormalized scattering envelopes for an arbitrary sphere with a real refractive index plotted versus q. Three stages of scattering are shown as its functionality evolves from the 3d diffraction limit (RDG) when $\rho' << 1$, with increasing ρ'. (b) Q-space demonstration of the quasi-universality of Rayleigh-normalized Mie scattering on the internal coupling parameter ($\rho' \to 0$, dashed line, for the RDG limit and $\rho' = 3$, 10, 30, 100, 300, 1000) is plotted versus qR for three refractive indices, $m =$ 1.1, 1.5, and 2. The sphere radii range from 0.25 to 647 microns. The vertical dashed lines at $\rho' = 100$ and 1000 indicate the position of the hump. Black colored dashed lines indicate the RDG limit, -2 and -3 power laws [23].*

1.1.6 Backscattering Regime

This regime begins when the scattering begins to increase relative to the side scattering. This regime is a mix of both refraction and wave interference. This is also called an "enhanced" backscattering regime, where the generalized rainbows and the glory appears, near $qR = 2kR$ (which corresponds to $\theta = 180°$). Scattering at backscattering regime is very sensitive to the size and refractive index. The sensitivity of backscattering on particle's size and refractive is demonstrated in Fig. 1.6, which shows an order of magnitude variation

in the intensity ratio I(180°)/I(178°) for small change in radius and refractive index. The backscattering data is useful for lidar and remote sensing measurements.

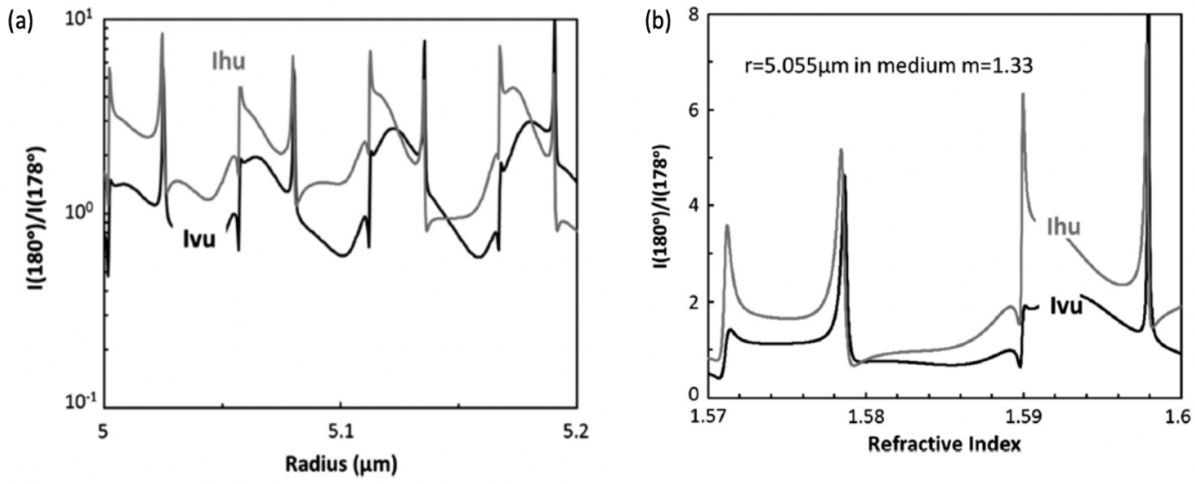

Figure 1.6: *I(180°)/I(178°) versus (a) radius over the range of 5.0 to 5.2 μm with a refractive index of m = 1.59 immersed in water with m = 1.33. (b) refractive index over the range of 1.57 to 1.6 for a radius of r = 5.055 μm in a medium with a 1.33 refractive index (water). Here, I_{hu} and I_{vu} represent horizontal polarization and vertical polarization, respectively [24].*

Chapter 2

A Wide Range $(0.32^\circ \leq \theta \leq 177.6^\circ)$ Multi-Angle Light Scattering Setup and Concomitant Analysis Method

The content of this chapter is based on Gautam and Sorensen [25].

2.1 Introduction

The setup described here can measure light scattering from extremely forward to a backscattering angle near 180°. Light scattering data from extreme forward and backward directions is important to gain a complete understanding of scattering by aerosol particles. Guinier's analysis of small-angle light scattering data yields the particle size of the scatterer to a good approximation. To estimate the size of large particles, we need the extremely small angle light scattering data that our setup provides. By analyzing the light scattering data from the back direction, which is complex and very sensitive to the size, shape, and refractive index of the scatterer, one can lay a foundation for the interpretation of remote sensing and identification of aerosols.

Many experiments have been done, but we know of none that have covered the whole angular range as well as the setup described here. The Amsterdam- Granada group, in their monumental work, studied the light scattering of a variety of aerosol particles with an apparatus that allowed measurements from scattering angles of $\theta = 3°$–$177°$ [26–31], 5°–174° [32] and 5°-173° [33, 34]. For their measurements, they had to move the detector along a ring surrounding the scattering sample from one scattering angle to another. Hunt and Huffman developed polarization-modulated light scattering instruments that can record the data from 5° to 168° in a relatively short time [35]. Bell and Bickel used an experimental setup that can measure over the angular range of 5°-160° [36]. From our perspective, it is important to recognize that 5° is more than an order of magnitude larger than 0.32° and important scattering phenomena, such as the glory, occur at angles greater than 168°. Curtis et al. (2008) have studied light scattering with a setup that can measure from 17°–172° [37]. Brendon et al. (2014) built an apparatus that could measure the light scattering through an angle from 155°– $\sim$ 180° [38], and Miffre et al. (2019) built an apparatus that could measure from 176°–$\sim$ 180° [39]. Most importantly, each experiment was missing the extreme forward scattering angles from which one could determine the size of the scatterer via a Guinier type of analysis. Moreover, forward scattering is important given the fact that approximately 50% of the scattered light occurs within the Guinier regime in the forward scattering lobe such that $\theta \leq \lambda/\pi$D, where λ is the wavelength of light and D is the particle diameter [40]. For many years we have applied small angle scattering methods to aerosols [19, 41–46]. The apparatus to be described here has advantages over these others because it is built to measure light scattering at many angles from very small, 0.32°, to nearly 180°, 177.60° simultaneously. This small angle (0.32°) for the forward scattering is a factor of 10 smaller than the Amsterdam Granada group. From our previous studies [45, 46], it is observed that if one is to perform scattering experiments to study backscattering, one must use forward light scattering data to determine the size, and if the particles are in the micron size range, one needs very small angles. With this setup, one can measure the scattering from aerosols with

sizes from nanometer range (if the aerosol is dense enough) to 15−20 micron with enough data points for Guinier analysis. However, this setup can be used to measure scattering from millimeter size particles having limited or no data points for Guinier analysis. Nevertheless, we could obtain data for side scattering and very useful, backscattering data. Thus, the setup we present here, is a great tool in the light scattering world that can measure light scattering throughout the complete angular range with notable resolution towards extreme forward scattering.

2.2 Experimental Design

The setup described here provides the data for such a small angle range to a very large scattering angle (i.e., 0.32° to 177.6°), and corresponding scattering wave vectors ranging from 660 cm^{-1} to 2.36 $\times$ 10^5 cm^{-1}. Those angles were determined by geometrical calculations where the calculated angles are the mid-point angles of the detector channels. Due to the non-zero width of the channels, detecting angles have an angle spread and corresponding scattering wave vector spread. Each channel integrates the light scattered along its width.

Figure 2.1 gives a schematic of the apparatus and Fig. 2.2 (a) a real picture of the apparatus and (b) scattering volume. The light source for our setup is a vertically polarized green laser (Coherent 532 nm CW DPSS Sapphire) with wavelength λ = 532 nm and a beam size at 1/e2 of 0.7 mm. Scattering matrices can be measured by manipulating linear polarizers and quarter-wave plates just after the laser source on its way to the scattering volume and in front of the detectors. Initially, we had planned to use a polarizer and an electro-optic modulator to send sinusoidally modulated polarized incident light into the scattering system, but the setup proved unreliable. However, based on the information of the scattering matrix and Stokes vectors, it was straightforward to send different polarized incident light by manipulating the different polarizer and wave plates. With this, we could

obtain all of the six matrix elements.

The scattering volume is the region at which laser light interacts with the aerosol coming from the aerosol tube with inner diameter 3 mm. Thus, the scattering volume is cylindrical, with dimensions 3 mm $\times$ 0.7 mm. The scattering for this setup can be divided into three different sections, namely forward, side and backscattering.

2.2.1 Forward Scattering

The forward scattering design is based on a design by Ferri (1997) [47]. This design includes a Fourier lens, beam stop and imaging lens. The Fourier lens L1 (Achromatic Doublet, F = 100 mm, Thorlabs AC508-100-A) is placed at a focal length's distance from the center of the scattering volume. Light scattered from the scattering volume and rays scattered parallel to one another are brought to converge at the back focal plane of the Fourier lens. All rays scattered at the same angle, θ are mapped by the Fourier lens L1, in a ring of radius r from the optical axis. Each ring of scattered light comes at the same r hence the same angle θ, and hence the same q, as given in Eq. 1.4.

An imaging lens L2 (Achromatic Doublet, F = 35 mm, Thorlabs AC254-035-A) is used to match the Fourier plane of the lens L1 and the 16-channel photodiode array (Hamamatsu S8558) detector. For such a small forward scattering angle measurement, there is a challenge to block the un-scattered light coming directly from the laser source that might fall onto the detector. For this, a beam stop is placed at the focal point of the Fourier lens. The beam stop is a 1.5 mm diameter steel rod with a 45° cut surface such that it will act as a mirror and reflect the un-scattered light coming directly from the laser to a beam dump, preventing the un-scattered light from reaching the detector. The forward scattering setup collects the scattered light through an angle ranging from 0.32° to 9.89°. The angular width of the channel is 0.55° approximately.

2.2.2 Side Scattering

For the side scattering, a custom elliptical mirror (Optiforms 2753-0100-1300-0-00 ELLIPSE, AQ COATED) is used to collect the scattered light. The scattering volume lies on the near focal point of the ellipse and a 1 mm iris (Thorlabs SM1D12C) is at the farther focal point. This iris would be able to block the stray light falling on to the detector. The scattered light passing through the iris then passes through a collimating lens (Thorlabs AC127-030-A) to send parallel light the detector. The detector used for this scattering measurement is a 16-channel photodiode array (Hamamatsu C12677-03), different than the one used for forward scattering measurement. The difference is that it is more sensitive than the forward detector, which is needed because in most situations the side scattering is much less intense than the forward scattering. One channel of this detector was sacrificed as a monitor. This side scattering arrangement collects the scattered light through a wide range of angles from 15° to 157°. The angular width of the channels is 9° approximately.

2.2.3 Backscattering

To collect the backscattered light, we use a 90° off axis parabolic mirror (Thorlabs MPD229H-PO1, RFL = 50.8 mm) with a 3 mm hole parallel to the incident beam. This mirror is placed in between the laser source and scattering volume so that the distance between the center of the scattering volume and the near edge of the mirror hole would be 50.8 mm. The laser from the source passes through the mirror hole and incident on the aerosol, coming up through the aerosol tube, forming a scattering volume. The parabolic mirror then collects the scattered radiation that falls on either side of its hole and reflects and collimates it at 90°, with respect to the incident laser direction. Light that fell on the right side of the hole is blocked, allowing only that which fell on the left side of the hole (looking anti-parallel to the beam source). The collimation of the reflected rays from the parabolic mirror was tested. The reflected rays formed a circle on a white sheet of paper and by moving it from the parabolic mirror to the detector with constant diameter ensured

that the rays were collimated. The width of the collimated light after reflection from the parabolic mirror was found to be 24 mm, whereas the detector width was 12 mm. Therefore, the width of the beam had to be reduced. A Keplerian Telescope, where the focal lengths of both lenses are positive, was built to act as a beam reducer. For this, two Plano-convex lenses with focal length 60 mm and 30 mm were used and aligned in a Keplerian form. The beam width was reduced by a factor of 2, which is the ratio of focal lengths. Thus, the beam width will match the length of the detector. A pinhole with a diameter of 1 mm was placed at the coinciding focal points to block stray light. The same detector was used for both side and backscattering measurements. Two mirrors were used to control which scattering went to the detector. The reduced beam after lens L5 hit mirror M1 at a 45° angle and was reflected. This reflected light then fell on another mirror M2 (The "flipping mirror") at a 45° angle and was again reflected to the detector. The flipping mirror blocked side scattering when it was used to measure backscattering. The midpoints of the detector channels angle ranged from 158° to 177.6°.

We performed the tests for background signals that might distort the measurements at the side and backscattering regions. We did this in three different ways:

1. Firstly, we measured the background signal detected by the detector with the laser off.

2. Secondly, we measured the background signal with the laser on but no particles in the scattering volume.

3. Thirdly, we measured the background signal with the laser on and aerosol particles in the scattering volume but blocked the path through which scattered light travelled into the detector at the pinhole.

All three background measurements agreed within the random error and were much smaller than typical scattering measurements.

Scattering in the back direction is weak, and its detection above background scattering is notoriously difficult. One advantages we have over colloidal systems is that our aerosols

are not in a container hence there is no scattering from the container walls which can foil a measurement (this is problematic in the forward direction too). The reader will note that we did not use a beam splitter in the back directions, and we did so because beam splitters create significant stray scattered light. The off-axis parabolic mirror avoids this. Nevertheless, one could use a beam splitter to get to 180° if the particle scattering is strong enough.

In summary, the entire apparatus collected scattered light through an angle range of 0.32° to 177.6°. The different channels have different angular spread ranging i.e., 0.55° (forward scattering), 9° (side scattering) and 1.2° (backscattering).

The two detectors collect scattered light from 31 angles simultaneously (46 angles overall), which allows for quick and efficient procurement of data. A quick sampling time will eliminate the effects of possible in-homogenies of the aerosol that can cause spurious fluctuations in the scattering when the scattering is detected one angle at a time. These two detectors were connected to a data acquisition box which was connected to a computer. Obviously, a third detector could be added, and the flipping mirror mechanism eliminated so that all 46 angles could be detected at once. However, funding limitations prevented us from doing so.

Additionally, this experimental design includes an aerodynamic particle sizer (APS) (aerosol sampling device) as a part of it, to sample the aerosol coming vertically up through the aerosol tube. This sampling device provides a real time measurement of the most probable size of the aerosols and their size distributions spread. That allows us to compare the Mie results calculated for these in situ observed parameters with the experimentally measured scattering results.

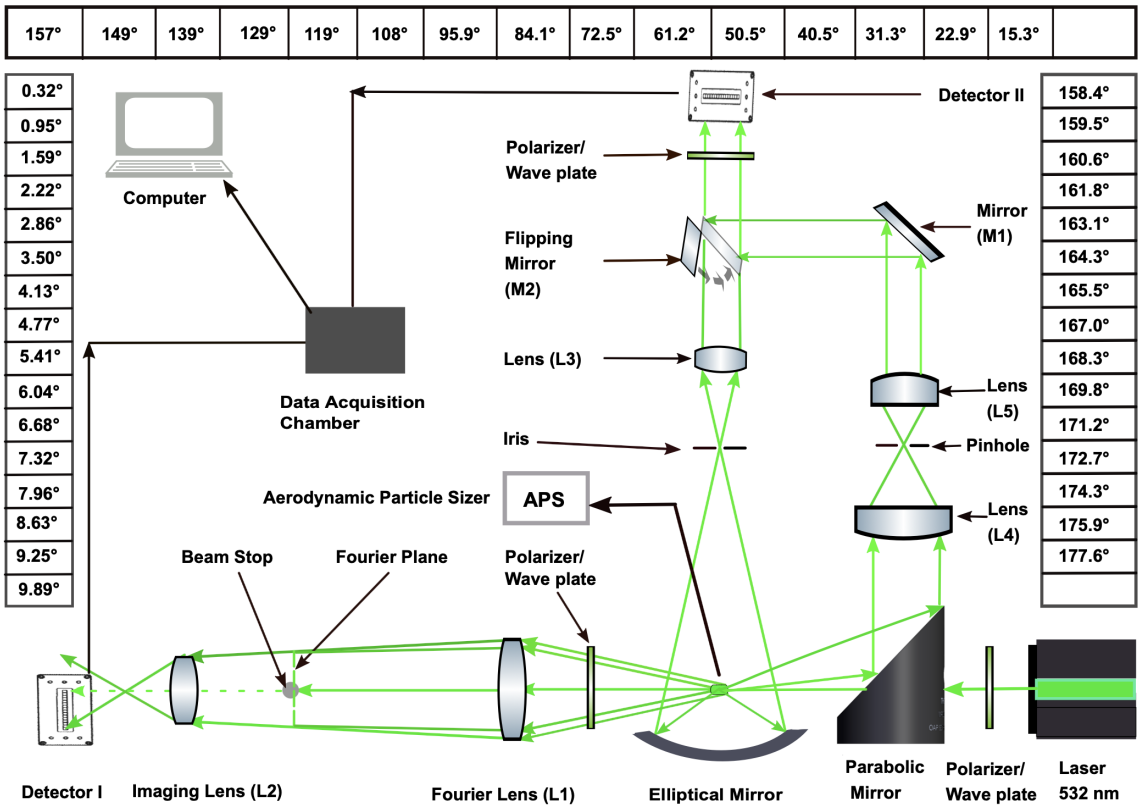

Figure 2.1: *Schematic diagram of the multi-angle light scattering apparatus. The Aerodynamic Particle Sizer (APS) samples the aerosol after it passes through the scattering volume.*

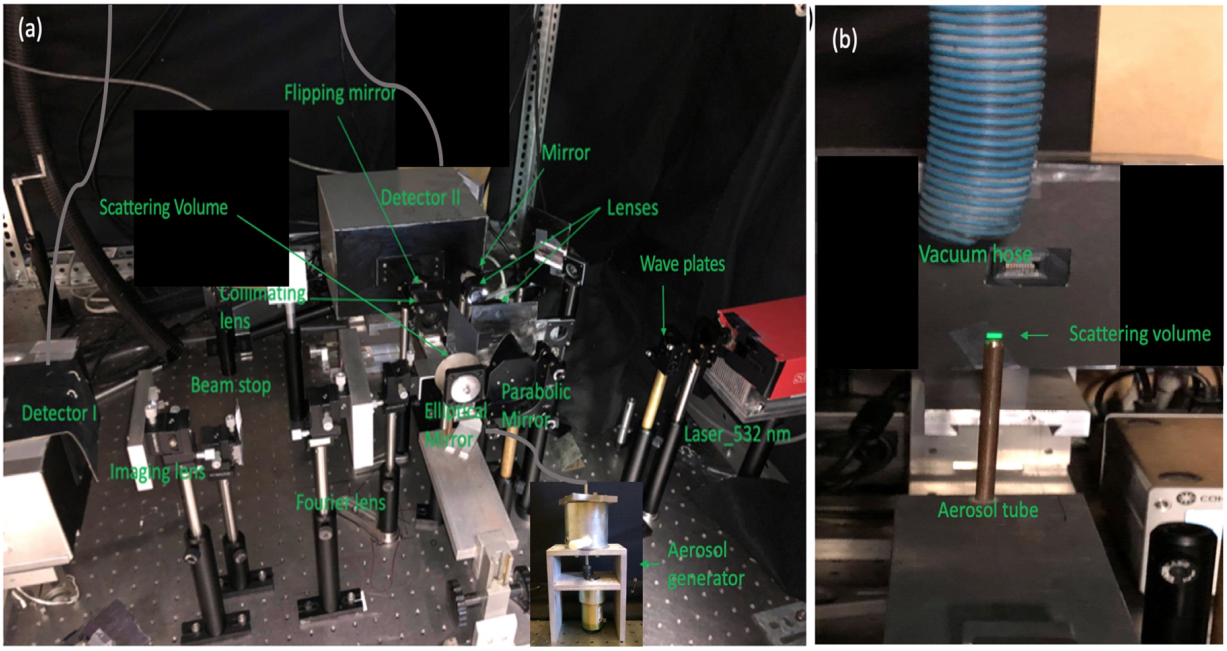

Figure 2.2: *(a) A real picture of the multi-angle light scattering apparatus, (b) Scattering volume.*

2.2.4 Aerosol Generator

Throughout the whole study, we have scattered the light from dust particles as well as water droplets. For the water droplets generator, we used a 6-jet Collison Nebulizer from CH Technologies; whereas, we used a lab made dust generator to aerosolize the dust particles. Figure 2.3(a) shows the schematic diagram with major parts labeled and Fig. 2.3(b) is the real picture of the dust generator [19, 48]. The dust generator had a dimension of 7.5 cm in diameter and 7.5 cm in height. The dust particles were loaded in the chamber. The bottom of the chamber had a stir bar connected to a motor, which in turn connected with the power supply to spin the stir bar at 200 revolutions per minute. To aerosolize the particles, oxygen blew in from the bottom of the chamber. The aerosolized particles were then taken to the scattering volume by vinyl tubing, connected to the vertically positioned aerosol tube with internal diameter of 3 mm.

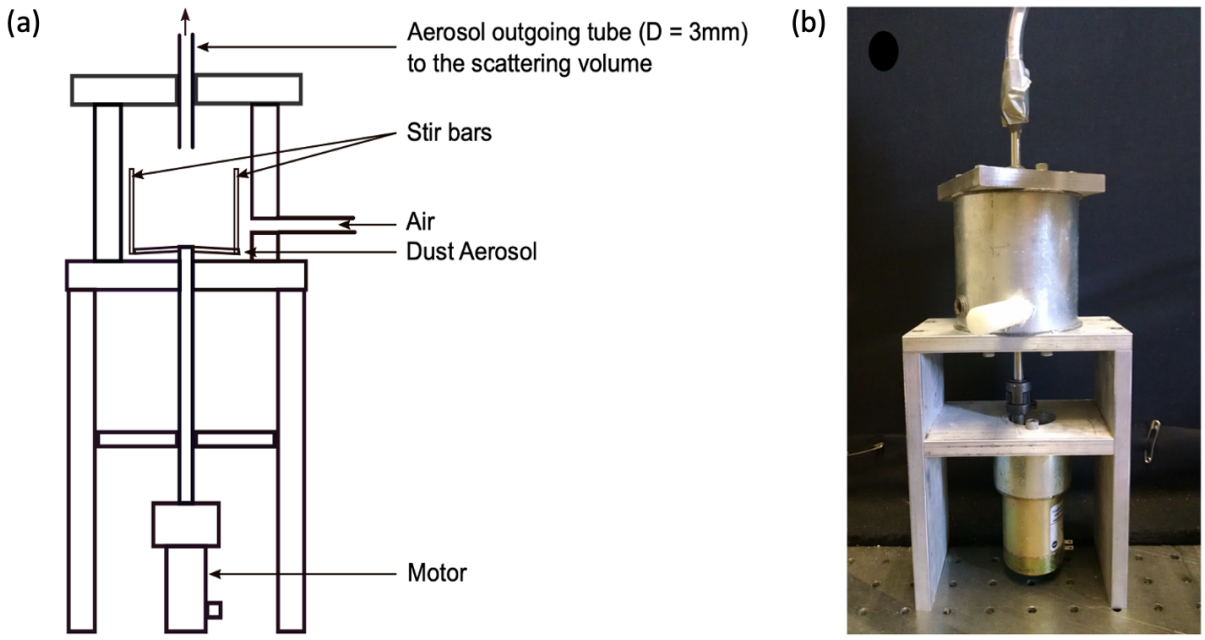

Figure 2.3: *(a) Schematic diagram with major parts labeled, (b)real picture of the dust generator.*

2.3 Setup Calibration

2.3.1 Forward Scattering Calibration

The forward scattering design was calibrated by diffracting light through a 10-micron single slit into the forward direction. The measured diffracted intensity was then compared to the well-known theoretical results [49]. Figure 2.4 shows a comparison of the data to the theory in both the usual "θ-space" and our Q-space. The comparison from each perspective is good, implying that our forward scattering setup works well.

Figure 2.4 also allows us to compare the θ-space and Q-space perspectives. Q-space analysis applied to the single slit uncovers a power law envelope with an exponent of -2 that is not apparent in θ-space, which involves plotting intensity versus scattering angle on linear scales. In general, the power law envelope follows the rule $q^{-(2Dm-Ds)}$, where D_m is

the mass scaling dimension and D_s is the surface scaling dimension of the scatterer [50]. For a single slit $D_m = 1$ and $D_s = 0$. Q-space analysis also shows a q independent, hence θ independent, forward scattering lobe. Furthermore, Q-space analysis also shows a Guinier regime as the forward scattering lobe ends and the power law envelop begins. None of these features are apparent in linear θ-space.

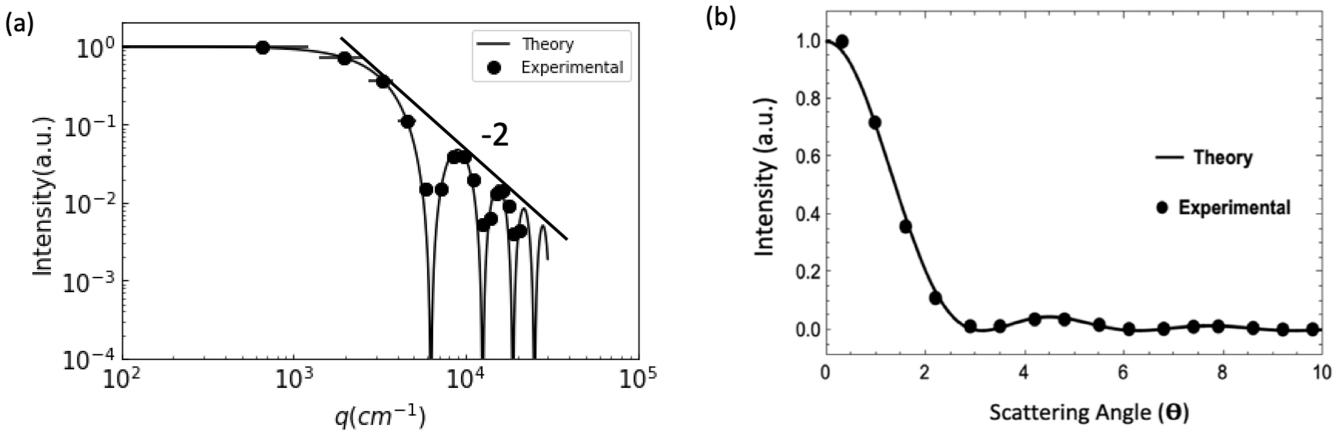

Figure 2.4: *(a) A comparison of experimentally measured diffracted intensity for 10 microns wide, single slit diffraction with a theoretically calculated diffraction pattern. (a) Q-space analysis of the measured intensity was plotted versus scattering wave vector $q(cm^{-1})$ on a double logarithmic graph. Note, the power-law envelope with a slope of -2, which indicates the match between theory and experiment and accuracy over one- and one-half orders magnitude of intensity. Also, note a q independent forward scattering lobe and a cross over the Guinier regime. (b) Same data and theory plotted versus scattering angle θ-space analysis on a double linear graph.*

2.3.2 Side Scattering Calibration

To calibrate side scattering, we used a capillary tube with a diameter of 1.5 mm and a length of 5 cm to simulate the real scattering volume. We filled the capillary tube with

a glowing agent and covered it with a black tape, except for a 3 mm length at the end. We aligned it horizontally at F1 of the elliptical mirror, ensuring that the glowing part of the capillary would occupy the position of the real scattering volume (Fig. 2.5(a)). This simulated a scattering volume uniformly scattering. With alignment (Fig. 2.5 a(ii)), we were able to simulate uniform scattering with angles greater than 90°. We then reversed the position of the glowing and covered parts of the capillary tube and then measured the intensity with angles less than 90° (Fig. 2.5 a(iii)). After that, we combined the separately measured intensities and plotted intensities versus the scattering angles shown in Fig. 2.5(b). The figure showed that measured intensity is uniformly distributed throughout the angles, as expected from the glowing agent with root mean square deviations (RMSD) 0.032. This indicates that the side scattering setup is aligned and that there is no need for any correction for any channels.

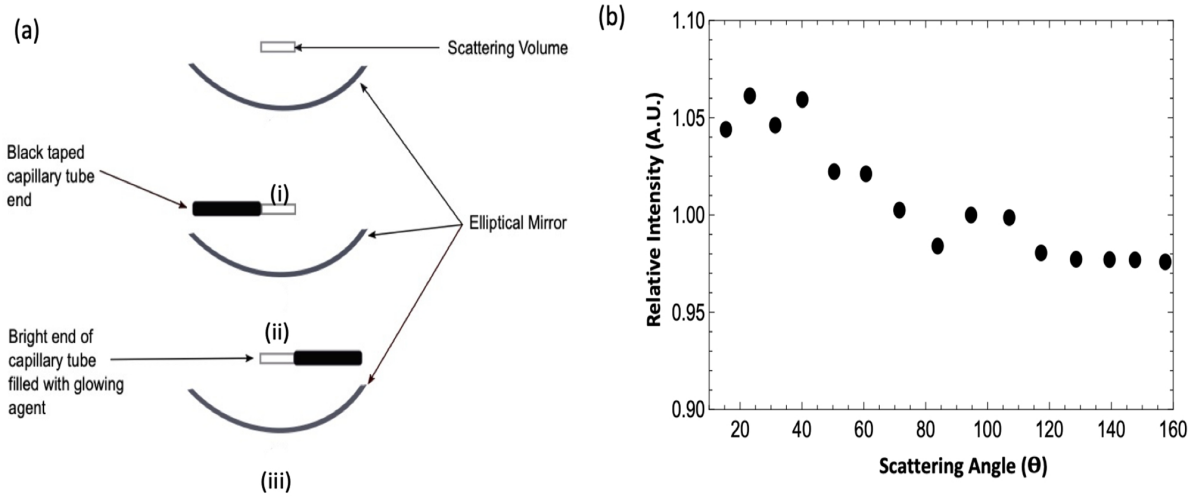

Figure 2.5: *(a) (i) A top view of real scattering volume. (ii) and (iii) Capillary tube filled with glowing agents at one end (3 mm) and covered with black tape at the other end to measure the intensity at angles greater and less than 90°, respectively. (b) Combined intensities measured by capillary calibration method versus scattering angle, θ. Note that, the data is plotted on a linear scale and the variations are well below 10%.*

2.3.3 Backscattering Calibration

The backscattering setup was calibrated by comparing to a random scatter screen/intensity and single slit diffraction in the back direction. For this, a glass diffuser (DG10-220-P01) from Thorlabs with a known backscattering angular pattern and a 10-micron wide, precision optical slit was used. Both the glass diffuser and the single slit were placed at the focal point of the 90° off axis parabolic mirror (with holes parallel to focused beam), which coincided with the center of the scattering volume. The glass diffuser was a protected silver reflective, and the slit was a photo-etched on a chromium-coated glass substrate which diffracted the light both into the forward direction and back direction. The laser beam from the source passed through the parabolic mirror hole, hit the diffuser and was diffusely reflected. Simi-

larly, the laser was diffracted both in the forward and back direction once it hit the slit. Both diffusely reflected and back diffracted light from the slit then followed the same path to the backscattering detector as light from an aerosol sample, and the intensities were measured.

Figure 2.6 shows the method of the backscattering setup calibration. Fig. 2.6(a) compares the reflected measured intensity from the diffuse reflector to the Thorlabs measured data[www.thorlabs.com]. The two sets of data are normalized to each other at 177.6°. Our measured data started to show a disagreement with the Thorlabs data after 165.5° and this disagreement reaches as much as 25%. Figure 2.6(b) shows the comparison of measured diffracted intensity with the well-known, single slit, theoretical results [49]. With light being back diffracted, the relevant scattering angle is the phase angle, $\alpha = 180°$- θ, and the analogous scattering wave vector magnitude is $q' = (4\pi/\lambda)sin(\alpha/2)$. This "backward" Q-space analysis of the back diffracted light from the slit is shown in Fig. 2.6(b). There we see a good fit between the data and the theory except for theoretical minima on the large-scale log graph. The minima are not fit because the detector channels have finite width and thereby spatially integrate over the rather sharp minima. Figure 2.6(c) shows the magnitude of the product I (measured intensity) $\times$ $q^{'2}$ versus q' on a magnified scale. A discrepancy is seen. Finally, we showed that the discrepancy is removed when the data is corrected by a factor derived from the diffuse reflector scatter intensity discrepancy (Fig. 2.6(d)). In essence, the calibration factor derived from the diffuse reflector scatter intensity was the same as would be determined from the single slit diffraction pattern.

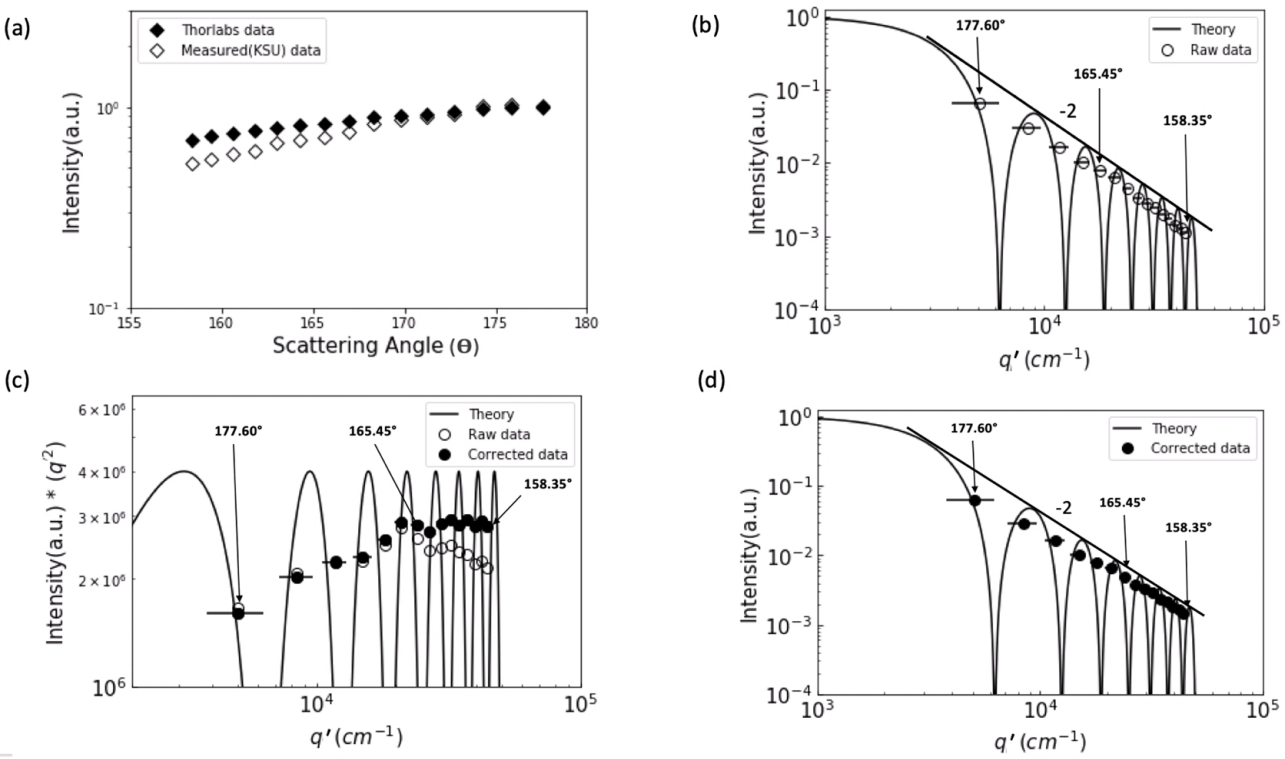

Figure 2.6: *Calibrating the backscattering setup by using (a) a glass diffuser such that measured data at KSU were compared with the Thorlabs measured data; (b) a 10-micorn wide, single slit diffracted intensity compared with the theoretically calculated, single slit diffraction pattern. (c) This shows the raw diffraction data and the diffraction data corrected by a factor derived from the diffuse reflector with theory on a magnified scale with* $I\times q^{'2}$. *(d) This again shows that the discrepancy is removed when the data is corrected by a factor obtained from the diffuse reflector scatter intensity discrepancy.*

2.3.4 Calibrating the Forward Scattering to Side Scattering

In order to calibrate the forward scattering to the side scattering, the direction of incident light was changed by a 6° angle such that the angles that correspond to each channel of the side scattering are decreased by that amount. That caused the side scattering angles to fall within the angle range of the forward scattering detector before the incident light direction

change. The experimental setup for connecting side scattering to the forward scattering is shown in Fig. 2.7. Two mirrors just after the laser source were used to change the direction of incident light by 6°. Scattering from an aerosol of water droplets was measured before and after the 6° change. The ratio of the scattered intensities in the overlap region near 10° yielded the calibration factor to connect the forward scattering to the side scattering.

The scattering intensities were measured from both the setups (Fig. 2.1 and Fig. 2.7) and by comparing the side scattering of both the setups, the calibration factors were determined for the channels on the side detector. The side scattering calibration is shown in Figs. 2.8(a) and 2.8(b). Figure 2.8(d) shows the completion of the side scattering calibration and connection of the forward scattering to the side scattering.

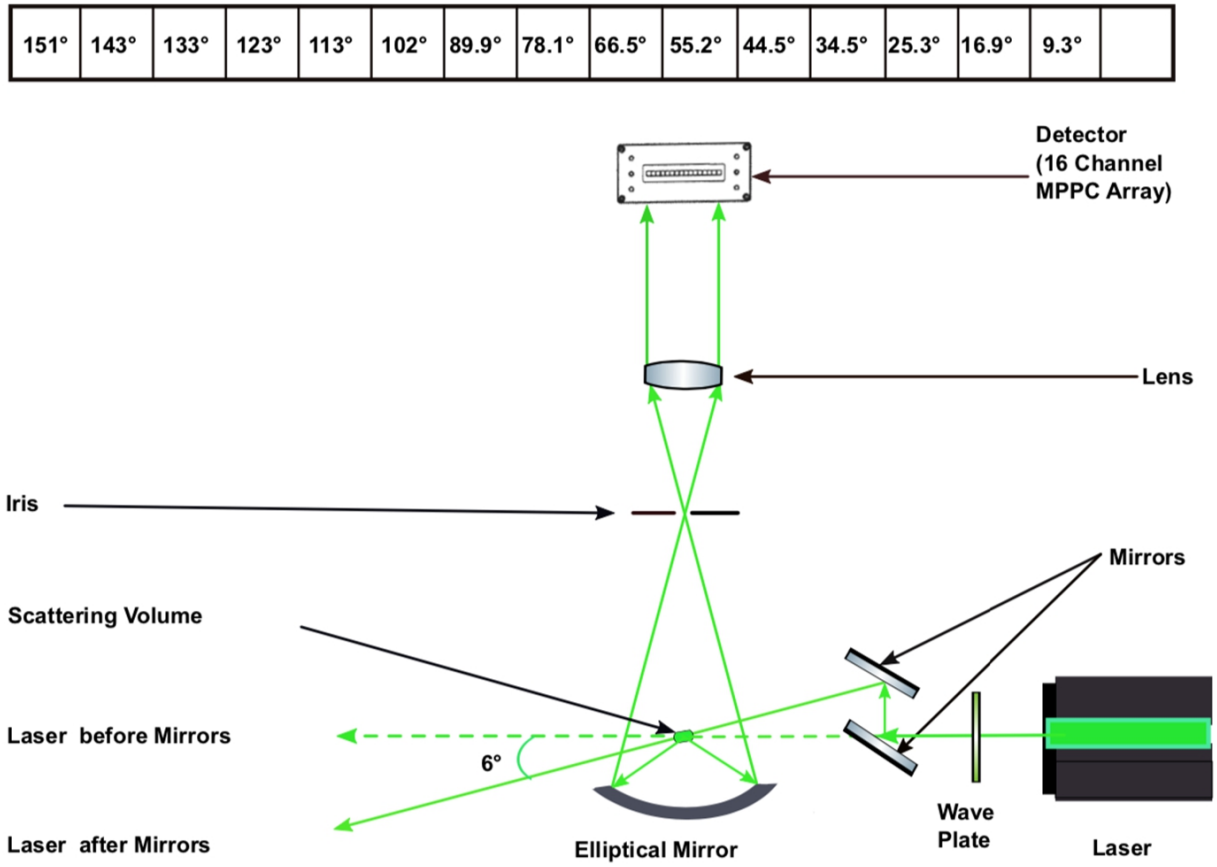

Figure 2.7: *A schematic diagram of the setup to connect forward scattering to the side scattering.*

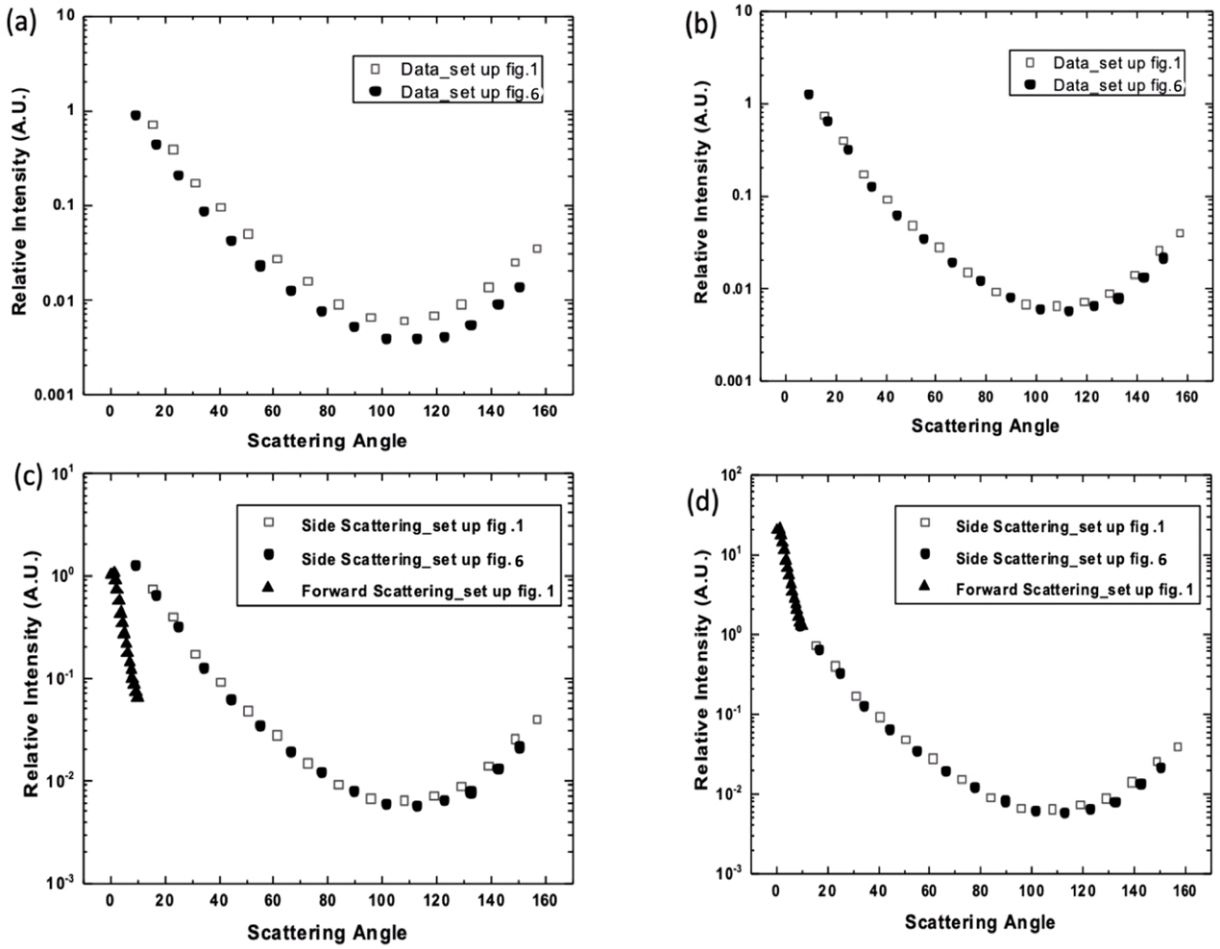

Figure 2.8: *Calibration to connect forward scattering to the side scattering by measuring the scattered intensity of the water droplets generated by a 6-jet collision nebulizer. Figures (a) and (b) show the calibration of side scattering and Figures (c) and (d) demonstrate calibrating (connecting) the forward scattering to the side scattering.*

2.3.5 Connecting Side Scattering to Backscattering

The same detector was used for the measurement of both the side scattering and back scattering. From the geometry of the setup and ray tracing, among 15 channels of the detector, the channel that corresponds to the largest angle for the side scattering becomes the channel for the smallest angle of the back scattering. The center angle for this channel differs

by 1.5° when calculated for side and back scattering, respectively. Since the channel has a certain angular width, such a small angle difference does not bring any noticeable difference in the magnitude of the measured scattered intensity. Thus, we can equate corresponding values that connect side scattering to the backscattering. Furthermore, the scattering intensity is mostly angle independent at that angle range, ensuring no need of any correction factor to connect side scattering to backscattering.

2.4 Analysis Method

This designed setup covered a wide-angle range from an extreme forward scattering to the backscattering regime, thereby yielding the wide-angle light scattering data. We now stress an important feature that our physical setup to include very small angles engenders, and that is to view the angular functionality in a geometric, rather than an arithmetic, manner. The prosaic approach of placing detectors uniformly (arithmetically) at, say, 10°, 20°, 30° and so on is fine for large angles, but as one descends with the same uniformity from 10° to 0°, a great deal is missed. Ideally, one might use 10°, 3°, 1°, 0.3°, and so on, a geometric progression, and thereby uncover a wealth of information, especially for large particles which scatter strongly in the forward direction. Such a progression might be practically difficult given the physical nature of multichannel array detectors, but this should not stop us from plotting our scattering data logarithmically to display the geometric functionality of light scattering that very often occurs.

With this point of view, we advocate plotting scattering data both linearly, when plotting versus the scattering angle, θ, and logarithmically when plotting versus the magnitude of the scattering wave vector q (cm^{-1}) given by the following relation,

$$q = 4\pi/\lambda Sin(\theta/2) \tag{2.1}$$

where $k = 2\pi/\lambda$ with λ is the vacuum wavelength of the light, and θ is the scattering angle.

We call this latter approach of scattered intensity versus q, log-log, "Q-space analysis" [15] . The Q-space analysis provides a simple and comprehensive description of scattering in terms of power-law with quantifiable exponents, whereas θ-space (versus scattering angle linearly) does not. However, we hasten to add that the Q-space analysis is explicitly not appropriate to study the last 60°–80° up to 180° of the scattering because the $Sin(\theta/2)$ functionality and the logarithmic plotting compress this region of the differential cross section to an extent that no details can be resolved. Thus, application of both the θ-space and Q-space analyses is needed to get a complete description of the scattering differential cross section. This double display of the data yields a comprehensive description of the scattering that neither plotting alone can give.

Figure 2.9 shows plotting the same scattering data by both methods. Left is data plotted in θ-space which showed no functionality in the forward scattering regime, but showed some functionality at the backscattering regime. However, the Q-space plot on the right uncovered a forward scattering regime, the Guinier regime followed by a power-law regime. At the backscattering regime in Q-space, all data points are compressed showing no functionality unlike the view from θ-space.

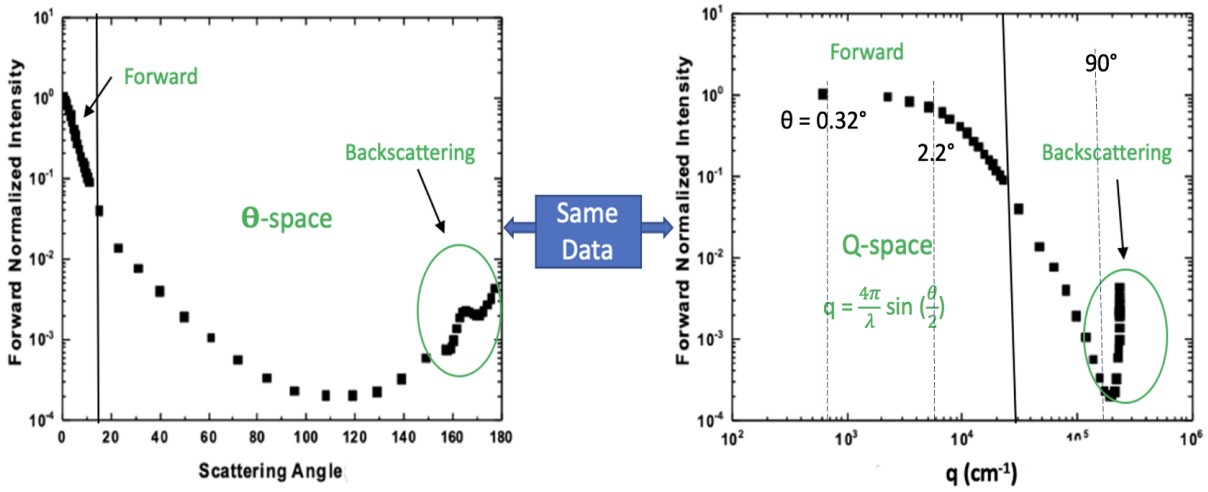

Figure 2.9: *Light scattered intensity normalized to unity at $\theta = 0.32°$, the smallest forward scattering angle, for an aerosol of water droplets generated by a 6-jet collision nebulizer, measured with the apparatus described in Fig. 2.1. Left is data plotted in θ-space which shows detail in the back direction; right is the same data plotted in Q-space which uncovers a forward scattering regime, a Guinier regime, and a power law. θ-space and Q-space give complimentary viewpoints for the scattering.*

2.5 Conclusions

We have designed and built a multi-angle light scattering set up for aerosols based on a novel optical scheme covering the scattering angle range from 0.32° to 177.6°, an extreme forward to the backscattering regime. This setup detected the scattered light from 31 channels (angles) simultaneously but overall 46 angles. Two multi-channel detectors are used for nearly simultaneous detection at all angles and inter-detector calibration methods are described. The entire setup is divided into three section namely: forward, side and backscattering regime. Calibration methods for each regime have been developed and described that demonstrate the efficacy of the setup. This setup allows the measurement of light scattering from a diverse size range of the particles including sizes approaching 20 microns. The

inclusion of small angles engenders the need for logarithmic plotting of the data versus the independent scattering variable. For that variable, we choose the magnitude of the scattering wave vector, q, a method we have called "Q-space analysis". However, a weakness of Q-space analysis is the compression of the data at large scattering angles, θ, where useful data also reside. Thus, we advocate plotting the scattered intensity versus linear θ as well, a method we herein choose to call "θ-space analysis". The combination of both viewpoints yields a comprehensive description of the scattering.

Chapter 3

A Light-Scattering Study of Highly Refractive, Irregularly Shaped MoS_2 Particles

The content of this chapter is based on Gautam and Sorensen [46].

3.1 Introduction

In this chapter, we present a light scattering study of aerosolized, micron sized, irregularly shaped, molybdenum disulfide (MoS_2) particles. We chose this material because it has rather extreme values of the real and imaginary parts of the refractive index, hence expanding the phase space of independent variables that control scattering that we have so far explored [19]. Furthermore, the important practical reason for all our work is that these particle types are common in the atmosphere, typically as dusts, and their light scattering and absorption properties play a significant role in the Earth's radiation budget [51–56]. Radiative forcing calculations generally rely on Mie theory which is rigorous for spherical particles only [5, 18]. Our work allows us to investigate questions that arise regarding the

nature of light scattering by highly refractive and absorptive irregularly shaped particles and how well Mie theory describes the scattering.

The complex refractive index for MoS_2 has been reported as m = n + iκ = 5.24 + i1.16 [57], 4.43 + i1.17 [58] and 4.41 + i0.63 [59] for the wavelength λ = 532 nm. We used a commercially available aerodynamic particle sizer spectrometer (APS 3321 (TSI)) to determine the size distribution of the aerosolized MoS_2 particles from which we scattered light. With this, we calculated the scattering using the Mie equations and compared that to the scattering data with some success. This analysis highlights the problems of an intensity weighted size distribution. In addition, we studied backscattering and showed that when the imaginary part of the refractive index κ is large compared to the inverse of the size parameter, $(2\pi \mathrm{R}/\ \lambda)^{-1}$, where R is the effective particle radius and λ is the optical wavelength; there is no enhancement in the backscattering. We applied both the conventional θ-space analysis and Q-space analysis methods to the experimentally measured data.

3.2 Experimental Method

The whole experimental setup was described in [25]. In addition to this, an aerodynamic particle sizer (APS 3321) has been used to measure the particle number size distributions. The APS 3321 had been calibrated by the manufacturer within 9 months prior to this experiment. Note that manufacturer recommends the APS 3321 be calibrated every 3 years. APS sheath and the aerosol flow rate were measured to be 4 $\pm$ 0.07 lpm and 1 $\pm$ 0.04 lpm, respectively. This is well within the range recommend by TSI. For analyzing the sizing accuracy of APS 3321, we used two different sizes of NIST traceable monodisperse polystyrene latex (PSL) spherical particles with manufacturer reported certified mean diameters 0.994 $\pm$ 0.021 μm and 6.15 $\pm$ 0.045 μm from Thermo Fisher Scientific, Waltham, MA, USA. We aerosolized PSL spheres using a nebulizer in combination with an aerosol diffusion dryer filled with silica gel as an absorbing agent. The APS measured sizes were found to be 0.98

$\pm$ 0.03 μm and 5.88 $\pm$ 0.1 μm, respectively. The differences between the manufacturer reported and the APS measured values are relatively minor to imply that our APS 3321 is measuring the particle size distribution correctly.

We calibrated the APS results with the light scattering by studying spherical silica (SiO_2) particles bought from US Research Nano-Materials. We did not scatter from PSL due to a low signal/noise ratio. The high sphericity of the silica particles makes them trustworthy subjects of the Mie calculations made for their measured size distribution; thus, they provide our benchmark for connecting the APS measured size distribution, the light scattering, and the Mie calculations made with the APS data. After calibrating our whole experimental system, we investigated the light scattering due to irregular molybdenum disulfide (MoS_2) particles.

TEM and an optical microscope were used to determine additional particle size and shape information. A theoretical Mie calculation of the scattering spectrum using the size distribution from the APS and the optical constant from prior published literature, is compared to the light scattering result. We apply Guinier analysis to test the consistency of the size measurement by light scattering with microscopy.

3.3 Results

3.3.1 Calibration of APS 3321 Measurements with Light Scattering

The manufacturer reported mean diameter for the silica particle is 0.82 μm. The size distribution of aerosolized silica was measured by the APS. The aerosol was collected at the light scattering volume. The volume equivalent sphere diameter is required for the Mie calculation. However, the APS instead measured the aerodynamic diameter. The volume

equivalent diameter (D_v) is related to the aerodynamic diameter (D_a) by [37, 60]

$$D_v = D_a\sqrt{\chi\rho_0/\rho_p} \tag{3.1}$$

where ρ_0 is the unit density ($1g/cc$), ρ_p is the particle density and χ is the aerodynamic shape factor of the particle. The aerodynamic shape factor is the ratio of drag force acting on a non-spherical particle to that of a spherical particle having the same volume and settling velocity (for a sphere, $\chi = 1$). For Eq. 3.1, we used $\chi = 1$ because the TEM pictures shown in Fig. 3.1 indicate that the particles are spherical in shape. Figure 3.2 shows the volume equivalent particle number distribution for the SiO_2 aerosol and their transformed light scattering intensity weighted distribution. The contribution of each particle in this weighted distribution will be proportional to the D^4, and the reasons for this weighting will be described below.

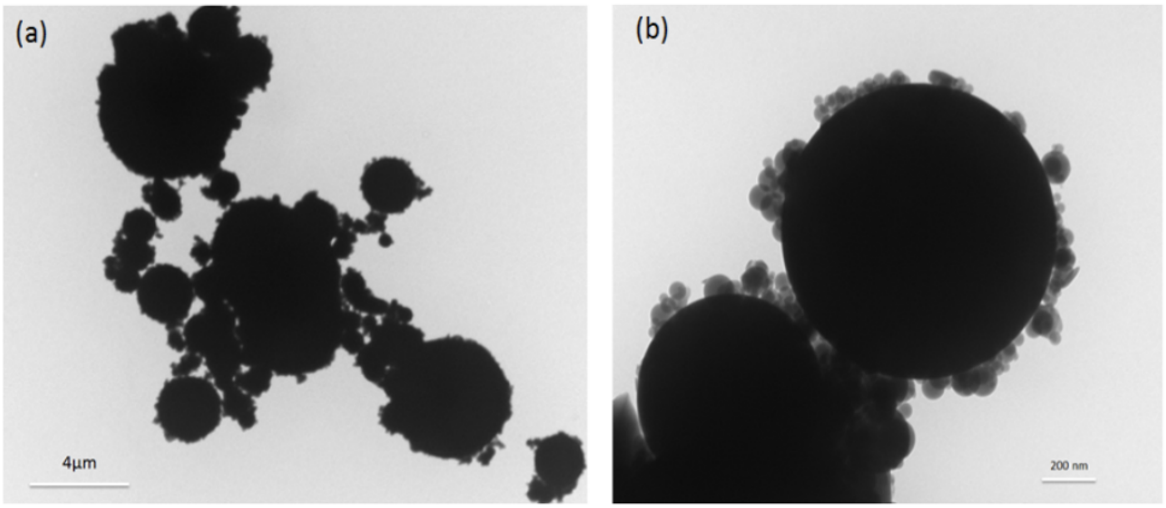

Figure 3.1: *Transmission electron microscope images for silica (SiO_2) particles.*

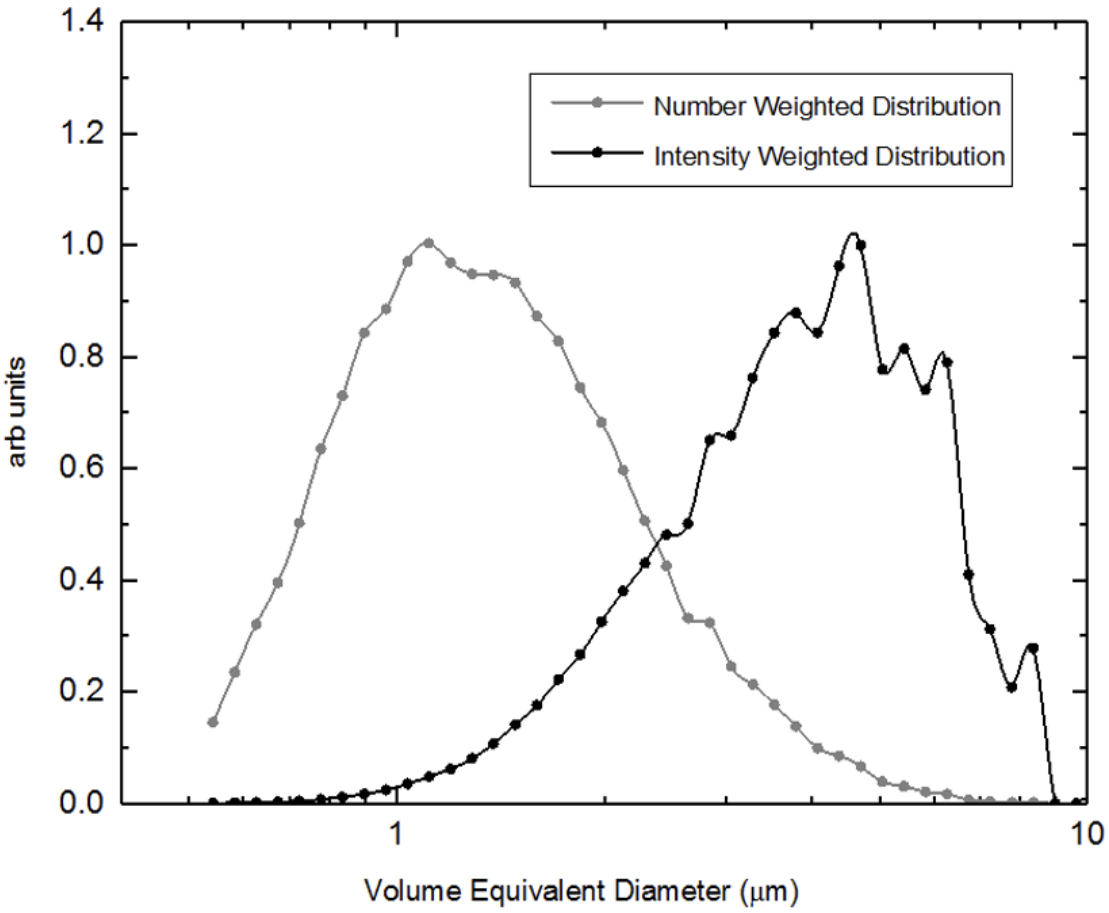

Figure 3.2: *Particle number distribution for the silica (SiO_2) particles measured with the APS 3321 after converting aerodynamic diameter (D_a) to the volume equivalent diameter (D_v) and its transformation to an intensity weighted distribution with a weighting factor of D^4.*

The volume equivalent particle number size distribution peaks at a diameter of 1.11 μm, and we used the corresponding radius for Mie calculations. The geometric standard deviation for this distribution was found to be $\sigma = 1.58$. With $\lambda = 532$ nm, the size parameter for the peak size is given by kR = 6.5. The refractive index for the silica particles is taken to be $m = \mathrm{n} + \mathrm{i}\kappa = 1.46 + \mathrm{i}0$ at $\lambda = 532$ nm [61]. With these parameters, the Mie calculations were performed and then compared to our experimental result as shown in Fig.

3.3.

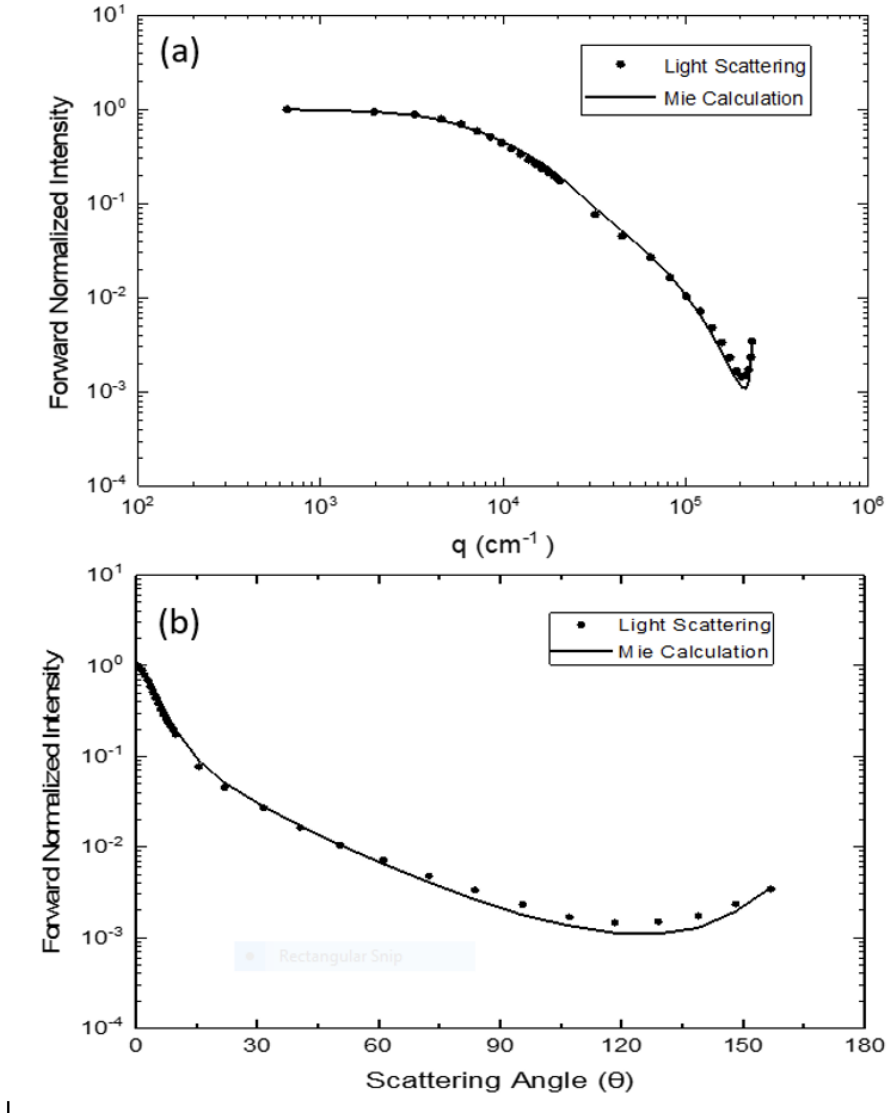

Figure 3.3: *Comparison of the experimentally observed forward normalized light scattering data with Mie calculations for APS observed silica (SiO_2) particle size distributions (a) plotted logarithmically versus q, the method of Q-space analysis, and (b) plotted linearly as a function of scattering angle, θ.*

Figure 3.3 shows that at a small angle range the Mie calculation and the data agree excellently. This angle range is least sensitive to the particle non-sphericity and its optical

constants. Further, Mie calculations underestimate the light scattering by a factor of 1.48 at angles around 125°. Note that the scattering in this region is about three orders of magnitude smaller than in the forward regime, hence prone to some uncertainty. Jaggard [62] and Mishchenko [63] showed a similar result when comparing Mie calculations for spheres and T–matrix calculations for spheroidal particles. The difference observed in our compared result may be due to nano-size silica attaching to the micron size silica particles (see in Fig. 3.1) thereby creating a distortion in sphericity. Overall, the Mie calculation for APS 3321 observed data agrees quite well with the experimental result.

The Q-space plot shows a constant forward scattering lobe at the smallest q. This is followed by a Guinier regime near $q \simeq R^{-1}$ where the q, hence angular, functionality begins. After that, there is a power law regime followed by a small dip that ends with enhanced backscattering. All this is typical of scattering from a polydisperse ensemble of spheres. From the Q-space plot, one can determine the radius of gyration, R_g, of any arbitrarily shaped particle via Guinier analysis [10] under the assumption of weak refractivity. The Guinier inferred radius of gyration is given by the Eq. 3.2 as follows:

$$I(q) = I(0)(1 - \frac{q^2 R_g^2}{3}) \tag{3.2}$$

where $I(q)$ is the scattering intensity, $I(0)$ is the forward scattering intensity and q is the magnitude of the scattering wave vector, Eq. 1.4. In principle, Guinier analysis is applicable for $qR_g < 1$. But one can exceed this limit with only minor error [64]. When qR_g is small, Eq. 3.2 can be written as

$$\frac{I(0)}{I(q)} = 1 + \frac{q^2 R_g^2}{3} \tag{3.3}$$

We performed the Guinier analysis for our experimentally observed result by plotting the inverse normalized intensity i.e.,$I(0)/I(q)$ versus q^2 as shown in Fig. 3.4. Equation 3.3 indicates that the Guinier plot should be a straight line with slope equal to $R_g^2/3$

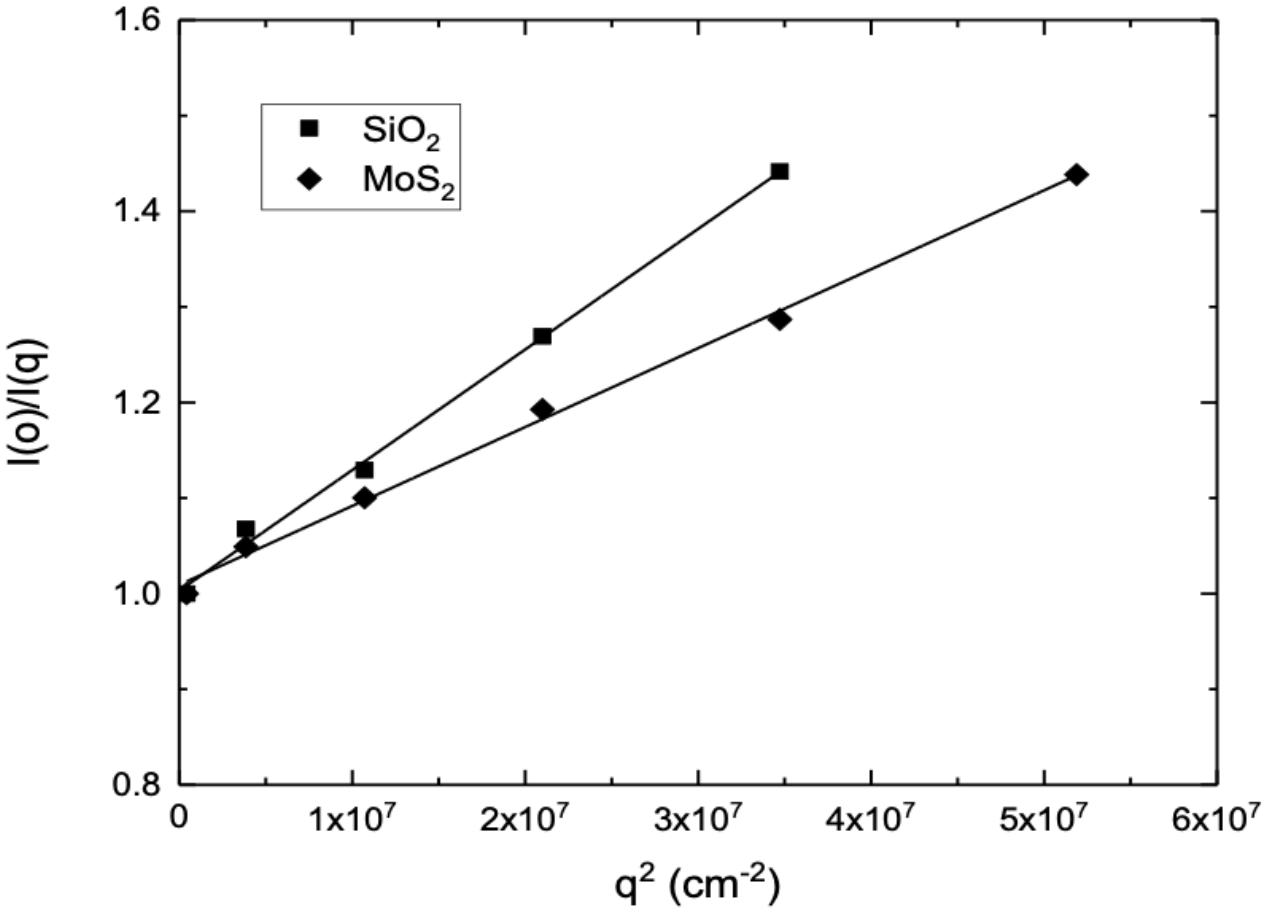

Figure 3.4: *Guinier Analysis of silica (SiO_2) particles (squares) and MoS_2 particles (diamonds).*

We find a measured radius of gyration of $R_g = 1.9$ μm. This suggests a sphere of radius R $=\sqrt{5/3}R_g = 1.29 \times 1.9 = 2.45$ μm, with a corresponding light scattering inferred diameter of D $= 4.9$ μm. TEM pictures shown in Fig. 3.1 indicate a broad size distribution of particles extending from the nanometer (e.g., 20 nm) range to the micron range. Micron size particles were measured to be around 1-6 μm, which is consistent with the light scattering inferred size because nanometer-size particles contribute negligibly to the light scattering in comparison to the micron size particles. More relevant is the APS observed most probable diameter because it sampled the aerosol at the optical scattering volume which was D $=$

1.11 μm, in poor agreement with the light scattering Guinier size. However, one must realize that light scattering favors the larger sizes of a distribution. The Guinier regime is in the forward scattering regime of the particulate scattering. In this regime, the scattering is proportional to the diameter of the fourth power, i.e., D^4 [14, 15]. To account for this the APS size distribution is multiplied by D^4 and then normalized to have a peak value of unity. This light scattering weighted size distribution is also plotted in Fig. 3.2. The results are dramatic (although perhaps not surprising). The minor large-size tail of the size distribution is emphasized and dominant while the most probable size at D = 1.11 μm is nearly inconsequential. The middle of the light scattering weighted distribution is between 4 and 5 μm, completely consistent with the Guinier inferred size.

The Guinier analysis comes with the caveat that it is accurate only in the diffraction limit when the phase shift parameter $\rho = 2\text{kR}|m-1| < 1$; i.e., weakly refractive particles. We have shown that the Guinier inferred radius of gyration, which was designated as $R_{g,G}$, is as much as 50% larger than the true radius of gyration when the phase shift parameter $\rho = 2\text{kR}|m-1| > 1$, and 12% larger in the $\rho >> 1$ limit [22]. The relationship between the true radius of gyration and Guinier's inferred size distribution with respect to the phase shift parameter is shown in Fig. 3.5.

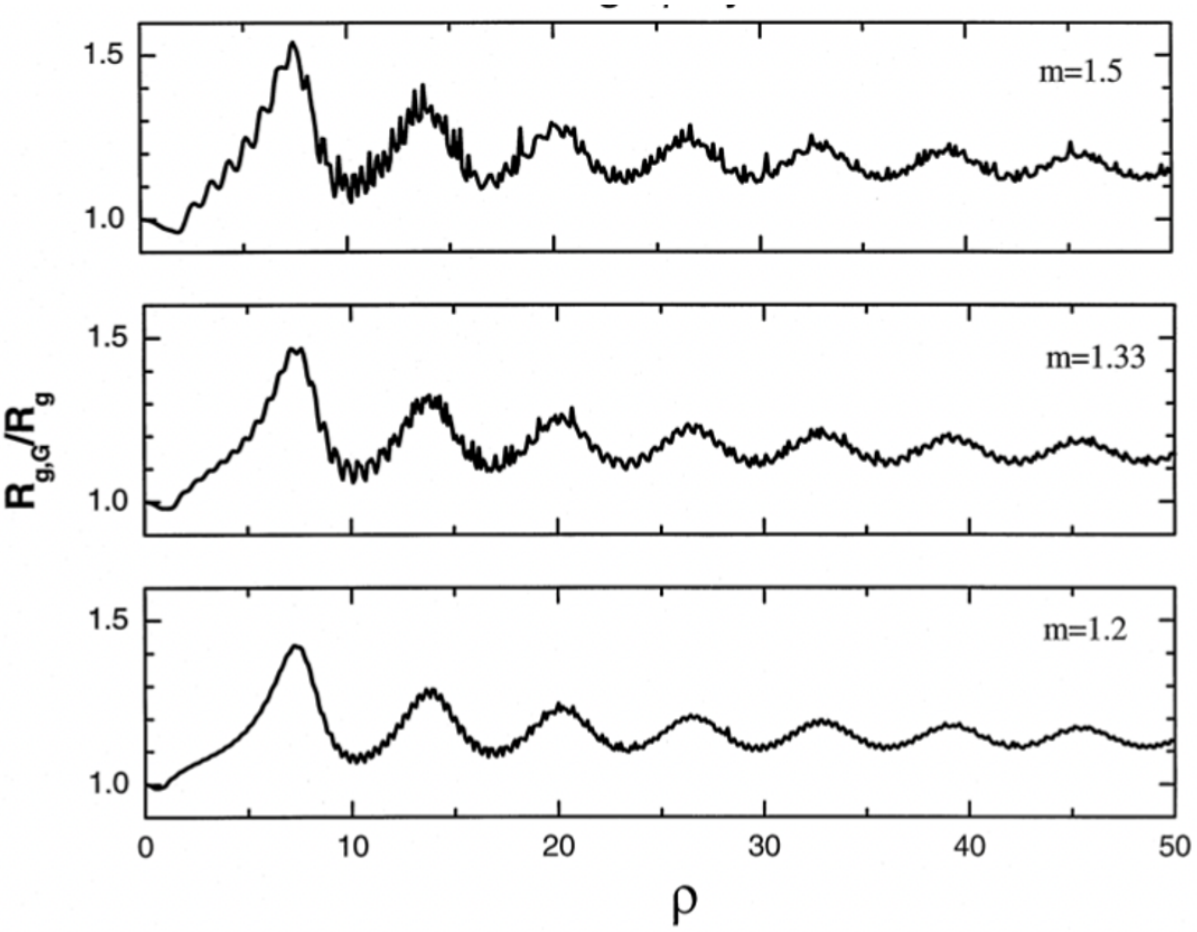

Figure 3.5: *The ratio of the Guinier inferred to real radius of gyration $R_{g,G}/Rg$ versus phase shift parameter (ρ) for spheres with three different refractive indices [22].*

.

We conclude by recognizing the semi-quantitative nature of our analysis. However, a good measurement with known caveats is better than no measurement at all. The major caveat here is the heavy weighting of light scattering in favor of the larger particles of a distribution. Moreover, there is considerable uncertainty in the large-size tail of the measured distribution because only a small fraction of the particles are there. This weighting is of utmost importance when comparing light scattering measurements to measurements made by the APS and similar devices, and will be important in our analysis below.

3.3.2 Light Scattering Results for Molybdenum Disulfide (MoS_2) Particles

After calibrating with SiO_2, we carried out the light scattering experiment for the MoS_2 particles. The MoS_2 particles were also bought from US Research Nano-Materials. The size distribution of MoS_2 was measured by the APS. Additionally, we used a TEM and an optical microscope to have more insight into particle shape and size. The TEM and optical pictures are shown in Fig. 3.6.

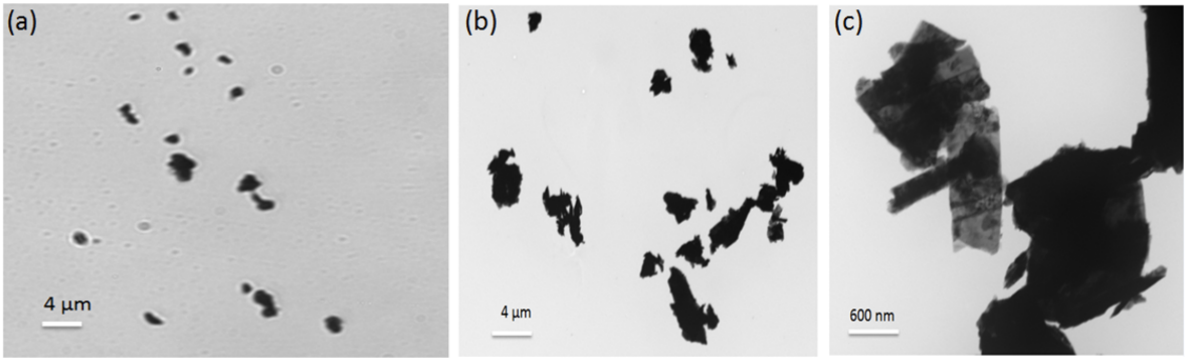

Figure 3.6: *The images of molybdenum disulfide (MoS_2) particles: (a) under an optical microscope and (b) and (c) under a transmission electron microscope (TEM).*

The measured aerodynamic diameters were converted to the volume equivalent diameters by using Eq. 3.1. Our MoS_2 particles look like Illite particles which have $\chi = 1.3$ [65]. So, we used a shape factor $\chi = 1.3$ in Eq. 3.1. Note that with the square root dependence for χ in Eq. 3.1, and the fact that χ is near unity for most shapes, uncertainties in χ are not significant for our work. Figure 3.7 shows the volume equivalent particle number distribution for MoS_2 and their transformed light scattering intensity weighted distribution. The number weighted distribution peaks around the diameter 1.13 ± 0.10 μm with a geometric standard deviation spread of $\sigma = 1.6$. The size parameter corresponding to this diameter is given by kR = 6.67.

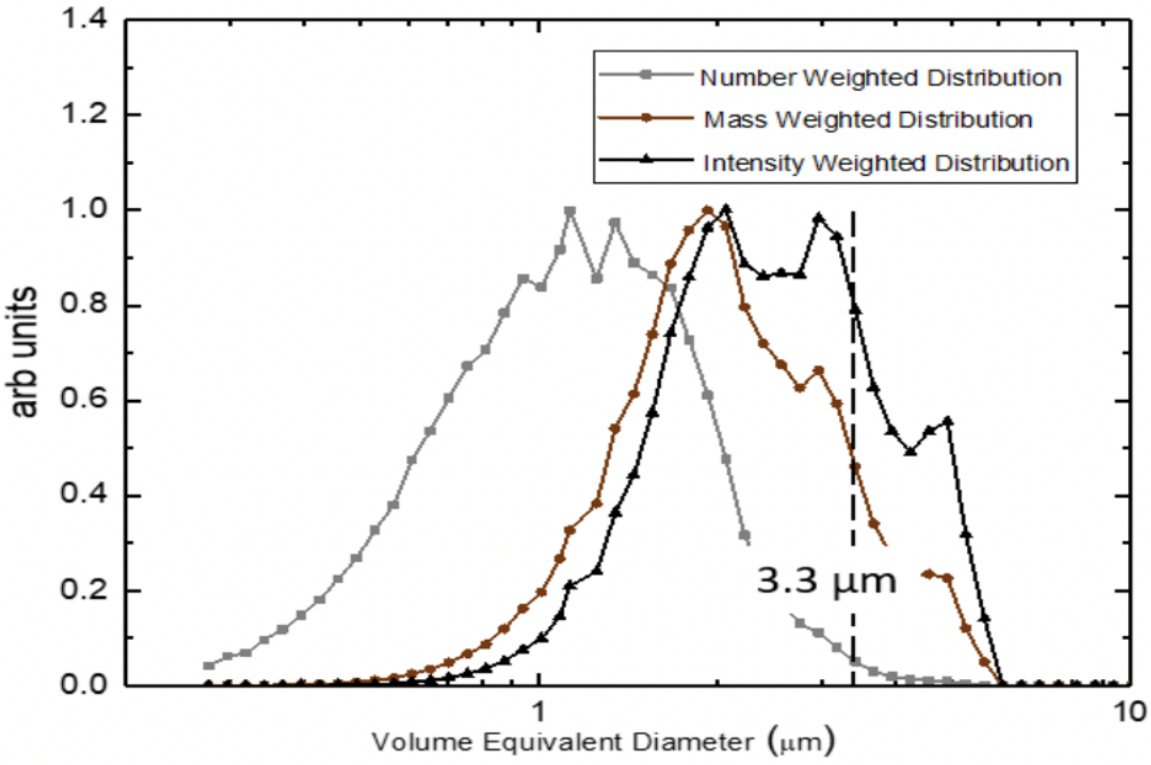

Figure 3.7: *Particle number (grey), mass (brown) and intensity weighted (black) distributions for the molybdenum disulfide (MoS_2) particles. Particle number distribution for the molybdenum disulfide (MoS_2) particles measured with the APS 3321 after converting aerodynamic diameter D_a to the volume equivalent diameter D_v and its transformation to mass and intensity weighted distribution with a weighting factor of D^3 and D^4, respectively. Dashed line marked D = 3.3 μm indicates the size determined by Guinier analysis of the light scattering data.*

The particle number distribution in Fig. 3.7 was used for Mie calculations with a refractive index of $m = \mathrm{n} + \mathrm{i}\kappa = 5.24 + \mathrm{i}1.16$ [57]. Using other reported values of m did not change calculations at small angles even though the imaginary refractive index κ differs by a factor of two across these values. However, we see a slight difference at larger angles. We have shown [66, 67] that effects of κ are effectively described by the parameter, κkR, the

product of the imaginary part of the refractive index and the size parameter. When κkR ≥ 0.1, κ starts to affect the scattering. Once the κkR ≥ 3, the effect of κ saturates. For all reported m, κkR > 3; thus, the choice between reported refractive indices is of small consequence for our calculations.

Figure 3.8 shows a comparison between Mie calculations and experimental results, plotted in Q-space (a) and the more conventional θ-space (b). The Q-space plot shows a forward scattering lobe and a Guinier regime, as for the spherical SiO_2 particles, but the subsequent power-law regime is ill-defined and there is no dip or enhanced backscattering. The conventional plot portrays more clearly the trend of the data in the larger scattering angle range. There is a close agreement between calculation and experiment in the small angle range, but the Mie result slightly underestimates the scattering at larger angles. Here it is valuable to recognize that when the parameter κkR is large, essentially all the light scattered energy is in the forward scattering regime [40]. With this perspective, we conclude that Mie theory successfully, but not exactly, describes the scattering, suggesting that the asphericity is rather insignificant for particles having a high refractive index.

Figure 3.8 also shows that there is no enhancement in the backscattering up to 157°. This is consistent with the theoretical result of Wang et al. [66] for spheres when κkR > 3. For our MoS_2 particles, we find below an intensity weighted diameter of D = 3.3 μm, hence κkR in the range of 12.5 to 22.75, depending on which of the three reported values of κ are used. These are very large values well in the saturated regime where no enhanced backscattering occurs. This result is in contrast to our previous work with irregularly shaped Arizona road dust [44] and abrasive, Al_2O_3 particles [68] that had significant backscattering but had small values of κkR.

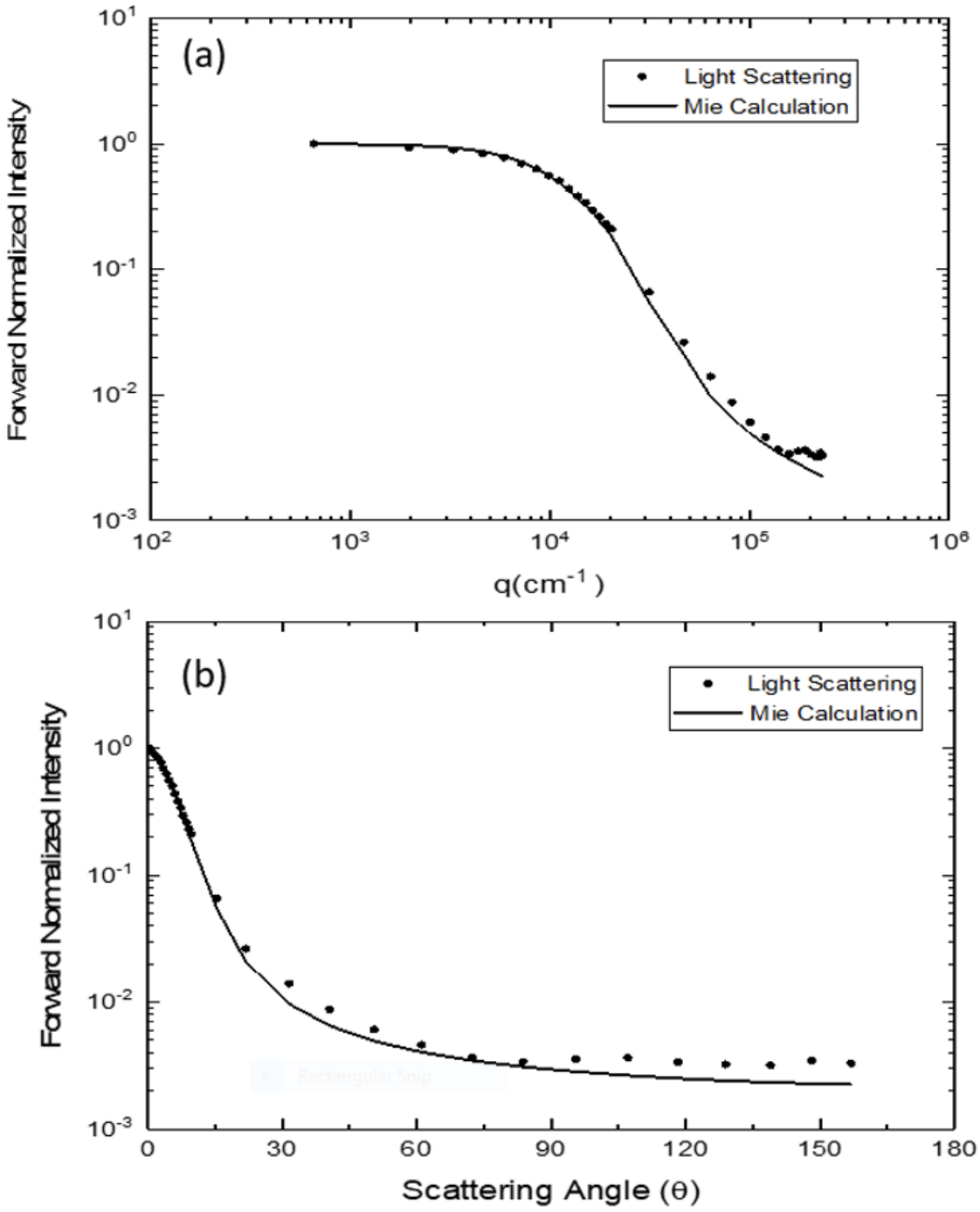

Figure 3.8: *Comparison of the experimentally observed forward normalized light scattering data with Mie calculations for APS observed molybdenum disulfide (MoS_2) particle size distributions (a) plotted logarithmically versus q, and (b) plotted linearly as a function of scattering angle, θ.*

Finally, the Q-space plot of Fig. 3.8 shows only a vague power law with q beyond the Guinier regime. This is in contrast to the results for Arizona road dust [44] which showed a strong power law for $\sim$ 1.5 orders of magnitude and the great many examples from the Amsterdam-Granada data set with our re-analysis [19, 69]. On the other hand, the Al_2O_3 abrasive particles showed only an ill-defined power law. We conclude that the issue of under what circumstances power laws in Q-space occur is uncertain.

Based on the Q-space plot, we applied Guinier analysis on MoS_2 data. Figure 3.4 includes the Guinier analysis, $I(0)/I(q)$ versus q^2 for MoS_2. The Guinier analysis shows the radius of gyration R_g to be 1.51 μm. By multiplying R_g by $\sqrt{5/3}$, the three-dimensional object equivalent radius becomes R = 1.9 μm. Thus, the light scattering determined diameter is D = 3.8 μm. This result is analogous to the results given above for the SiO_2 particles. The Guinier inferred size is not seen in the APS number distribution. On the other hand, the Guinier inferred size is consistent with the intensity weighted distribution, which is in the range D = 2 to 4 μm. However, as described above, the Guinier inferred radius of gyration is as much as 50 times larger than the true radius of gyration when $\rho >$ 1 [22]. For our MoS_2 at 532 nm, $\rho \approx 55$. At that value, $R_{g,G}$ is greater than R_g by around 12%. Reducing D = 3.8 μm by 12 leads to D = 3.3 μm, which is quite consistent with the sizes given by microscopic pictures in Fig. 3.6 and the intensity weighted distribution in Fig. 3.7.

It is useful to look at these Guinier results from the perspective that the Guinier equation was derived for X-ray scattering. X-rays have a refractive index of essentially one. Indeed, X-ray scattering is simply wave diffraction, the electromagnetic character is insignificant. Nevertheless, our results here show that the Guinier equation applied to light scattering from micron size, highly refractive particles still yield a valuable measure of the size, especially when one considers the difficulties in size measurements by other techniques.

3.4 Conclusion

In this chapter, we presented measurements of light scattering intensity from aerosolized, micron sized, irregularly shaped, molybdenum disulfide (MoS_2) particles in order to study the effects of a refractive index with high real and imaginary parts. Light scattering was measured over a range of angles from 0.32° to 157°. This experimental study showed that Mie calculations describe light scattering intensity quite accurately for highly refractive, irregular particles. We found that enhanced backscattering (to $\theta \leq 157°$) is not present when the parameter κkR is large; a result anticipated by theory. Theoretical calculations showed that when the quantity κkR, where $kR = 2\pi\mathrm{R}/\lambda$ is the size parameter, is greater than one, there is no enhancement in the backscattering. We demonstrated a good connection between light scattering and the size distribution of the aerosolized particles as measured by the aerodynamic particle sizer spectrometer. This connection showed that Guinier's analysis of light scattering yields intensity weighted mean sizes of reasonable accuracy for any shape and refractive index. This work also highlighted the rather sever implications of an intensity weighting of the size distribution.

Chapter 4

Light Scattering Study of Highly Absorptive, Non-fractal, Hematite Aggregates

The content of this chapter is based on Gautam and Sorensen [45].

4.1 Introduction

Iron oxide constitutes an important component of mineral dust particles, and these minerals are strong absorbers at visible wavelength. For example, hematite comprises up to 1% of Saharan dust and up to 2.6% of Icelandic dust by mass [70–74]. Furthermore, Hematite, an iron oxide mineral, is found in the Martian atmosphere and is believed to be the main component that gives Mars its orange color [32, 75, 76]. Hematite has a large absorption cross-section in comparison to other mineral aerosols [32, 70]. The way in which they scatter and absorb light plays an important role in climate forcing and climate models. Thus, scattering by such irregular particles is a problem of current interest. Another important characteristic of the hematite is that it is a birefringent material with significant

dispersion.

In this chapter, we present the angular distribution of the light scattering due to hematite particles. This work is focused mainly on the backscatter region. The backscattering region is more sensitive to particle shape irregularities and heterogeneities than the forward scattering region [7]. Moreover, the result presented in this chapter demonstrates the importance of Q-space over the θ-space analysis as well as emphasizes the importance of plotting the scattering data by both methods. Scanning electron microscope images and Ultra Small-angle X-ray Scattering (USAXS) data show that hematite particles are uniform, non-fractal aggregates.

4.2 Sample Characterization

Scanning Electron Microscope (SEM) and optical microscope images of the hematite sample are given in Fig. 4.1. SEM shows the hematite sample is bimodal with aggregates as large as 10 μm. The aggregates are composed of small grains, monomers, that look like rounded polyhedrons with a mean diameter of 2a $\simeq$ 200 nm. The optical microscope pictures in Fig. 4.1(d) were created by blowing the hematite into a 17 L chamber in a manner very similar to that which blows the particles through the optical scattering volume. The aerosol was allowed to settle with time onto microscope slides at the bottom of the chamber. Thus, this picture represents the light scattering aerosol, and that aerosol is seen to be bimodal with mode sizes (rough diameters) of approximately 1 and 10 μm dominated in number by the smaller size.

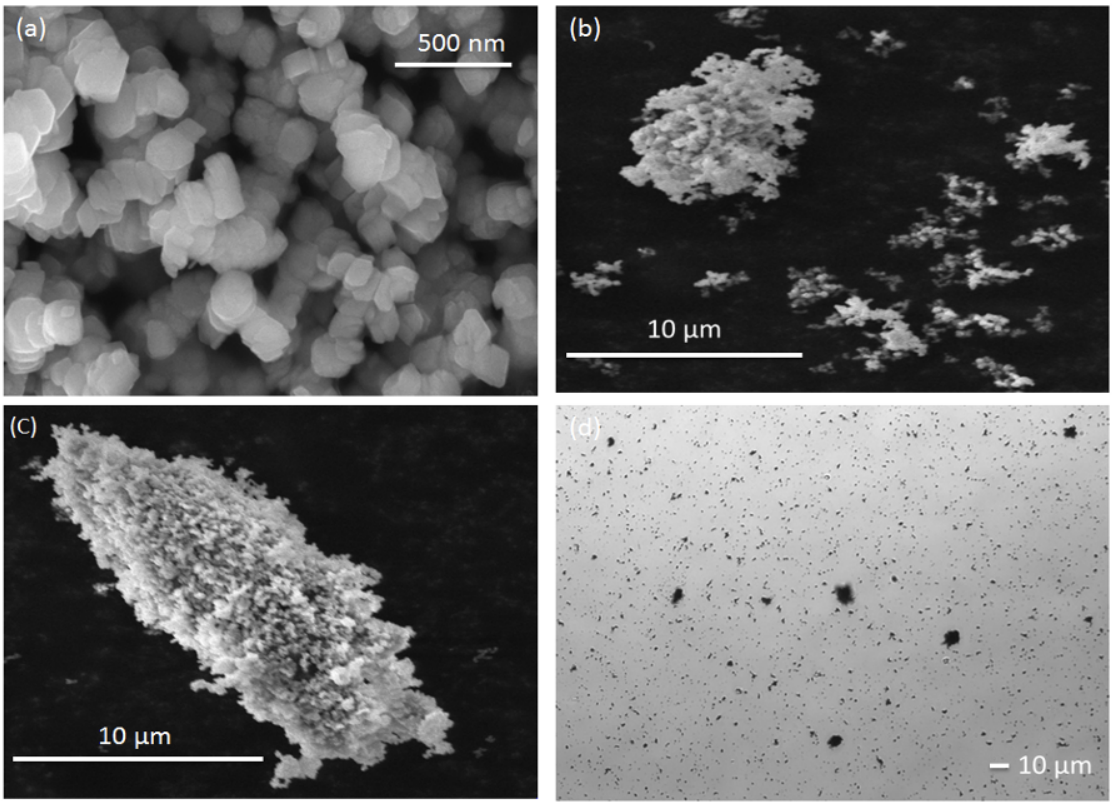

Figure 4.1: *The images of hematite (Fe_2O_3) particles: (a), (b) and (c) under a scanning electron microscope (SEM) and (d) under an optical microscope.*

The SEM pictures show that the larger hematite particles are aggregated in nature; but to identify the nature of aggregates, we performed Ultra Small-Angle X-ray Scattering (USAXS) to determine the structure factor S(q) of the particles [77]. The result displayed in Fig. 4.2 shows two Porod regimes with slope -4 to indicate power laws $S(q) \sim q^{-4}$. Most generally, the magnitude of the Porod exponent is $D_p = 2D_m - D_s$ [50], whereD_m and D_s are the mass and surface scaling dimensions, respectively. These exponents describe the power-law scaling of an object's mass with an overall linear size like the mean radius. A value of $D_p = 4$ implies that (not uniquely) $D_m = 3$ and $D_s = 2$ to indicate non-fractal, "three dimensional", objects.

To model the USAXS result, and thereby gain more insight into the structure of the aggregates, we used a variation of the Eden growth model to create aggregates [78]. Three model aggregates were grown into spherical volumes of radii 8, 10, and 12 μm with a monomer size of radius a =100 nm until a volume fraction of 0.3 was reached. This volume fraction was determined by massing the real sample with and without a penetrating liquid medium. The model aggregates were discretized and placed onto a cubic lattice with a point spacing of 20 nm. To compare with the USAXS data, the real space coordinates of the model aggregates were Fourier transformed into the reciprocal q-space. The scattered intensity is proportional to the square of the Fourier transformed real space coordinates, which is the structure factor, and for a discretized system it is given by [79]

$$S(\vec{q}) = \sum_{l,j}^{N} e^{i\vec{q}.(\vec{r_l} - \vec{r_j})} \tag{4.1}$$

where $\vec{r_l}$ and $\vec{r_j}$ are the position vectors of the l^{th} and j^{th} points within the aggregate, respectively, and N is the number of points that the aggregate has been discretized into.

The average of the structure factors for the spherical volumes of radii 8, 10, and 12 μm is shown in Fig. 4.2. The average structure factor is used to minimize the diffraction ripple structure. In Fig. 4.2, it can be seen that the calculated structure factor and USAXS data agree very well at small q, which corresponds to the length scales of the aggregates until inverse q (which is a length) becomes comparable with the monomer size. The disagreement at larger q comes about due to the use of a single monomer size. The use of a single-sized monomer yields a form factor for the monomer with a ripple structure. Nevertheless, the envelope of the form factor at large q shows a slope of -4 consistent with the USAXS data. Given the fairly uniform morphology of the aggregates seen in Fig. 4.1, the USAXS data, and our successful modeling of the data, we conclude that the hematite aggregates are not fractal and have mass and surface scaling dimensions of $D_m = 3$ and $D_s = 2$, respectively.

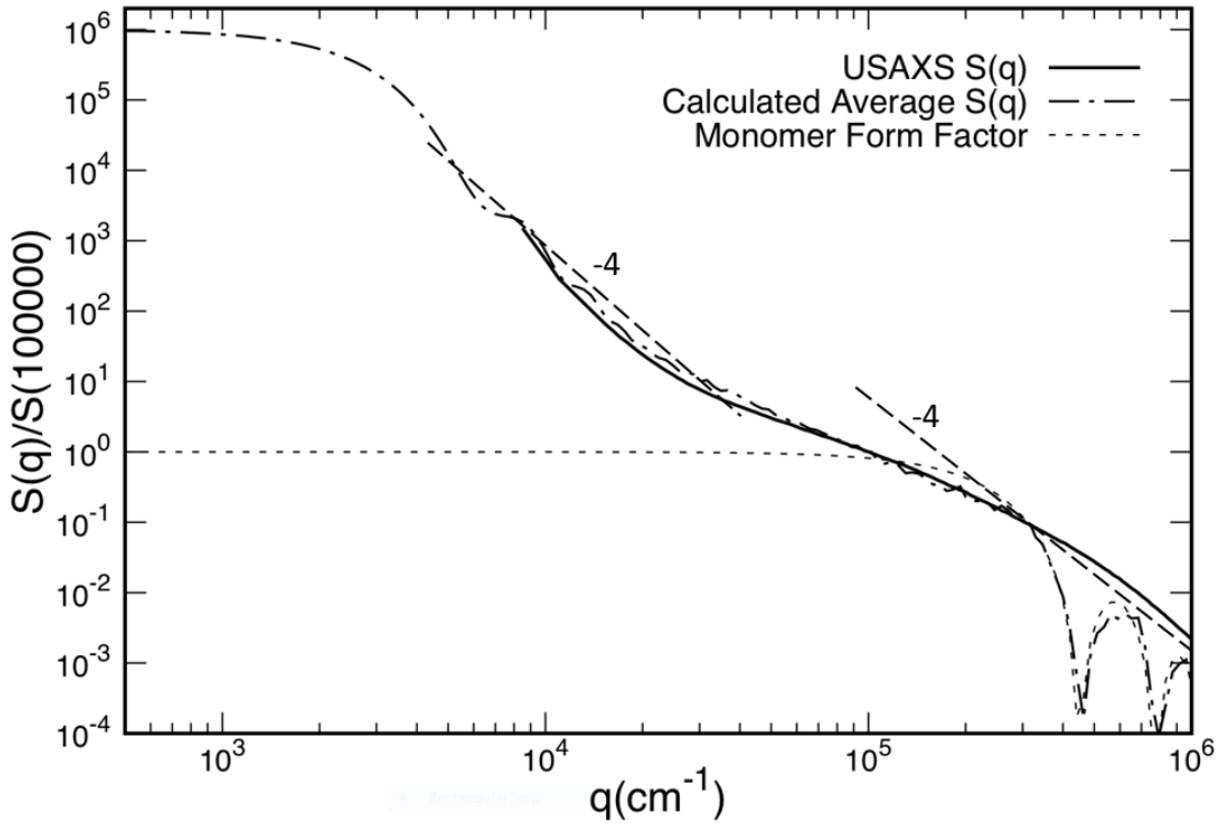

Figure 4.2: *Ultra Small-Angle X-ray Scattering (USAXS) data, solid line, for the structure factor S(q) of the hematite. Power laws of* q^{-4} *at large and small q values indicate that the primary (monomers) and aggregated particles, respectively, have mass scaling dimension* $D_m = 3$ *and surface scaling dimension* $D_s = 2$*. This implies a non-fractal nature of both the aggregates and, not surprisingly, the monomers.*

To conclude our sample characterization, it is known that Hematite is a birefringent material. The real and imaginary values of the refractive index for the extraordinary ray is $n = 2.8$ and $\kappa = 0.5$ and for the ordinary ray is $n = 3.2$ and $\kappa = 0.5$, respectively, for $\lambda =$ 532 nm [70], which is based on the previous work by [80]. In our calculations, we used the refractive index $m = n + \mathrm{i}\kappa = 3 + \mathrm{i}0.5$, the average values of extraordinary and ordinary rays; weighted equally [32, 81].

4.3 Results

The experimental scattered intensity plotted versus q on a double logarithmic scale, Q-space analysis, is shown in Fig. 4.3(a). This is normalized to 1 at the smallest measuring angle of 0.3° ("forward normalized"). Three notable features are observed: 1) an extended Guinier regime in the range 103 cm^{-1} < q < 104 cm^{-1} with two Guinier crossovers, 2) a short power-law regime with exponent -3, and 3) enhanced backscattering at large q corresponding to angles of $\theta = 129°$, 139°, 149° and 157°. It is this backscattering feature that is the major subject of this paper. Figure 4.3(b) shows the same data plotted versus linear scattering angle, θ,in the conventional manner. Non-descript curve results were unable to resolve the two Guinier regimes and the power law.

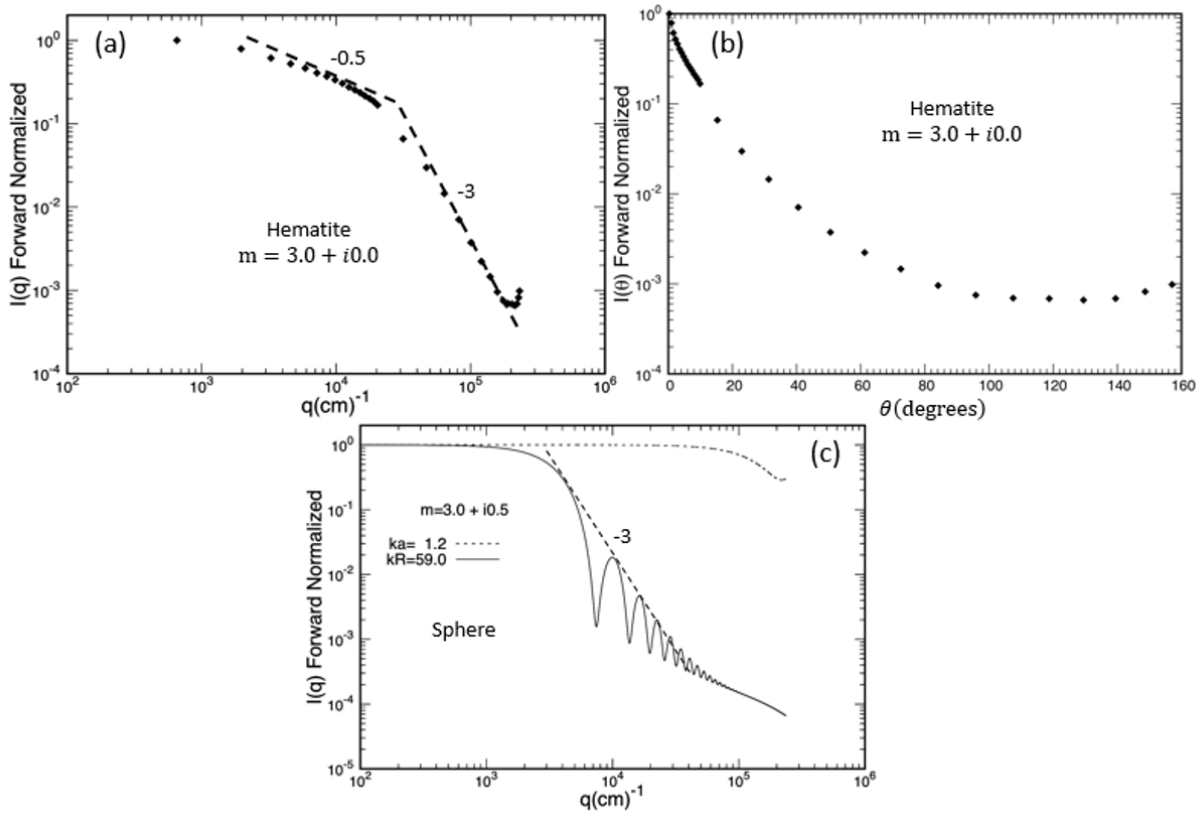

Figure 4.3: *(a) Forward normalized scattered intensity data versus q plotted double logarithmically (Q-space analysis) of the light scattered intensity of the hematite aggregate particles observed experimentally, (b) same data plotted versus linear scattering angle , and (c) Forward normalized Mie scattered intensity for a sphere with a radius $R = 1.2\ \mu m$ similar to the hematite aggregate particles, solid line, and spherical hematite grains of radius $a = 100$ nm, dashed line. Sphere size parameters, kR and ka, are given. Dashed lines indicate power laws with slope designated.*

An explanation of the first feature lies with the bimodal size distribution seen in Figs. 4.1(b) and 4.1(d). Q-space analysis facilitates the determination of the size of any shape of particles via Guinier analysis [10, 22]. For our purposes here, a complete Guinier analysis is not necessary. Instead, we will use the fact that the Guinier regime is an inflection of the

slope of I(q) versus q when plotted double logarithmically, typically at small q to imply a length scale equal to the inverse of the q value at the crossover. The data in Fig. 4.3(a) suggest two inflections due to two length scales [82]. The first inflection is at $q \simeq 103\ cm^{-1}$ to imply a length scale of $q^{-1} \simeq 10\ \mu$m and the second inflection is at q $\simeq 104\ cm^{-1}$ to imply a length scale of $q^{-1} \simeq 1\ \mu$m. These semi-quantitative length scales are consistent with the bimodality depicted in Figs. 4.1(b) and 4.1(d). Note that this bimodality is essentially impossible to see in the data when been plotted versus linear scattering angle, Fig. 4.3(b).

An explanation of the second feature, the brief power law, lies with the large refractive index of hematite. We have shown that for spheres with large real and imaginary parts to the refractive index the scattering limits to a Fraunhofer diffraction pattern for a circular aperture or, by Babinet's principle, circular obstacle [23]. This is particularly true when the product of the imaginary refractive index and the size parameter, κkR, is large. The parameter κkR [66] is the ratio of the particle radius to the optical penetration depth, such that when $\kappa\text{kR} \geq 3$, the incident light barely penetrates the object and a particle acts as an opaque object. Ignoring the ripples, all diffraction patterns have a constant scattered intensity at small q followed by a crossover Guinier regime, and then at largest q, a power-law Porod regime, which is an envelope for the ripples with q^{-D_p} functionality. A Porod exponent of $D_p = 3$ results for any shape with mass and surface scaling dimensions or $D_m = 2$ and $D_s = 1$, respectively (recall from above $D_p = 2D_m - D_s$). The fact that the hematite aggregates have mass and surface scaling dimensions of $D_m = 3$ and $D_s = 2$, respectively, means that their projections will have $D_m = 2$ and $D_s = 1$, so that their diffraction patterns will have Porod exponents of $D_p = 3$. This explains the observed power law.

Given all this, we calculated circular aperture diffraction patterns for radii of 1 and 10 μm and averaged them over a minor size distribution to eliminate the ripple structure. We added these together and adjusted the relative intensities to yield a power law of slope -0.5 between the two Guinier regimes, as seen in the data, Fig. 4.3(a). The results are shown in Fig. 4.4, and are seen to replicate the data in Fig. 4.3(a), except for the enhanced

backscattering. Given that the scattering in this regime of size and refractive index is proportional to the diameter to the fourth power, the implication is that there are 10^4 more small particles than big ones. This is consistent with Fig. 4.1(d).

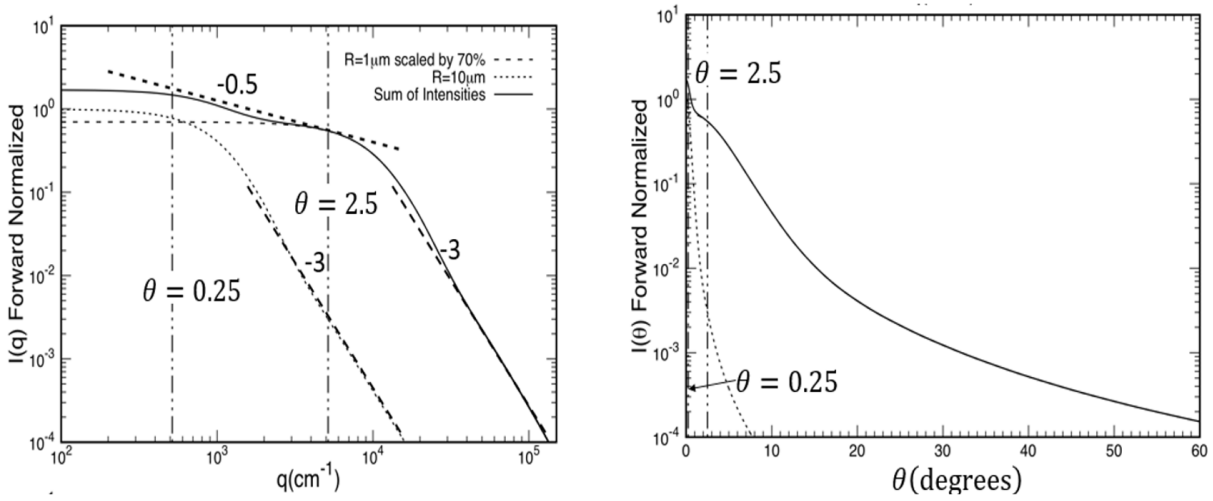

Figure 4.4: *Forward normalized circular aperture diffraction pattern envelopes for radii of 1 μm and 10 μm. Left: versus q plotted double logarithmically (Q-space analysis); Right: versus the scattering angle, θ. Both plots indicate scattering angles of 0.25° and 2.5° with vertical dash-double-dot lines. The two individual Q-space analysis plots for R = 1 μm and 10 μm show a single inflexion at the Guinier regime, a power-law envelope of q^{-3} with no enhanced backscattering. The sum of intensities for these two plots shows an extended Guinier regime with slope -0.5 followed by a power-law envelope of q^{-3}. Note that these features are not apparent in the normal plotting of scattered intensity versus linear scattering angle.*

It is interesting to compare this conclusion to the USAXS analysis. In the USAXS analysis, the large size mode of the bimodal size distribution with radii on the order of R $\simeq$ 10 μm dominated the X-ray scattering. In the analysis of the light scattering in Fig. 4.4, the small size mode of the bimodal size distribution with radii on the order of 1 μm dominated the light scattering. The difference lies in the fact that the refractive index for X-rays is

nearly unity with no imaginary part. Then the scattering lies in the Rayleigh-Debye-Gans limit where the forward scattering is proportional to R^6. On the other hand, large refractive particles, like our hematite, are in a regime of scattering for which the forward scattering is proportional to R^4. This difference in size functionality applied to our particular bimodal size distribution shifts the dominance of one mode over the other between the two sets of data.

The rest of this paper considers the third feature, the enhanced backscattering at large q. Our light scattering results are compared to the results of Mie calculation for a sphere with the same perimeter radius of the hematite particles in Fig. 4.3(c). For the Mie calculations, we took $R = 1.2$ μm, the approximate size for aggregate hematite particles inferred from microscopy measurements. This radius corresponds to a size parameter of $kR = 2\pi R/\lambda = 14.2$. The size parameter of the grain is ka = 1.2, where $a = 100$ nm. Figure 4.3(c) shows that the hematite size equivalent sphere has no enhanced backscattering, while the single grain does. This can be explained with the parameter κkR [66, 83], which for the sphere is κkR = 7.1, a very large value, such that enhanced backscattering is not observed. On the other hand, for the grain κka = 0.6 which is small enough to allow for enhanced backscattering, and indeed, the Mie calculation in Fig. 4.3 indicates that this is true. However, the data in Fig. 4.3(a) indicate that hematite aggregates with the same size as the sphere show enhanced backscattering. Accordingly, we can speculate that the backscattering of the aggregate is either due to the grains in the aggregate particles or the aggregate structure.

4.4 Theoretical Calculations

Investigations of backscattering phenomena by aggregates are "neither few nor small" [84–90]. These studies are mostly theoretical, and essentially all see enhanced backscattering beyond scattering angles of ca.140°, as do we with Hematite. However, these previous studies are oriented towards astrophysical situations such as lunar and planetary

regolith's, cometary dust, etc. Hence the refractive indices are significantly smaller than that of Hematite. Given this, we have performed our own theoretical calculations directly relevant to our experimental work.

To study the effects of the hematite aggregate structure on the light scattering we simulated the hematite aggregates with the variant Eden growth model aggregates described above to fit the USAXS data. An example is shown in Fig. 4.5. Then the light scattering was calculated using the T-matrix method [91]. Given the size information in Fig. 4.1, our Guinier analysis in Fig. 4.4, and consideration of computational time constraints, we studied a spherical volume of radius $R = 1.2$ μm. The monomers were spherical with radii of $a = 100$ nm, which is equivalent to the size of the hematite grains. The number of monomers inside the diameter 2.4 μm spherical volume was varied from N = 30 to N = 692, thereby yielding particle volume fractions from $f_v = 0.017$ to $f_v = 0.40$. The light wavelength used was $\lambda = 532$ nm. The incident light was linearly polarized perpendicular to the scattering plane. Figure 4.6 shows the results of these calculations for a monomer refractive index of $m = 3 + i0.0$, Fig. 4.7 shows the for a monomer refractive index of $m = 3 + i0.5$, the refractive index of hematite at $\lambda = 532$nm, and Fig. 4.8 shows results for $m = 3 + i1.0$.

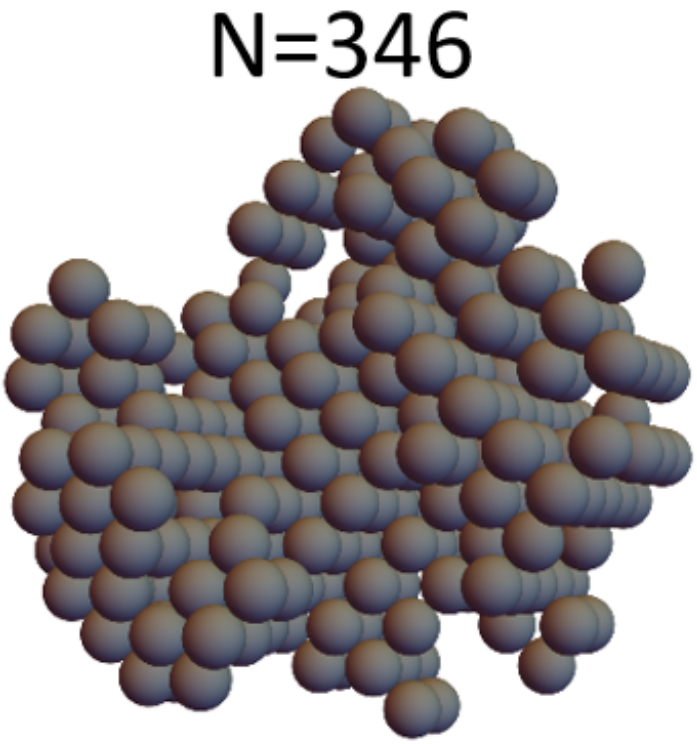

Figure 4.5: *An example of the variant Eden growth model aggregates use for the T-matrix calculations.*

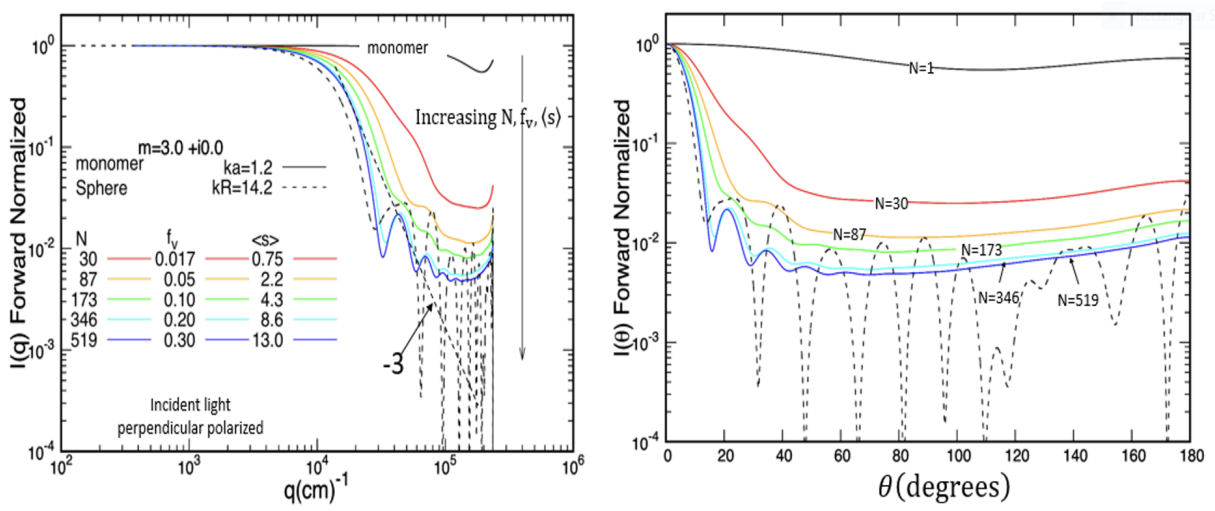

Figure 4.6: *Calculated forward normalized scattered intensity for an aggregate formed as a spherical volume with a diameter of 2.4 μm with N randomly distributed spherical monomers of diameter 2a = 200 nm within. Left: versus q plotted double logarithmically (Q-space analysis); Right: versus the scattering angle, θ. The corresponding monomer particle volume fractions are denoted by f_v. The monomers have a refractive index of m = 3 + i0.0. The light wavelength is λ = 532 nm linearly polarized perpendicular to the scattering plane. The average number of scattering events within the aggregate volume is <s>, see Eq. 4.3, below. Also shown is the scattering for a single monomer and for a solid sphere with a diameter D = 2.4 μm. The dashed line indicates a slope of -3.*

Figure 4.7 clearly shows that the simulated aggregates with $m = 3 + i0.5$ mimic well the enhanced backscattering of the hematite data, Fig. 4.3(a). This figure also shows that a same size sphere with the same refractive indices displays no enhanced backscattering. However, a single monomer grain still shows enhanced backscattering. Thus, we ask: is the enhanced backscattering of the aggregate due to the aggregate's structure or related to the enhanced backscattering of the grains?

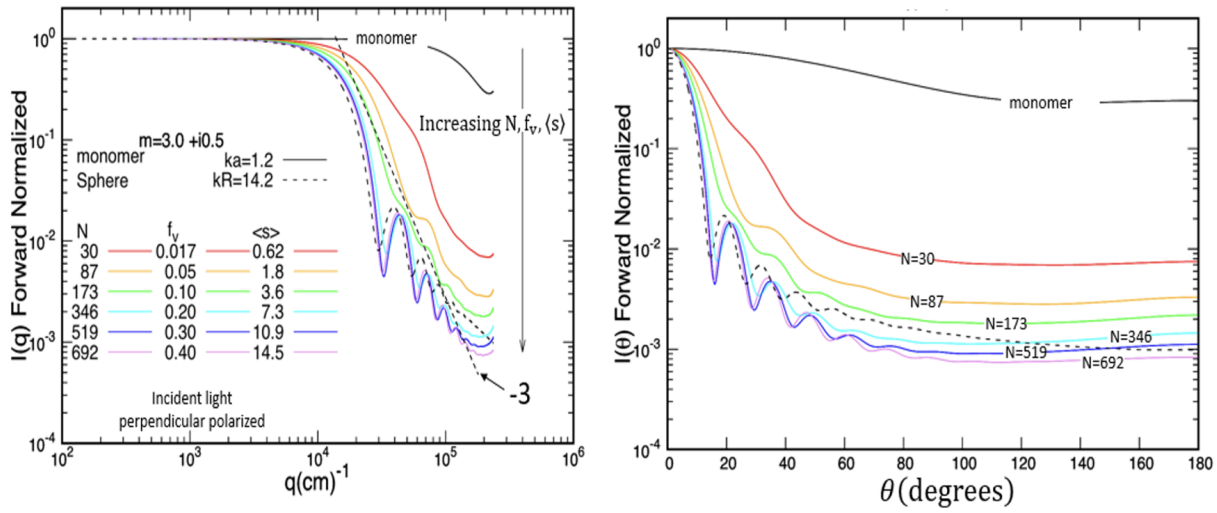

Figure 4.7: *Same as Fig. 4.6 except m = 3 + i0.5, the refractive index of hematite.*

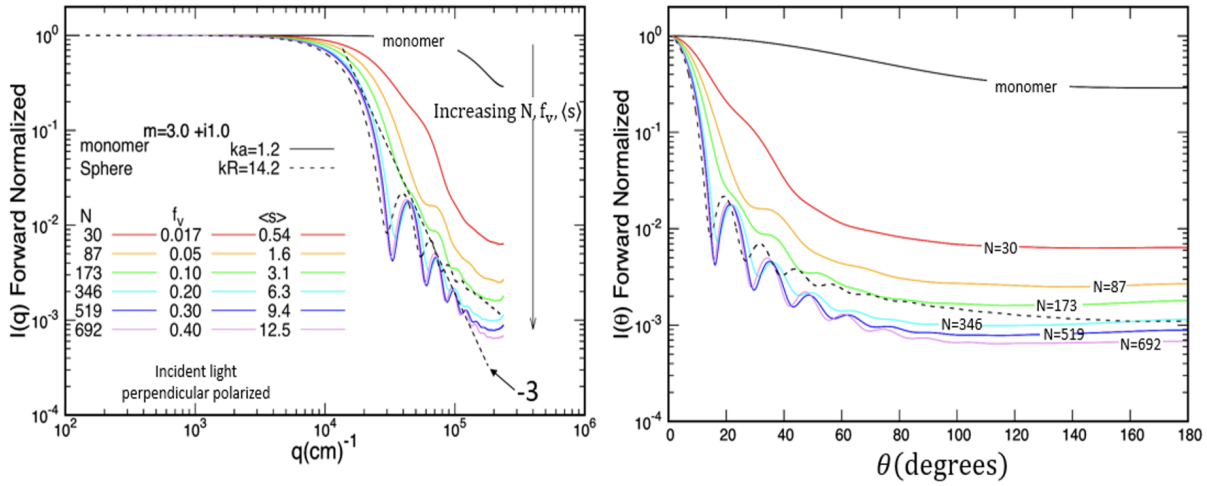

Figure 4.8: *Same as Figs. 4.6 and 4.7 except m = 3 + i1.0.*

The systematic study displayed in Figs. 4.6 to 4.8 used two variables: 1) a wide range of monomer volume fractions inside the spherical volume to explore the effect of the aggregate structure and 2) the grain refractive index imaginary part varied as $\kappa = 0.0$, 0.5 to 1.0. This change led the parameter κka of the grain to range from 0.0 to 0.6 and to 1.2 and yielded significant, moderate and no enhanced backscattering by the monomer grain respectively,

see Figs.4.6 to 4.8.

Figure 4.6 uses $m = 3 + i0.0$. The monomer, the same size solid sphere and the aggregates all show enhanced backscattering. As described above, Fig. 4.7 for $m = 3 + i0.5$ shows modest enhanced backscattering for the monomer, no enhanced backscattering for the solid sphere, and enhanced backscattering for the aggregate. Figure 4.8 uses $m = 3 + i1.0$ to find no enhanced backscattering for the monomer, no enhanced backscattering for the solid sphere, and enhanced backscattering for the aggregate. Thus, while the imaginary part of the refractive index quenched the enhanced backscattering in the monomer and the same sized sphere, the enhanced backscattering remained in the aggregates. We conclude that the enhanced backscattering from the aggregate is due to the aggregate structure. This is a direct result of Maxwell's equations which are the foundation of the computational method used.

Close inspection of Figs. 4.6 to 4.8 show that a larger imaginary part κ does cause smaller enhanced backscattering for the aggregates. This could be an augmentation of the aggregate-based backscattering with the monomer backscattering or lack of it. One also observes that the enhanced backscattering initially increases with the number of monomers N. The enhancement levels off around the particle volume fractions $f_v = 0.20$ to $f_v = 0.30$, and then declines when the particle volume fraction reaches $f_v = 0.40$. This decline suggests that the spherical volume starts to behave as a homogenous [91]. Our overall conclusion is that the aggregate's enhanced backscattering occurs even when the individual grains have none. This implies that the enhanced backscattering is a colligative effect related to the aggregate structure.

We now hypothesize a physical interpretation for the enhanced backscattering in the aggregate due to multiple scattering between the monomer grains. Our approach will use dimensional analysis to estimate the extent of multiple scattering within the hematite aggregates.

Inter-grain multiple scattering within the aggregate will depend upon the grain scattering

cross-section, with dimension length squared, and the number density of the grains, with a dimension of inverse length cubed. Thus, a length scale can be formed from these two quantities as the inverse of their product. It is reasonable to claim that this length scale is related to the mean free path (mfp) of the light wave between scattering events [92] but this interpretation is not necessary. Thus, we write

$$mfp = \frac{1}{nC_{sca,mon}} = \frac{4\pi a^3}{3C_{sca,mon}.f_v} \tag{4.2}$$

where, $C_{sca,mon}$ is the total scattering cross-section of a monomer grain, n is the number density of the monomers, f_v is the monomer volume fraction, and a is the monomer radius. This scattering length scale can be compared to the length scale of the entire aggregate to get a dimensionless number that is related to the extent of the multiple scattering, which would be the average number of scattering events <s> given by

$$< s >= \frac{R}{mfp} \tag{4.3}$$

To continue we expect the intra-aggregate scattering to be stochastic and governed by the Poisson distribution. Then the probability of s scattering events within the aggregate is

$$P(s) = \frac{< s >^s}{S!} e^{-<s>} \tag{4.4}$$

Multiple scattering plays a significant role for non-absorptive particles when the average number of scattering events <s> becomes large.

We now test our hypothesis that enhanced backscattering from the aggregate is due to multiple scattering between the monomer grains by seeing if our definition of the average number of scattering events <s> is correlated to the enhanced backscattering.

We have calculated the average number of scattering events <s> for the spherical scattering volume of diameter of 2.4 μm. The enhancement in the backscattering for different volume fractions was quantified by calculating the ratio of scattered intensity at 157°, our

largest experimental angle, to the minimum intensity near 129° i.e., I(157°)/I(Min). This ratio is plotted versus the average number of scattering events <s> and volume fractions, f_v in Fig. 4.9.

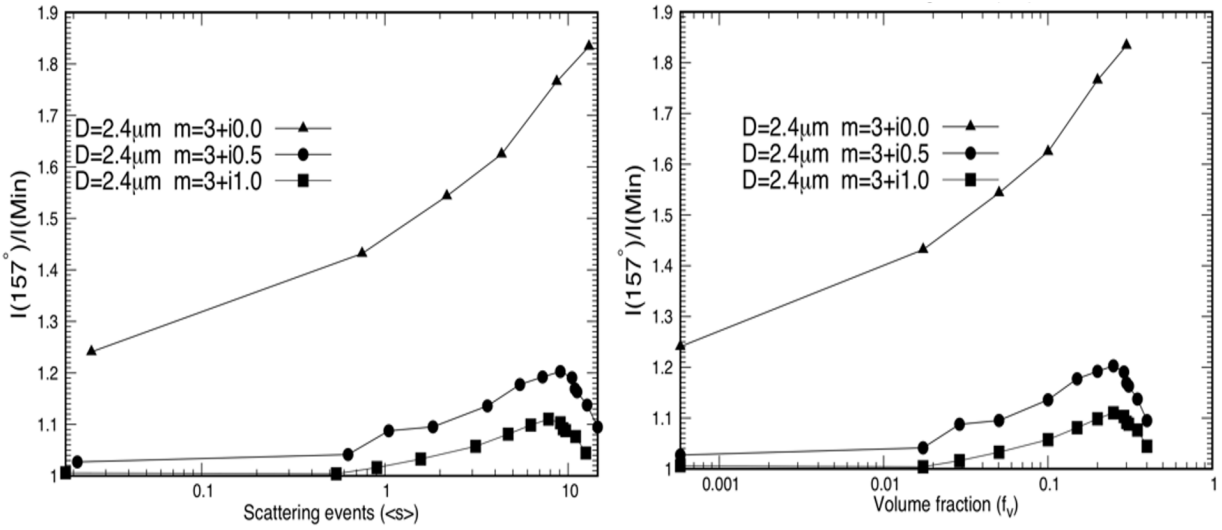

Figure 4.9: *Plot showing the enhancement in the backscattering, the ratio I(157°)/I(Min), versus (left) the average number of scattering events <s> in the aggregate, and (right) the volume fraction f_v of monomers in the aggregate.*

Figure 4.9 (left) shows that when the average number of scattering events in the aggregate is very small, there is very little enhanced backscattering. With increasing scattering events, there is an increase in the backscattering enhancement and this enhancement peaks around <s> $\simeq$ 10. When $\kappa \geq 0.5$, a further increase in the scattering event led the backscattering enhancement to decrease; see Fig. 4.9 (right). The behavior for $m = 3 + i0.0$ shows no peak, but the computation was limited by computational time constraints such that volume fractions where the other two refractive indices showed a peak were not obtained when $\kappa = 0$. The decrease might occur because with an increasing number of monomers, the spherical volume starts to act like a homogenous particle, which we have seen has no enhanced backscattering for the values of R that we are considering. Nevertheless, our tentative multiple scattering hypothesis correlates the increase and the ultimate decrease in

the enhanced backscattering with increasing monomer volume fraction.

4.5 Conclusion

In this chapter, we have studied light scattering due to densely aggregated hematite particles composed of monomer grains. Hematite is a naturally occurring mineral with a large refractive index of $m = 3.0 + i0.5$ at $\lambda = 532$ nm, the wavelength used in our study. Scanning electron micrographs (SEM) indicated that the particles were aggregates whereas the optical microscope pictures showed that the aerosol had a bimodal distribution with effective mean diameters of roughly 1 and 10 µm. This is consistent with the light scattering results, uncovered by Q-space analysis which displayed two Guinier regimes. The two Guinier regimes indicated the bimodal size distribution, consistent with optical microscopic inferred size distribution. Ultra Small-Angle X-ray Scattering (USAXS) indicates that the aggregates were uniform and non-fractal. The aggregates were composed of smaller grains with an approximate size of 200 nm.

Mie calculations for a sphere, equivalent to the aggregate size, were compared to the experimentally observed results. The observed results showed an enhanced backscattering, whereas Mie calculations for a sphere equivalent to the aggregate size were compared to the experimentally observed results. Enhanced backscattering was observed for angles greater than 130°. It was shown with model calculations, that this enhanced backscattering was due to the aggregate structure, despite the large imaginary part of the refractive index which quenched enhanced backscattering for the aggregate monomers and aggregate size equivalent sphere. It was proposed that aggregate internal multiple scattering between monomers within the aggregate was the cause of the enhanced backscattering. Dimensional analysis for the average number of internal scattering events supported that proposition.

Chapter 5

Light Scattering Due to Nearly Spherical and Irregular Shaped Aluminum Abrasive (Al_2O_3) Particles

5.1 Introduction

Light scattering from non-spherical particles can be significantly different from those of volume or surface equivalent spheres, implying that Mie theory may not be suitable for interpreting scattering data such as satellite observed data. Theoretically, light scattering by small arbitrarily shaped particles can be calculated by the discrete dipole approximation method [93–95]. Another widely used method for computing the scattering by non-spherical particles is the T-matrix approach [96–99]. However, these techniques become very time-consuming to calculate the scattering from large-sized particles (i.e., particles much larger than the wavelength). These techniques were specifically developed to calculate light scattering by rotationally symmetric non-spherical particles like spheroidal [100], finite circular cylinders [101], Chebyshev particles [102, 103], ice crystals [104], Gaussian random particles [105].

Mishchenko et al. [1997] compared the scattering from non-spherical versus projected-area-equivalence spherical particles and found a large difference in compared results at the side and backscattering regime [63]. Hill et al. [1984] demonstrated that the scattering phase function of natural soil particles could be represented by a size/shape mixture of randomly oriented spheroids much better than projected-area-equivalent spheres [106]. Besides these above mentioned methods of characterizing the aerosol particles, Digital holography is another very useful method to specify the particle size, shape and orientation free of assumptions [107–110].

In this work, we scattered the light from irregular particles and compared the result to the Mie scattering calculated for volume equivalent particle number size distribution measured by an aerosol sampling instrument, Aerodynamic Particle Sizer, APS 3321. We reported the measurement of scattered intensity for nearly regular and irregularly shaped Al_2O_3 abrasive powders of various grit sizes. Those particles were created by rolling between the grinding surfaces, yielding a roughly spherical shape, unlike particles with large aspect ratios, e.g., flakes and needles [19]. Thus, we can anticipate that the particles will act like spherical particles to some extent too. The measurements were performed at a wavelength of 532 nm, covering the scattering angle range from 0.32° (extreme forward scattering) to 177.6° (backscattering). The measured scattering intensity data were analyzed by both θ and Q-space methods. Furthermore, extreme-forward scattering data is important in the light scattering because 50% of the scattered light (approximately) falls within the Guinier regime in the forward scattering lobe such that $\theta \leq \lambda/\pi D$, where λ is the wavelength of light and D is the particle diameter [40]. And backscattering data works as a foundation for interpreting remote sensing and identifying aerosols. APS provides the *in-situ* real-time measurements of the aerosol particle number size distribution that the laser could see during the light scattering measurements. The light scattering results were compared to the Mie results calculated for APS observed number size distributions.

The number size distributions were measured using an Aerodynamic Particle Sizer (APS

3321). To analyze its sizing accuracy, we used two different sizes of NIST traceable monodisperse polystyrene latex (PSL) spherical particles. The conversion principle for APS measured aerodynamic particle sizer to volume equivalent diameter used in Mie calculations was found in [37, 60]. We applied Guinier analysis to determine the scattering inferred size of the particles, and the results were compared to the intensity weighted APS observed number size distribution. The APS observed mean number size distribution was compared with the manufacturer's reported size.

5.2 Results

The manufacturer reported most probable sizes (D = 2R) of the grits are labeled in the pictures, Fig. 5.1. We used an optical microscope to have more insight into particle shapes and sizes. Optical pictures are shown in Fig. 5.1. The figures indicated that the particles are irregular but not extremely like flakes in shape.

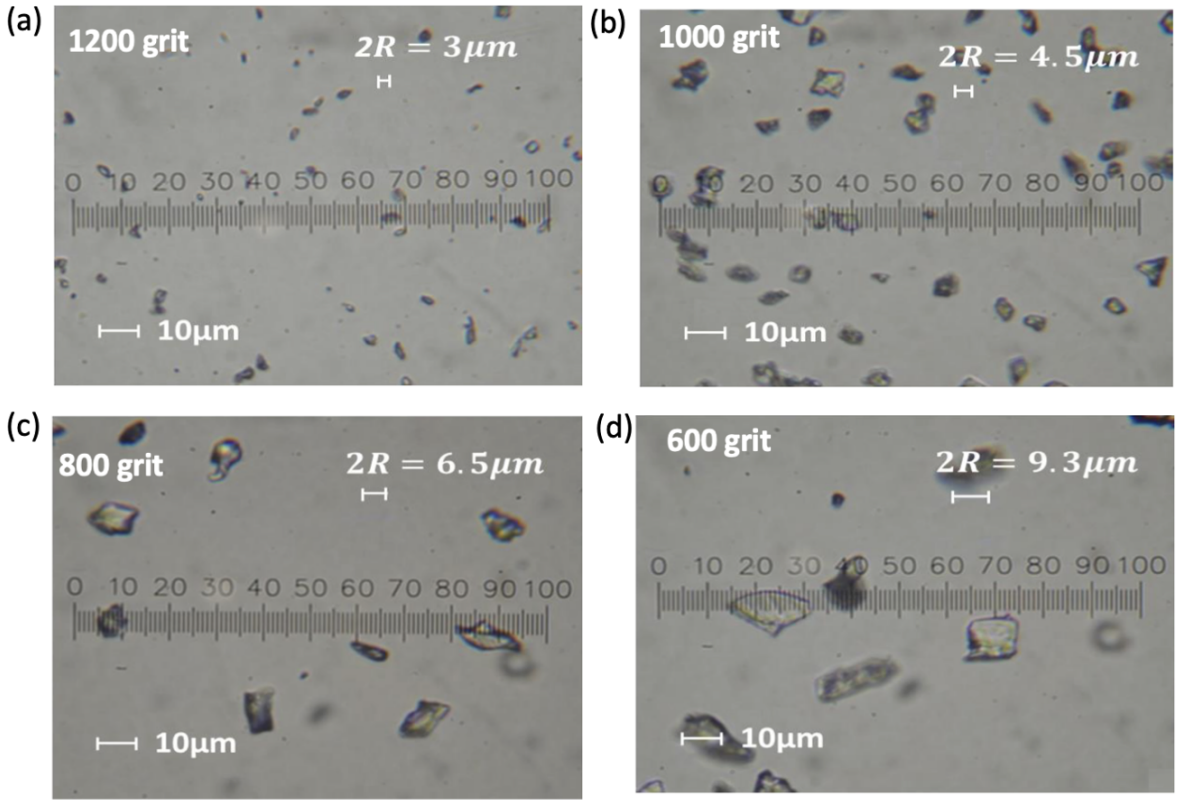

Figure 5.1: *Optical microscope images for aluminum abrasive (Al_2O_3) powders (a) 1200 grit, (b) 1000 grit, (c) 800 grit and (d) 600 grit. Pictures were taken from [19].*

The size distributions of aerosolized aluminum abrasive powders were measured by the APS. The particles were collected at the light scattering volume. The APS measures the same particle size distributions that the laser could see. The volume equivalent sphere diameter is required for the Mie calculation. Therefore, the formula that is used to convert the APS measured aerodynamic diameters to the volume equivalent diameters can be found in [37, 46]. The Al_2O_3 abrasive particles look moderately spherical, unlike Illite particles with a shape factor (χ) = 1.3 [65]. With this value of χ (square root dependence) in the conversion formula, the magnitude of D_v got changed by 14%. In comparing Illite particles' shape with Al_2O_3 abrasive particles (Fig. 5.1), χ is near unity for Al_2O_3 particles. Thus,

for our calculations, uncertainties in the value of χ could cause a small or no change that was acceptable within the limit of experimental error. The density used for Al_2O_3 was 2.93 g/cc [111].

Since the Guinier regime lies in the forward scattering regime, the scattering intensity is proportional to the diameter to the fourth power, i.e., D^4 [14, 15]. To account for this, the APS converted volume equivalent size distribution is multiplied by D^4. Figure 5.2 shows the volume equivalent number size distributions and transformed intensity weighted distributions for four different grits 1200,1000, 800, and 600. We normalized both the number size distributions and corresponding intensity weighted distributions to have a peak value of unity. The intensity-weighted distribution curves show that although most of the particles lie in the smaller size range, the contribution of those particles is negligible compared to the large particle's contribution. APS measured size distributions showed that the most probable diameters for 1200, 1000, 800, and 600 grits were 2.7, 6, 7.8, and 10 microns, respectively. The intensity-weighted distributions for 1200, 1000, 800, and 600 grits showed peaks of 4.4, 7.3, 13.0, and 16.0 microns, respectively.

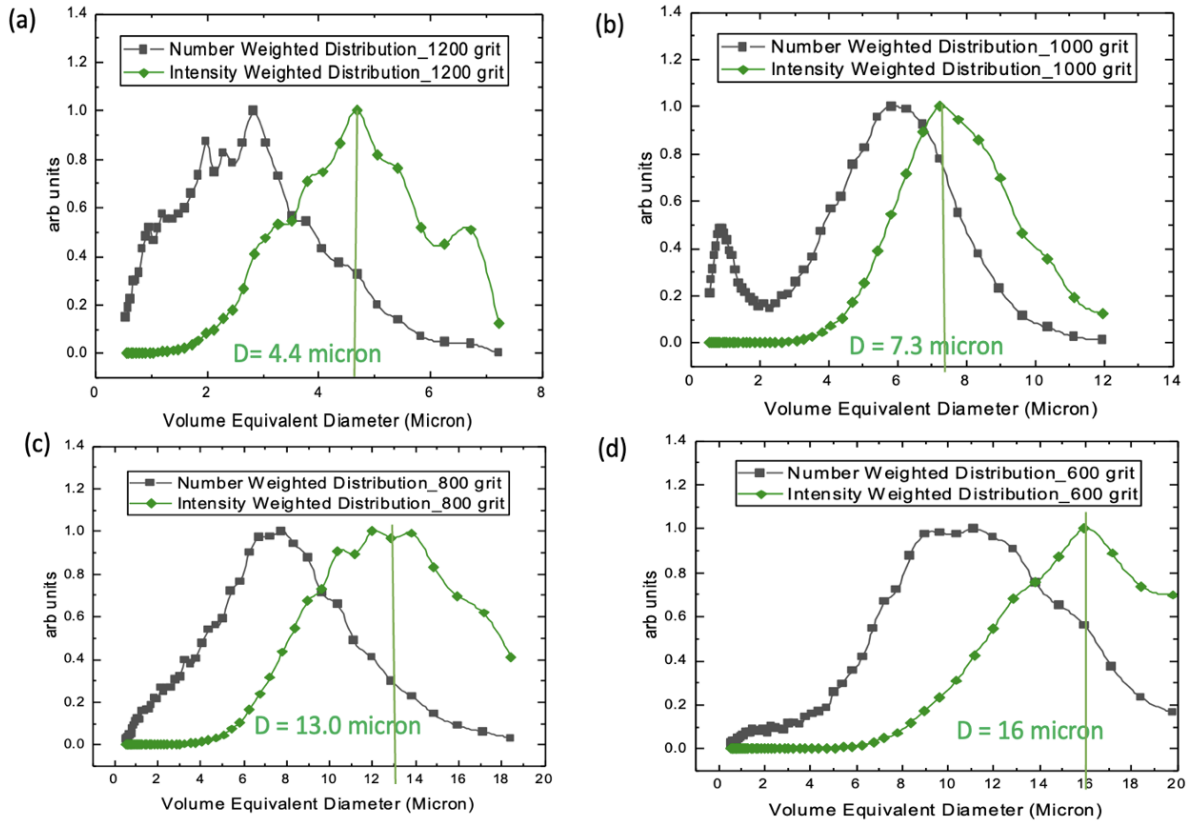

Figure 5.2: *Particle number distribution for aluminum abrasive (Al_2O_3) powders of various grit sizes (a) 1200, (b) 1000, (c) 800, and (d) 600, measured with the APS 3321 after converting aerodynamic diameter Da to the volume equivalent diameter Dv and their transformation to an intensity weighted distribution with a weighing factor of D^4. Guinier inferred diameters are labeled in each graph.*

5.2.1 Comparison of Light Scattering Measured Data with Mie Calculations for Different Aluminum Abrasive (Al_2O_3) grit sizes.

Since the measured data ranged from an extreme forward scattering to the backscattering regime, we analyzed the data by plotting both versus the magnitude of scattering wave

vector, q on a log-log scale, called Q-space, and versus scattering angle, θ linearly. Figures 5.3 and 5.4 showed the comparisons between experimentally measured light scattering results with Mie calculations. The data were normalized to unity at the smallest forward scattering angle of 0.32°. Mie calculations were carried out for volume equivalent number size distributions obtained from APS observed number size distributions. For all the grit sizes, the Q-space plot showed a constant forward scattering lobe at the smallest q, followed by a Guinier regime near q $\approx R^{-1}$. After the Guinier regime, a power law regime appeared that ended with an enhancement in the backscattering.

For all the grit sizes, Mie calculations matched well with the experimental results at the forward scattering regime. However, it underestimated experimental light scattering results at the side scattering and overestimated at the backscattering regime. The smooth and featureless scattering that appeared at the side scattering regime seems to be commonly found for irregularly shaped particles [62, 106, 112–116]. This smooth scattering can be explained by particle ensembles being a mixture of different shapes in which shape-specific scattering functions of individual particles are averaged out [117–120]. Mishchenko et al., 1997 studied the light scattering by shape distributions of polydisperse, randomly oriented spheroids with refractive indices and size distributions representative of naturally occurring dust aerosols using the T-matrix method [63]. They found similar light scattering patterns (Figs. 5.3 and 5.4) when the scattering function averaged over a wide aspect-ratio distribution of prolate and oblate spheroidal grains. However, they observed a unique, shape-specific scattering function for a single spheroidal shape.

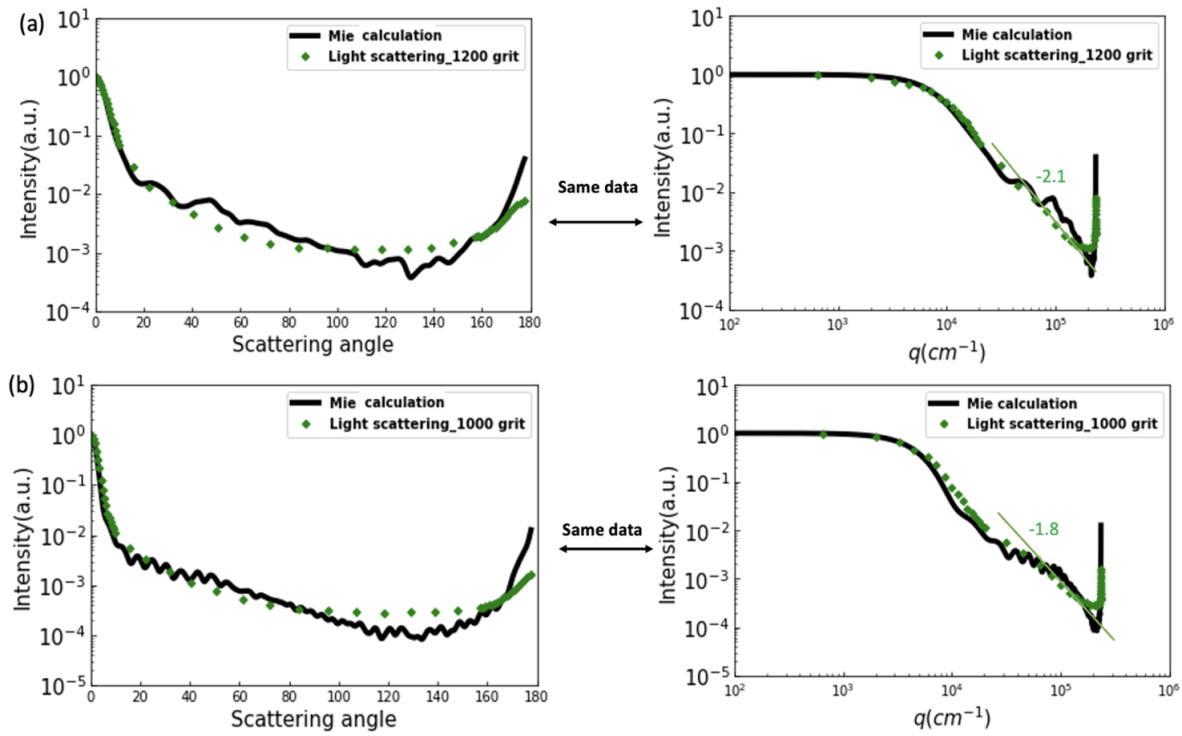

Figure 5.3: *Comparison of the experimentally measured forward normalized light scattering data with Mie calculations for APS observed aluminum abrasive (Al_2O_3) particles. Same data were plotted both linearly versus scattering angle, θ and logarithmically versus q, the method of Q-space analysis for (a)1200 grit and (b) 1000 grit.*

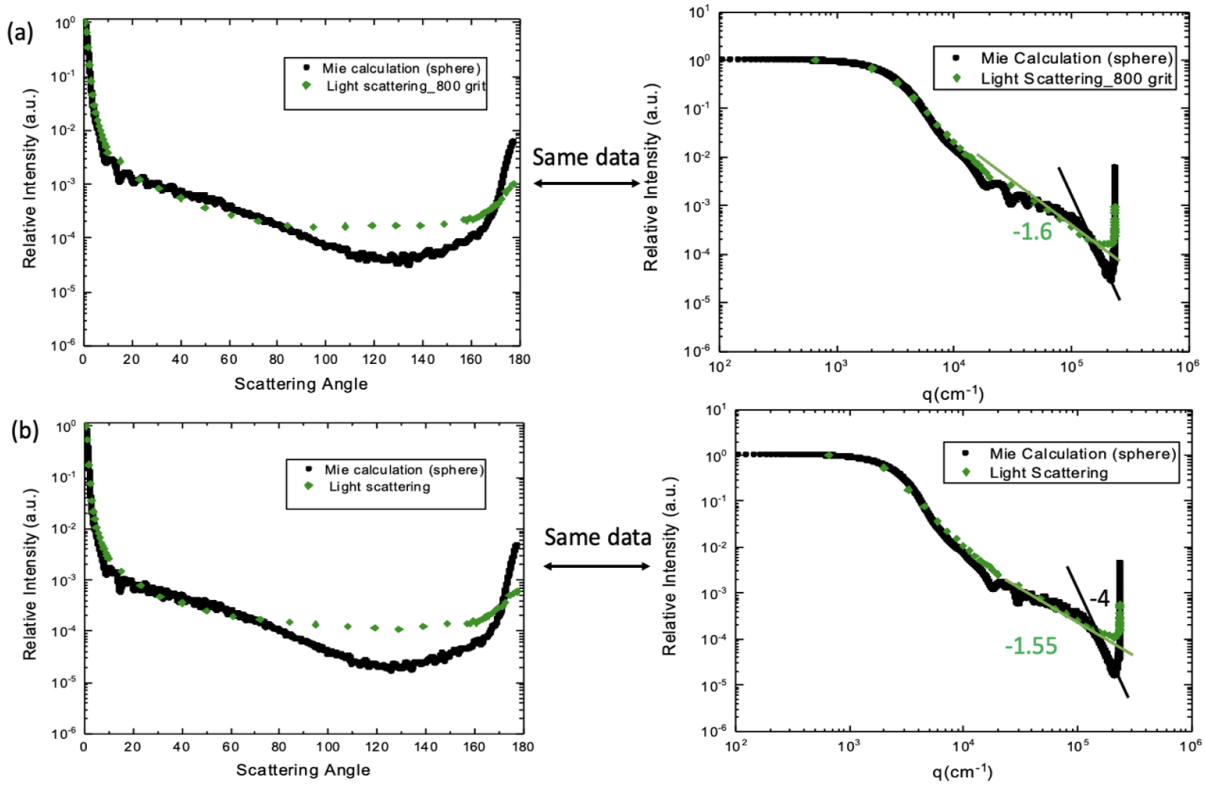

Figure 5.4: *Same as figure 5.3 for 800 and 600 grits.*

5.2.2 Guinier Analysis on Light Scattering Results for Different Irregular Aluminum Abrasive (Al_2O_3) Grit Sizes

From the Q-space plot, one can determine the size of any arbitrarily shaped particle by doing a Guinier analysis, under the assumption of weak refractivity. For a sphere, the radius of gyration R_g is given by

$$I(q) = I(0)(1 - \frac{q^2 R_g^2}{3}), \rho' \to 0 \tag{5.1}$$

where I(q) is the scattering intensity, I (0) is the forward scattering intensity and, q is the magnitude of the scattering wave vector. In principle, Guinier analysis is applicable when $qR_g < 1$, but one can exceed this limit with minor error [22]. For the small qR_g, the Eq.

5.1 can be written as

$$\frac{I(0)}{I(q)} = 1 + \frac{q^2 R_g^2}{3} \tag{5.2}$$

The size determined from the Guinier analysis is accurate only in the diffraction limit when the internal coupling parameter is $\rho' < 1$, for weakly refractive particles. For $\rho' > 1$, the Guinier equation still holds, but, the radius of gyration given by Eq. 5.2 is not the true radius of gyration. For a sphere with $\rho' >> 1$, the ratio of the true to measured radius of gyration is 0.88 ($\pm$ 12 %). Although Guinier analysis is applicable for spherical particles, we still apply for these irregular aluminum abrasive particles to get Guinier inferred sizes.

We performed the Guinier analysis for experimentally measured light scattering results by plotting inverse normalized intensity, $I(0)/I(q)$ versus q^2, as shown in Fig. 5.5. Equation 5.2 indicates that the Guinier plot should be a straight line with a slope of $R_g^2/3$. For the 1200 and 1000 grits, there are several data points for Guinier analysis that satisfied the condition $qR_g < 1$, unlike 800 and 600 grits with limited data points and poorly defined Guinier inferred sizes. According to the fit lines' slopes, the Guinier inferred radii for 1200, 1000, 800, and 600 grits were 2.14, 3.6, 6.56, and 8.30 microns, respectively. For such a large particle with $\rho' >> 1$, $R_{g,G}$, is greater than R_g by around 12%. After applying the correction factor of 0.88, the true Guinier inferred radii of gyration were calculated to be 1.88, 3.16, 5.77, and 7.30 microns, respectively. The shape of the particles was irregular, but we made an approximation based on a sphere such that $R_g = \sqrt{3/5}R$. Thus, the equivalent sphere radii for 1200, 1000, 800, and 600 grit were found to be 2.42, 4.07, 7.44, and 9.42 microns and corresponding diameters 4.84, 8.14, 14.88, and 18 microns respectively. These diameters were consistent with the intensity weighted distribution peaks are shown in Fig. 5.2. The peaks correspond around the diameters 4.40, 7.3, 13, and 16 microns for 1200, 1000, 800, and 600 grits, respectively.

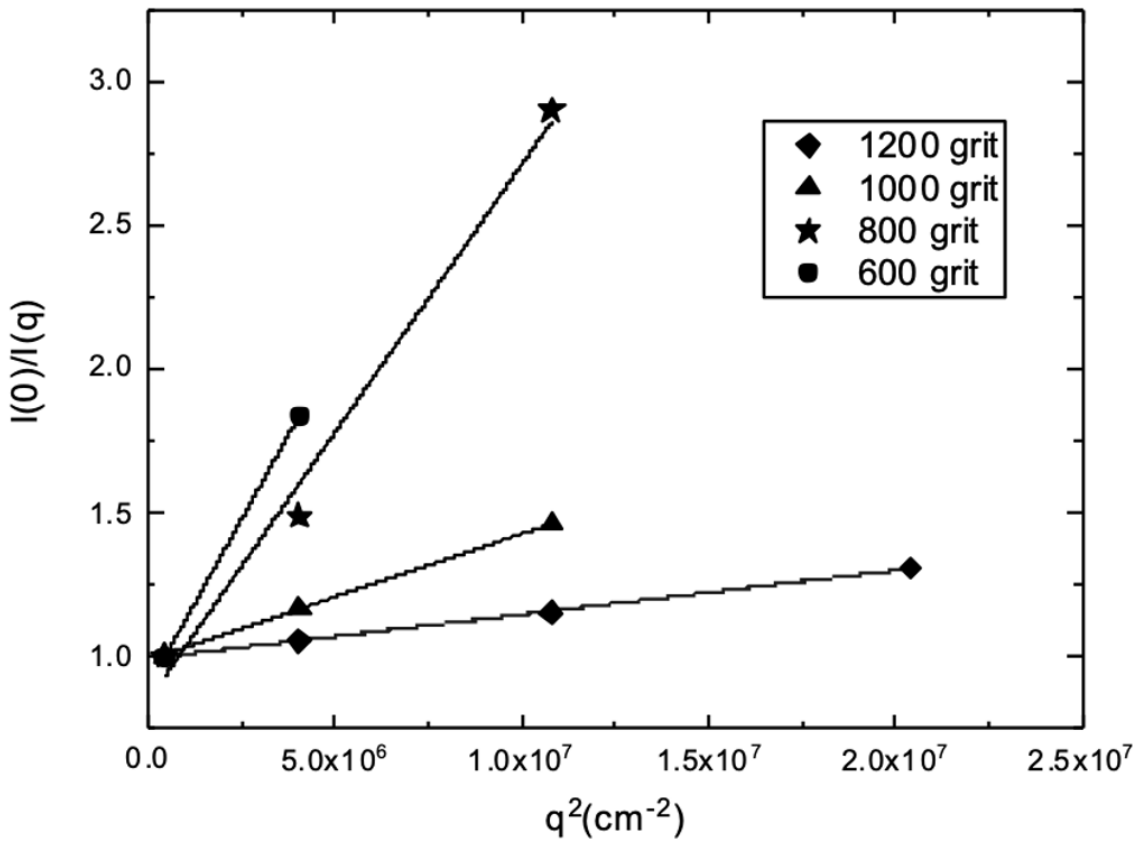

Figure 5.5: *Guinier analysis on aluminum abrasive (Al_2O_3) particles of 1200, 1000, 800, and 600 grits.*

5.2.3 Light Scattering Results of Nearly Spherical Al_2O_3 Particles

We carried out light scattering experiments for the nearly spherical Al_2O_3 particles of two-size distributions. The TEM pictures for such particles are shown in Fig. 5.6 to gain more insight into particle shape and size distributions. TEM pictures indicate a size distribution consistent with the APS measured number size distribution. In addition, the TEM images showed particles were nearly spherical.

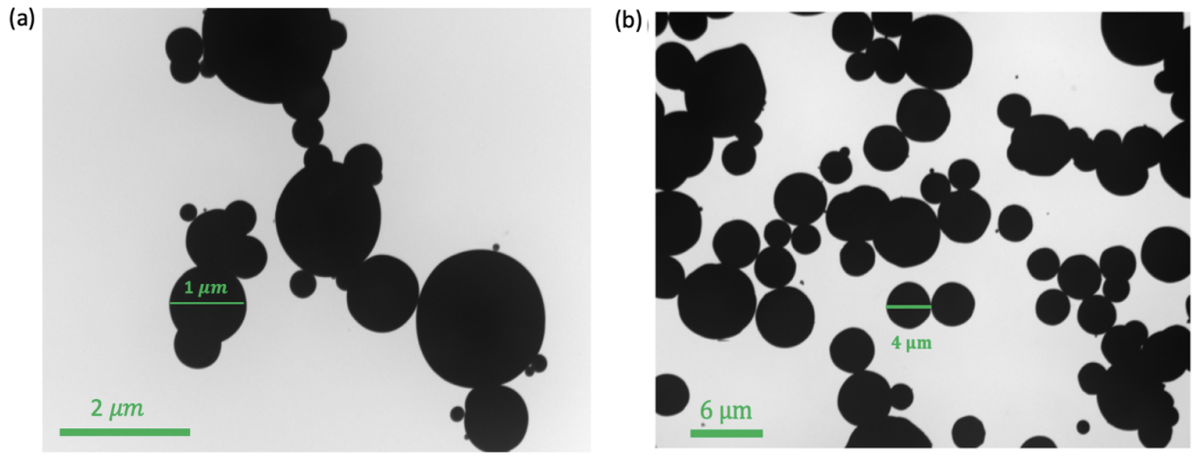

Figure 5.6: *TEM images of aluminum abrasive (Al_2O_3) particles (a) small, S and (b) large, L samples.*

The volume equivalent number size distributions of Al_2O_3 particles are shown in Fig. 5.7, and were measured by the APS 3321. Figure 5.7(a) shows that the number size distributions peak at 1.07 and 4.22 microns, inferring the most probable diameter for small, S, and large L samples. This most probable diameter agreed with the manufacturer's reported most probable sizes of 0.8 and 5 microns, respectively. These number size distributions were consistent with images shown in Fig. 5.6. Since the Guinier regime lies in the forward scattering regime, the scattering intensity is proportional to the diameter of the fourth power, i.e., D^4 [14, 15]. Thus, intensity weighted number size distributions (i.e., light scattering weighted size distribution) were obtained with a weighting factor of D^4. Figure 5.7(b) showed that the intensity weighted number size distributions peak around the diameter of 3.4 and 8.5 microns for S and L samples, respectively.

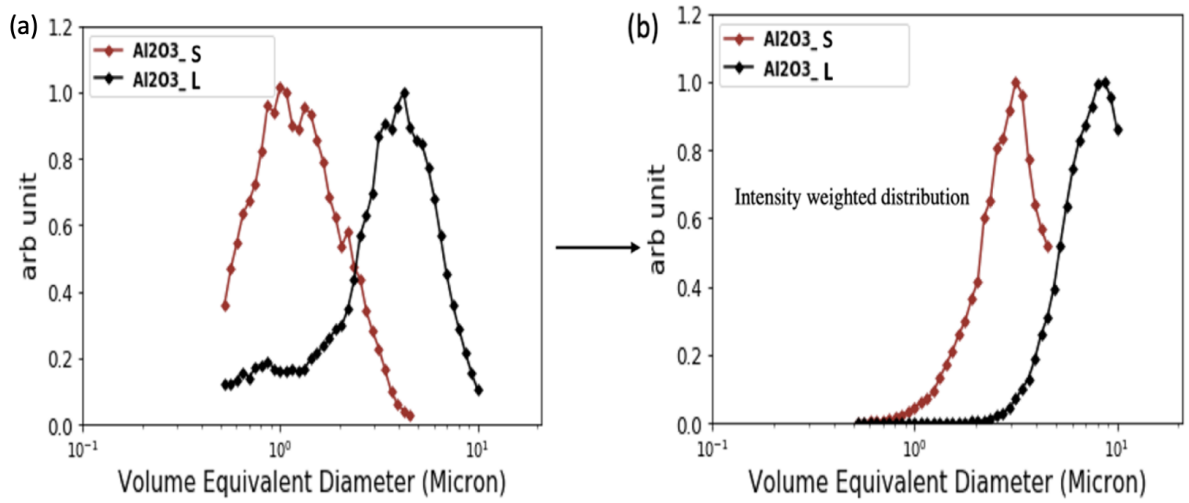

Figure 5.7: *(a) The volume equivalent particle number distributions, (b) Intensity weighted distributions for Al_2O_3 samples. We normalized both the number size distributions and corresponding intensity weighted distributions to have a peak value of unity.*

We performed the Guinier analysis for experimentally measured light scattering results by plotting inverse normalized intensity $(I(0)/I(q))$ versus q^2 [Fig. 5.8]. According to the fit lines' slopes, the Guinier inferred radii were calculated to be 1.24 and 3.15 microns for the S and L samples, respectively. Although particle's shapes were nearly spherical, we still made an approximation based on a sphere such that $R_g = \sqrt{3/5}R$. By multiplying R_g by $\sqrt{5/3}$, three-dimensional object equivalent radii for S and L samples becomes 1.59 and 4.06 microns. Thus, the light scattering determined diameters for S and L samples were D = 3.18 and 8.12 microns. These Guinier inferred sizes were consistent with the intensity weighted distribution (Fig. 5.7(b)).

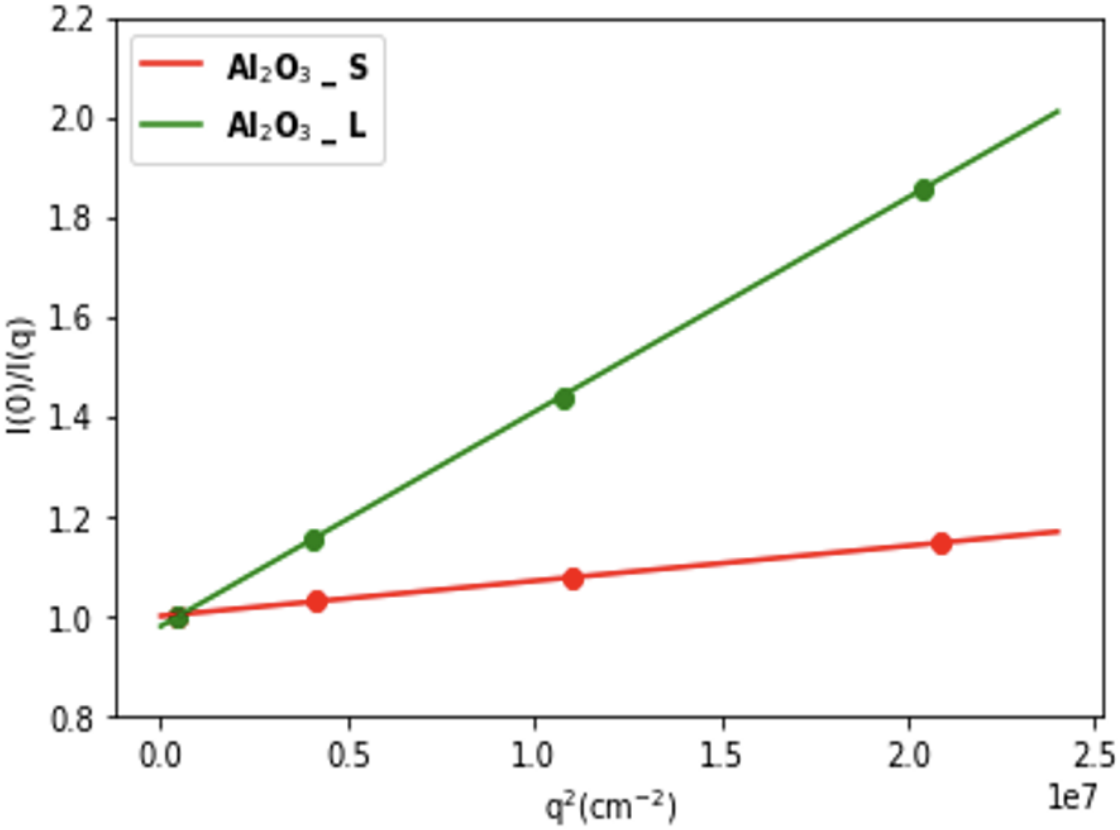

Figure 5.8: *Guinier analysis of nearly spherical aluminum abrasive* (Al_2O_3) *particles.*

Figure 5.9 shows a comparison between Mie calculations and experimental results, plotted in Q- space and conventional θ-space. The Q-space plots showed a forward scattering lobe, a Guinier regime, followed by a well-defined power-law regime that ends with an enhancement in the backscattering. The Mie calculation and the data agreed closely in the small-angle range i.e., at the forward scattering regime, but there was a small difference at the side scattering and a quite large difference at the backscattering regime. Here, the compared results for the nearly spherical data fit better with the Mie calculations than the one for irregular particles presented in Figs. 5.3 and 5.4.

On comparing the results of scattering from nearly regular (Fig. 5.9(b)) to irregular particles of equivalent size (Fig. 5.3(b)), we observed a close agreement between Mie calcu-

lations and measured data at the forward scattering regime in both cases. A close agreement between Mie calculations and the measured data at the forward scattering regime may be due to the least sensitivity to the particle's non-sphericity and its optical constants. In the side scattering regime, nearly spherical particles showed a more considerable dip, unlike flat and smooth scattering seen for irregular particles. The difference observed in our compared results for the side and backscattering regimes may be due to irregularity in particle shape. An enhancement in the backscattering is small for irregular particles compared to that of spherical particles. However, we could not quantify how much it decreases with irregularity and sizes. More work is required theoretically and more experimental data from particles of diverse sizes, shapes, and refractive indexes to get conclusive and well-quantified explainable results.

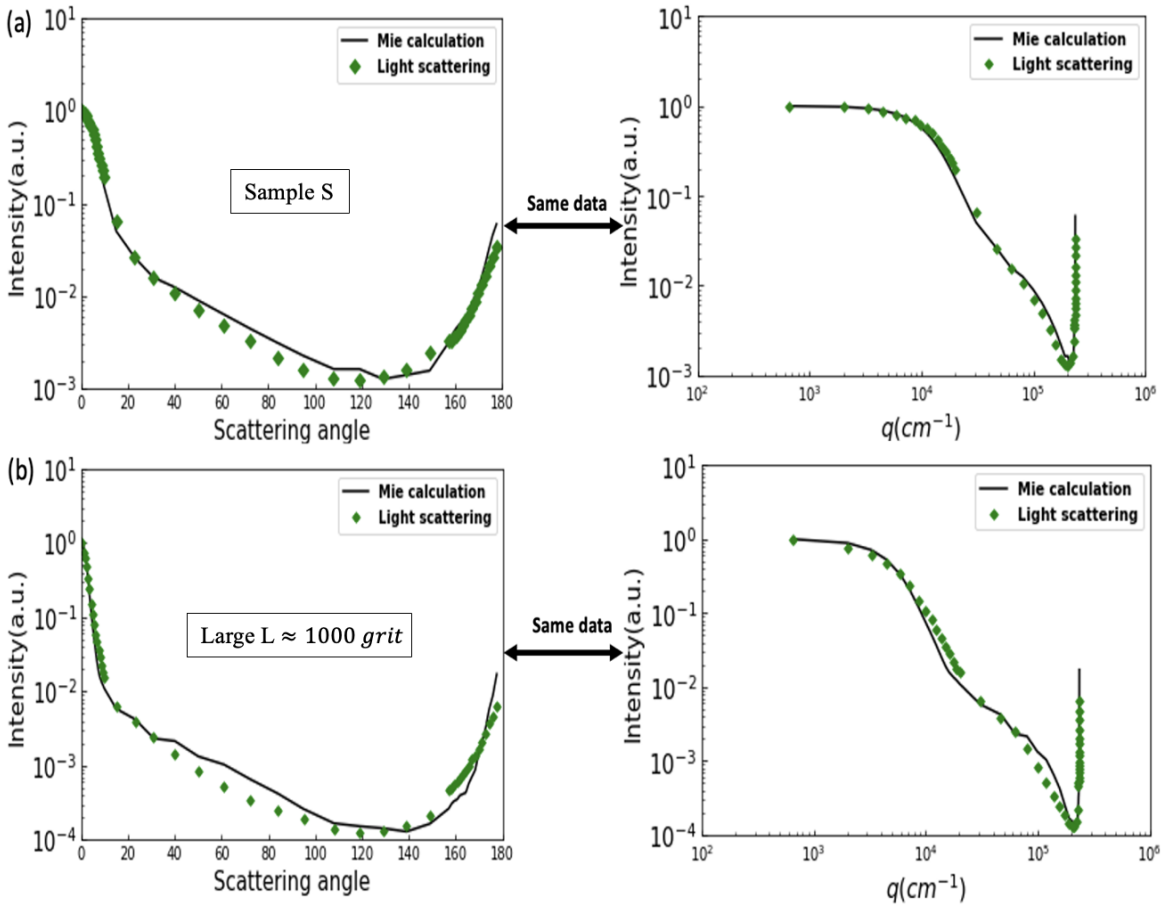

Figure 5.9: *Comparison of the experimentally measured forward normalized light scattering data with Mie calculations for APS observed nearly spherical aluminum abrasive* (Al_2O_3) *particles. Same data were plotted both linearly versus scattering angle,* θ *and logarithmically versus q, the method of Q-space analysis for (a) Small, S and (b) Large, L samples. The Q-space plot shows a forward scattering lobe, a Guinier regime, and the subsequent power law regime that ends with an enhanced backscattering. The conventional plot portrays the trend of the data in the larger scattering angle range more clearly.*

5.3 Conclusion

For the forward scattering regime, the Mie theory is expected to be reliable and accurate in interpreting the measured results for both spherical and non-spherical particles. However, Mie's theory is unreliable in the side and backscattering regime, where it estimates the scattering significantly different than what we observed experimentally for irregular particles. For near forward scattering angles, scattering is independent of particle shape, and optical constants. So, the theoretical Mie curve accurately explains spherical and non-spherical light scattering data at the forward scattering regime. However, for non-spherical particles, Mie theory predicts differently at larger scattering angles.

At the side and backscattering regime, the measured data and Mie results agreed qualitatively for nearly spherical particles. For irregular particles, Mie results underestimate the scattering at the side scattering regime and over-estimate at the backscattering regime. Our results showed that the difference between the Mie results and measured data is relatively small for nearly spherical particles than for the irregular particles. The difference seems to increase with increasing the size of the particles but needs more theoretical and experimental results to quantify such differences. A flat and smooth scattering pattern appeared at the side scattering regime for irregular particles that did not appear for nearly spherical particles, consistent with the result calculated for spheroidal-shaped particles for different aspect ratio [63].

The intensity weighted distribution curves show that although most of the particles lie in the smaller size range, the contribution of those particles is negligible compared to the large particle's contribution. Thus, the most significant point is the heavy weighting of light scattering in favor of large size particles in a distribution. The measured particle number size distributions show that larger particles in distribution are only a small fraction, leading to significant uncertainty in the measurements. Thus, intensity weighting is of utmost importance when comparing light scattering measurements to the measurements made by other aerosol measuring instruments like APS, and other sampling devices like SMPS, etc.

Chapter 6

Light Scattering from Post-flame, Non-homogenous Soot Particles

6.1 Introduction

The Intergovernmental Panel on Climate Change (IPPC 1996) and combustion researchers used the term "soot" as a light-absorbing, combustion-generated aerosol. However, climate modelers mostly called it "black carbon", which has strong absorption across a broad spectrum of visible wavelengths [121]. These soot particles have a direct effect on climate radiation budgets, human health, and other air quality-related areas [122–125]. Thus, the study of light scattering due to soot particles is essential in understanding its effect on global radiation budgets/climate models. Soot particles are carbonaceous black particles with fractal morphology produced during the incomplete combustion of fossil fuels and biomass [126, 127]. Fractals have repeating branching leading to the scale invariance structure, e.g., trees or river deltas. If you break off a tree branch and make it stand on the earth, this part looks like the whole tree, making it scale-invariant. The Intergovernmental Panel on Climate Change (IPCC) Forth Assessment Report has shown that the effects of soot particles on global radiation budgets are being poorly understood. Climate

modelers have used the Lorentz-Mie theory to estimate their optical properties by assuming the particles are spherical. However, soot particles are non-spherical aggregates with open structures, which cannot be approximated as spheres. Due to such shape and structure of soot particles, we proposed that intra-dependent scattering between the monomers within the aggregates and inter-dependent scattering between the aggregates needs to be accounted for.

Soot typically occurs in an aggregated form that consists of many small, nearly spherical primary particles, called monomers, forming a complex structure (aggregate). Soot monomers have a high refractive index value, both real and imaginary. Hence, soot aggregates play a crucial role in the global radiation budget by scattering and absorbing light. Soot agglomerates are fractal-shaped, and their structure obeys a power law [20, 128],

$$N = k_0(R_g/a)^{D_f} \tag{6.1}$$

In Eq. 6.1, N is the number of monomers in the aggregate, k_0 is the scaling pre-factor, which indicates the shape and compactness of the aggregate, R_g is the radius of gyration of the aggregate (overall size), a is the monomer radius of the order of 10−30 nm [129], 20−50 nm [130] and D_f is the mass fractal dimension used to describe the aggregate morphology quantitatively. Its value can vary from 1 to $\simeq 3$; 1 for an infinitely long straight chain of aggregate and $\simeq 3$ for a compact agglomerate. Soot typically forms by a diffusion-limited cluster-cluster aggregation (DLCA) process, leading to fractal aggregates with $k_0 = 1.35 \pm 0.05$ and $D_f = 1.78 \pm 0.05$ [20]. This Eq. 6.1 is very useful in describing the morphology of fractal aggregates but not the shape. In our study, the scattered intensity is plotted versus the magnitude of the scattering wave vector, q, called Q-space analysis. The importance of this analysis over the θ-space is that it leads us to quantify the result like aggregate size R_g, and fractal dimension D_f.

For laboratory studies, soot is frequently produced by burning hydrocarbons. Experimental laboratory studies of scattering light by soot have been mostly limited to fresh soot

in simple flames. However, much theoretical work has considered more complex situations [131–133]. A great deal of work on light scattering due to soot particles have been carried out in our lab previously [19, 20, 41–43, 50, 129, 134–140]. This work was limited to measuring the scattered light at the forward scattering regime, except for Heinson et al., 2015 who studied angles up to 157°. This study aims to systematically study light scattering by soot generated using a commercially available miniature inverted soot generator and premixed burner. The measurements were made at a wavelength of 532 nm with vertically polarized incident light in the scattering angle range from 0.32° to 157°. For the soot generated by a miniature soot generator, the scattering volume was in a post-flame region where the soot was nearly at room temperature; whereas the scattering volume was very near to the flame for the pre-mixed burner. As indicated by Eq. 6.1, many parameters are associated with the soot particles making it difficult to characterize accurately. The microscopic study can be done for this purpose; however, we contend that light scattering is superior to characterizing soot particles because it is an *in-situ* method. First, we used a commercially available aerodynamic particle sizer spectrometer (APS 3321 (TSI)) to determine the number size distribution of soot from which we scattered light. Then, we analyzed soot particles using a transmission electron microscope (TEM) for more characterization of their size distribution and morphology.

In this work, the light used was a green laser with a wavelength of 532 nm, and the refractive index for this wavelength is $m = n + i\kappa = 1.6 + i0.6$, with some uncertainty, indicating highly absorbent particle [20]. In order to compare the experimentally measured light scattering properties of the soot particles with theoretical calculations, one needs to determine precisely the parameters involved in the Eq. 6.1 and most importantly the refractive index of the soot. There is a large uncertainty in measuring the values of the refractive index of soot due to their changing morphology with time once they formed, composition and the source of generation [141–143]. However, all the works showed that the black carbon particle has a high values of imaginary part of the refractive index. A large imaginary refractive index

typically quenches enhanced backscattering; however, our experimental results showed an enhancement in the backscattering. Furthermore, we found some correlation between the backscattering and the degree of water vapor condensation during combustion. The amount of water vapor condensation is explained by the dew point temperature. Though quantitative relations are not established for the degree of an enhancement in the backscattering with dew point temperature, some conclusions could be proposed from this study. Figure 6.1 shows simulated soot along TEM pictures of experimentally observed soot.

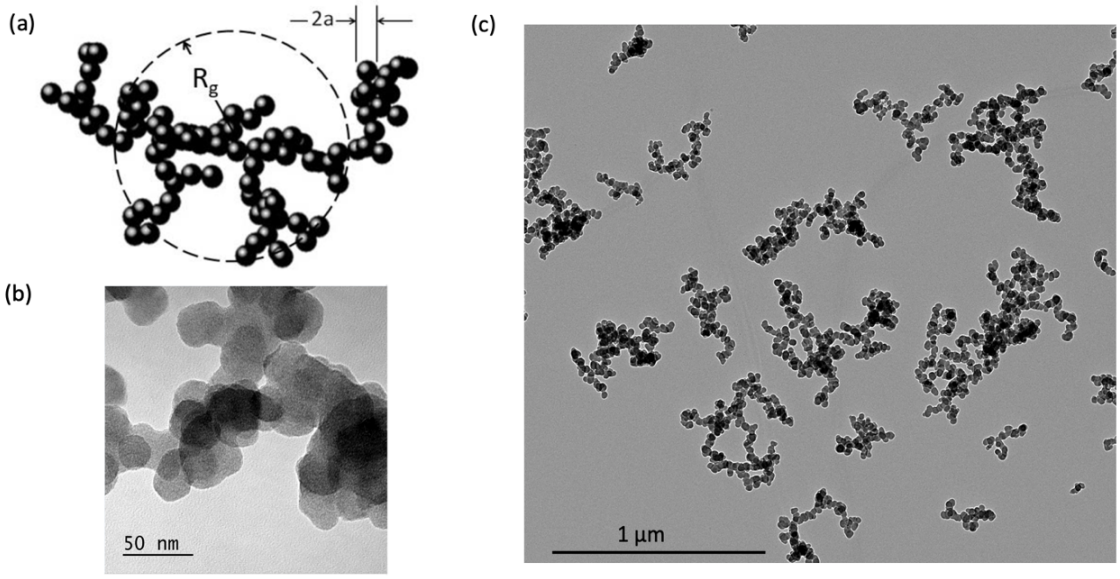

Figure 6.1: *(a) Computer-generated diffusion-limited cluster aggregation (DLCA) fractal aggregate of a radius of gyration R_g, monomer diameter $2a$ and fractal dimension 1.8. (b) and (c) TEM pictures of nascent soot generated at our lab at high magnification showing the monomer size and low magnification showing the aggregated nature of soot particles, respectively.*

6.2 Soot Generation

We generated soot by two different methods: one using a lab-made premixed burner and another using a commercially available miniature inverted soot generator.

A schematic diagram and picture of the pre-mixed burner are shown in figure 6.2. The main body parts' names are labeled. The main body of the burner was made of 6mm copper tubing and two Tee fittings forming two "T" joints. The main body of the burner was covered by a cylindrical shield which was a 7.5 cm long, 1.8 cm inner diameter, and 2.5 cm outer diameter cylinder with a copper tubing at the center. Additionally, the extra cap was built for the burner to wear. The cap was 7.5 cm long and its inner diameter was slightly larger than 2.5 cm such that it could slide along the burner shield. The cap has six opening slots distributed symmetrically along the wall. In one of six slots, one can insert a matchstick to light the burner. A tubing of 5 cm long and 3 mm inner diameter was attached to the top of the cap, which acted as a neck through which soot came out to the scattering volume. The two cylinders worked together as a complete shield to block the outside airflow from reaching the flame. In between the cap and the neck, a 0.6 mm thick solid plate acted as a cooling plate that stabilized the soot stream. The soot stream became more stabilized while passing through the neck. With the help of a suction nozzle with a tip diameter equivalent to the internal diameter of the neck, as indicated in Fig. 6.2(b), the soot steam was confined, helping to produce the soot from a flame stable enough to measure the scattered light.

The two-hydrocarbons ethylene (C_2H_4) and propane (C_3H_8) ran through two separate copper tubing, and were mixed at the T-joints. Now, mixed hydrocarbon runs through the tubing, which joins another copper tubing which oxygen (O_2) runs through, by a second Tee fitting forming another "T" joint. Then, C_2H_4, C_3H_8, and O_2 were mixed from the second Tee fitting and connected to another copper tubing. At the end of this copper tubing, a coupling was used to mount a frit: a porous stone. This frit ensured that the flame was one dimensional along the vertical axis. Finally, the amount of gases used to generate the soot

particles were controlled using a flow meter (Matheson) and a flow controller (Omega).

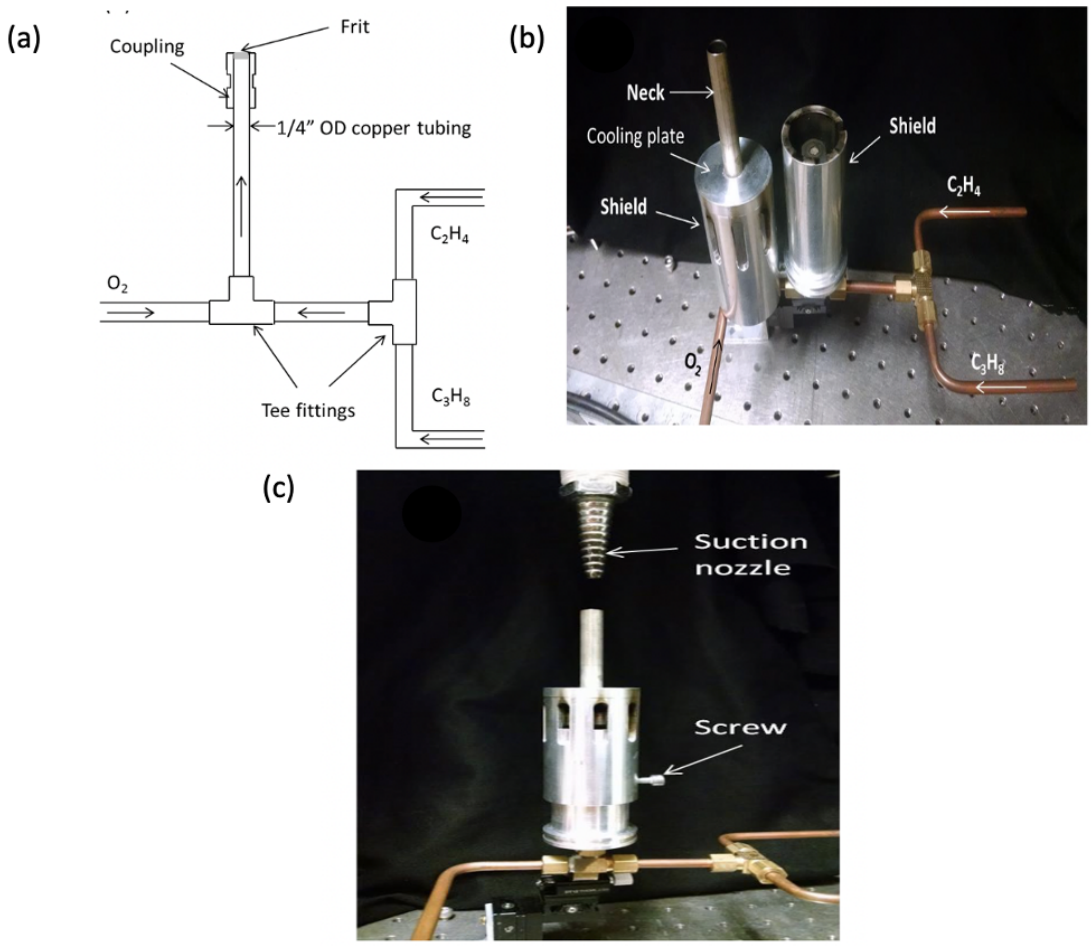

Figure 6.2: *(a) A schematic drawing of the main burner body, (b) two disassembled burner parts with major elements labeled, and (c) a picture of the pre-mixed burner with a suction nozzle connected to a vacuum cleaner [144].*

Using a Mini-inverted soot generator (MISG) from Argonaut scientific, non-homogenous cooled soot particles were generated. It uses an inverted co-flow diffusion flame similar to Stepe [145]. It can generate soot in a wide range of sizes and concentrations. The importance of using such a generator lies in its flame stability and reproducibility. Its design and operation can be found in [146]. The soot generator was operated with ethylene as fuel

and air as an oxidizer. The airflow rate was maintained at 10 SLPM and the ethylene flow ranged from 0.096−0.33 SLPM to give equivalence ratios over a range of $\phi = 0.13$ (air/fuel = 104) to $\phi = 0.48$ (air/fuel = 30). Gaseous flow rates were controlled by using omega mass flow controllers. The generated soot is allowed to split into two parts. First, of the total flow, a certain fraction of soot is sampled by a calibrated aerodynamic particle sizer (APS 3321), and the other is allowed to pass into the scattering volume. The scattering volume was a cylinder with a diameter of 0.7 mm, the beam waist, and a length of 3 mm, the width of the aerosol soot flow tube. The detectors thus measure the scattered light, whereas the APS measured the number size distribution of soot in the mobility size diameter from 0.54 to 20 μm.

To study the morphology of soot particles, samples were collected by thermophoretic deposition onto the copper electron microscope grids with formvar coating placed on a frog-tongue probe device [135], designed by Dobbins and Megaridis [147] that inserted quickly and briefly into the soot flow path. This soot collection method avoids the possibility of soot impaction onto the grids. Soot samples were collected at two different flow rates, and their morphology was investigated by a TEM. Size distributions seen on the TEM were compared with APS measured number size distributions. Furthermore, Guinier inferred sizes given by light scattering were compared with the intensity-weighted distribution generated from the APS observed number size distribution.

6.3 Results

6.3.1 Miniature Soot Generator

Characteristics of soot generated from hydrocarbon combustion depend on the fuel equivalence ratio (ϕ) that typically controls the particles' concentration, size distribution, and compactness. It is defined as the actual fuel to air ratio used for the combustion to the stoichiometric ratio. If $\phi = 1$, the combustion is stoichiometric (complete combustion of

fuel). If $\phi < 1$, the combustion is lean with excess air, and $\phi > 1$, the combustion is rich with incomplete combustion. Condensing the water vapor present in the exhaust gas during combustion is determined by the value of dew point temperature. It is the saturation temperature at which water vapor starts condensing into a liquid at a particular pressure. The amount of water vapor in exhaust gas depends on the fuel used for the combustion.

Light scattering studies were conducted at equivalence ratios from $\phi = 0.13$ (air/fuel flow rate = 104) to $\phi = 0.48$ (air/fuel flow rate = 30). At an equivalence ratio less than $\phi = 0.13$ (air/fuel flow rate = 104), the signal to noise ratio was not large enough to measure the scattered light. On the other hand, we could not get the constant soot flow rate for an equivalence ratio greater than $\phi = 0.48$ (air/fuel flow rate = 30) due to the quick condensation of water vapor-deposited on the inner surface aerosol tube during combustion. Furthermore, the shape and appearance of the flame were visually checked and agreed with the observations described by Olfert [148]. Light scattering results for five different fuel flow rates were presented. TEM images were taken at two different flow rates at $\phi = 0.13$ (air/fuel flow rate = 104) and $\phi = 0.48$ (air/fuel flow rate = 30). Figure 6.3 shows the overview of ethylene and airflow rates used to generate soot.

Fuel (C_2H_4) (SLPM)	Air (SLPM)	Equivalence Ratio (Φ)	Air to Fuel Ratio (Flow Rate)	Partial Vapor pressure of water in the combustion product (kPa)	Saturation Vapor pressure of water at room temperature (kPa)	Dew point temperature for water vapor in the combustion product (°C)	Dew point temperature for water vapor at room temperature (° C)
0.330	10	0.48	30	6.40	3.17	37.40	25
0.270		0.39	37	5.26		33.80	
0.210		0.30	47	4.11		29.40	
0.150		0.22	67	2.95		23.80	
0.096		0.13	104	2.27		19.00	

Figure 6.3: *Five different flow rates used for soot generation with corresponding equivalence ratios and dew point temperatures for water vapor condensation in the combustion product. The tabulation indicates that when the air-to-fuel ratio is less than 65, water vapor condensation is expected, above which, no water vapor condensation.*

Figure 6.4 shows an example of TEM images for cooled soot particles at two different flow rates that corresponds to equivalence ratios $\phi = 0.13$ (air/fuel flow rate = 104) and $\phi = 0.48$ (air/fuel flow rate = 30). At equivalence ratio $\phi = 0.13$ (air/fuel flow rate = 104), water vapor condensation was not expected whereas, at $\phi = 0.48$ (air/fuel flow rate = 30), water vapor condensation was expected. TEM images indicated a wide range of particle size distribution produced in each flow rate, consistent with the APS measured number size distribution (Fig. 6.5(a)). When comparing images for these two flow rates, a noticeable difference in soot morphology is observed. Larger aggregates, i.e., hybrid particles, were observed in both cases, and their number availability decreases with decreasing fuel flow rates. The presences of these particles are an artifact of the inverted flame. For soot at equivalence ratio $\phi = 0.48$ (air/fuel flow rate = 30), images look like a long one−dimensional

chain-like structures supported by an extended Guinier regime with slope -1 (Fig. 6.6 at air/fuel flow rate = 30).

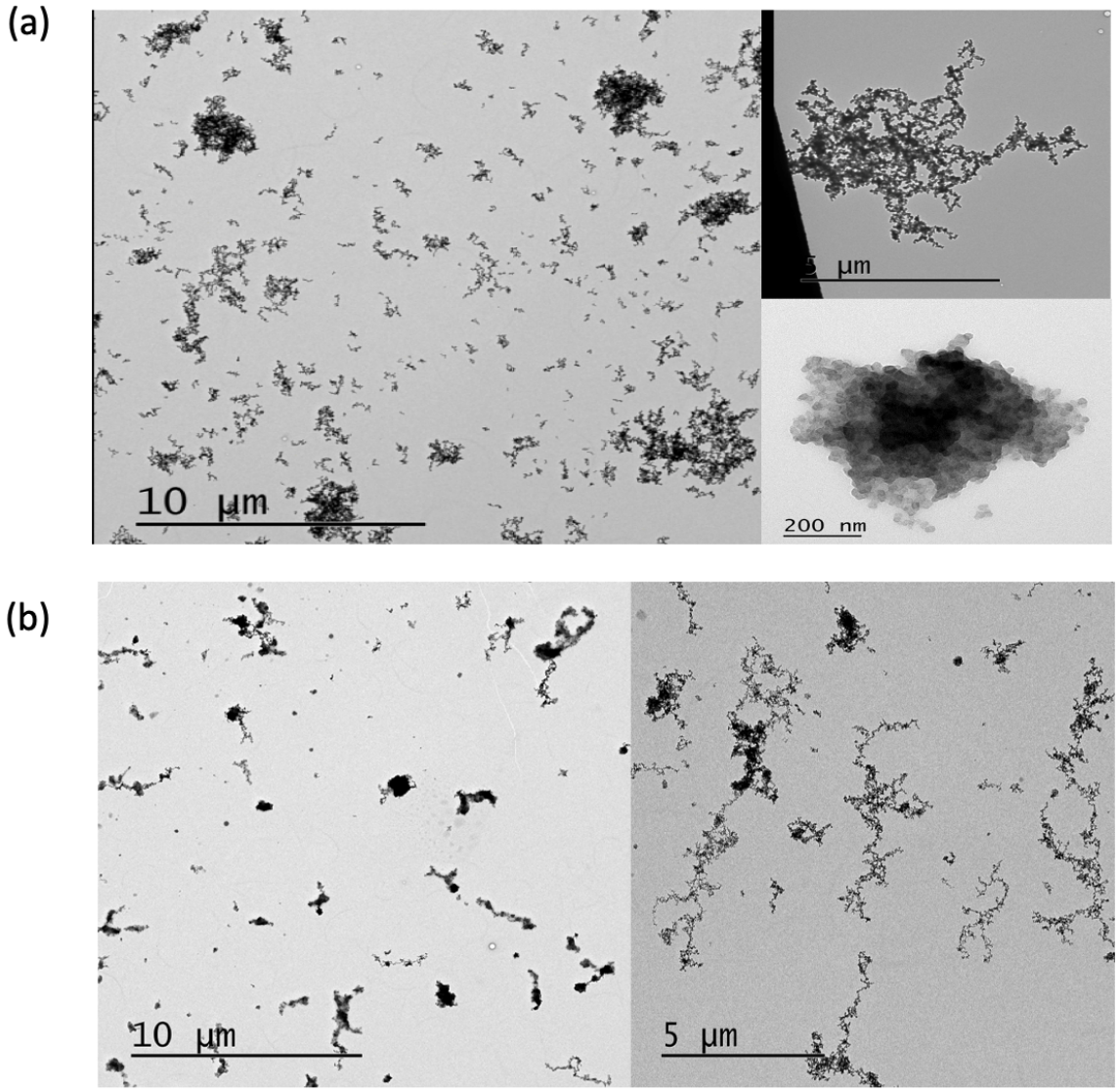

Figure 6.4: *TEM images of soot particles at two different flow rates (a) Air/Fuel flow rate = 67 and (b) Air/Fuel flow rate = 30. Pictures showed a wide size distribution with a non-homogenous morphology.*

The soot particle number size distributions generated at five different flow rates were

measured by a calibrated Aerodynamic Particle Sizer (APS 3321), shown in Fig. 6.5(a)) and corresponding intensity weighted distribution (Fig. 6.5(b)). The intensity weighted distributions were obtained by multiplying the number size distributions by their corresponding diameter to the fourth power, D^4 [14, 15]. We presented relative rather than absolute values to see the number particle size distribution trend generated at different fuel flow rates. The number particle size distributions observed at different fuel flow rates showed a similar trend observed by Olfert [148]. APS showed a quite wide size distribution such that smaller size particles increase with decreasing fuel flow rate, i.e., increasing air/fuel flow rates. Larger particle sizes were measured at all flow rates, consistent with the size shown by the TEM.

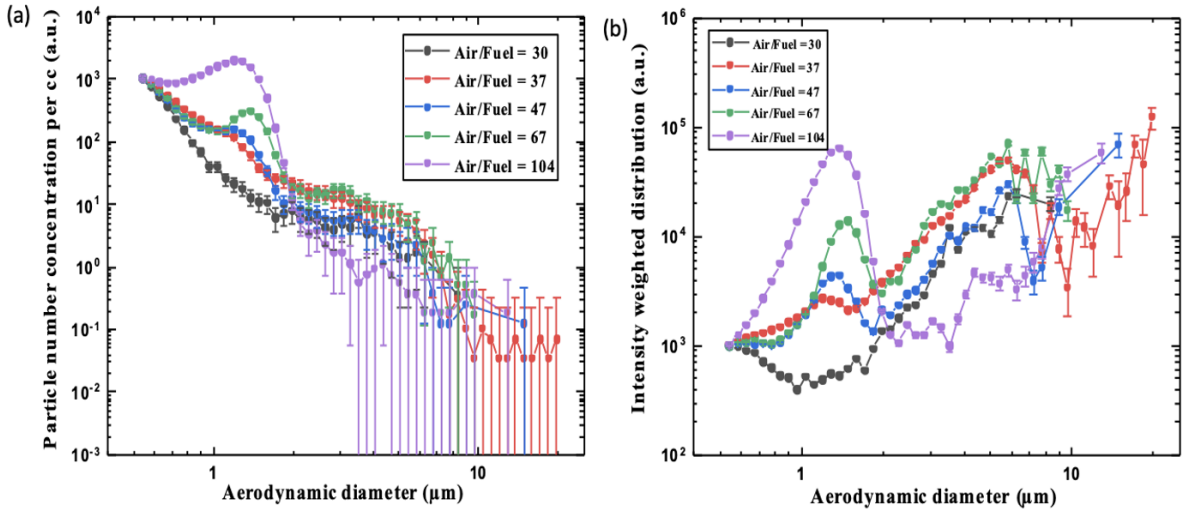

Figure 6.5: *(a) APS observed aerodynamic diameter number size distribution for five different air/fuel flow rates and (b) corresponding intensity weighted number size distribution.*

The measured light scattering data were plotted in Q-space and θ-space, as shown in Fig. 6.6. We multiplied the measured intensity by a certain factor to make it clear from one measurement to another. It is observed from the Q-space plot (Fig. 6.6(a)) that a Guinier regime followed by a constant slope indicating the power-law q^{-D_f} and an enhancement in the backscattering for all flow rates except at air/fuel flow rate = 104. Recall from Eq. 6.1 that D_f is the fractal dimension. The measured fractal dimension indicated that soot

consists of hybrid particles i.e., superaggregates. It is an aggregate composed of aggregates. If DLCA is allowed to proceed until the aggregates occupy an appreciable fraction of the space, a situation called cluster-dense limit, superaggregates occur. These superaggregates have a hybrid structure with a fractal dimension of D $\approx$ 2.5 at large length scales but are composed of smaller aggregates with fractal dimension of D_f = -1.8 at smaller scales [41–43, 138]. The θ-space (Fig. 6.6(b)) did not show any quantifiable pattern like the Q-space plot.

Our experimental results showed an enhancement in the backscattering near the maximum q = 2.4×10^5 cm^{-1}. The results indicated that an enhancement in the backscattering decreases with increasing air to fuel flow rate. Furthermore, it was found that at a small air to fuel ratio, a large amount of water vapor condensation took place compared with the large air to fuel ratio. Therefore, we speculate that a larger enhancement in the backscattering might be due to water droplets.

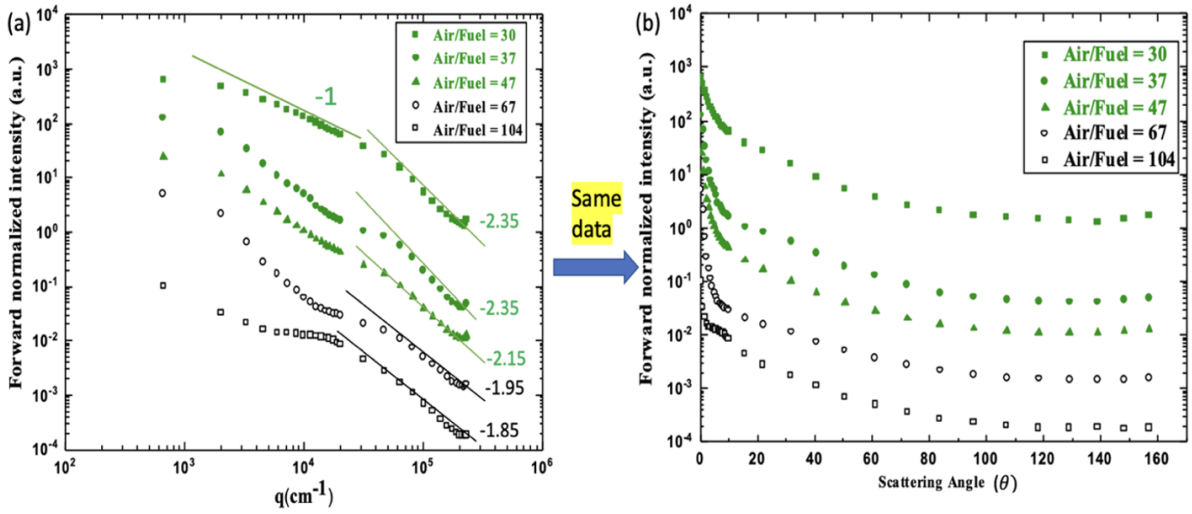

Figure 6.6: *Static light scattering intensity as a (a) function of scattering wave vector q and (b) scattering angle, θ from an air/ethylene flame generated soot at various flow rates.*

The Guinier regime is in the forward scattering regime of the particulate scattering. In this regime, the scattering is proportional to the diameter to the fourth power, i.e., D^4. To

account for this when comparing APS results to light scattering measurements, the APS size distribution is multiplied by D^4. That facilitated us to compare the size indicated by the Guinier regime to the intensity (light scattering) weighted size distribution. Figure 6.7 showed a side-by-side comparison for each flow rate. At a flow rate of air/fuel = 30 to air/fuel = 47, we see a single inflection indicating a single Guinier size, corroborating by the corresponding intensity weighted distribution (Figs. 6.7(a), 6.7(b), and 6.7(c)). Double inflection at the Guinier regime begins from air/fuel = 67 (Fig. 6.7(d)) that becomes pronounced at flow rate air/fuel = 104 (Fig. 6.7(e), left), consistent with the double peak seen on the intensity weighted distribution (Fig. 6.7(e), right)). Furthermore, the Guinier regime and intensity weighted distribution curve shown in Fig. 6.7 indicated the presence of submicron particles ($\leq$1 μm), consistent with the APS measured number size distribution (Fig. 6.5). The calculations showed considerable uncertainty in the large tail of the measured distribution because only a small fraction of the particles are there that contribute more to the scattering. This weighting is of utmost importance when comparing light scattering measurements made by the APS and similar devices.

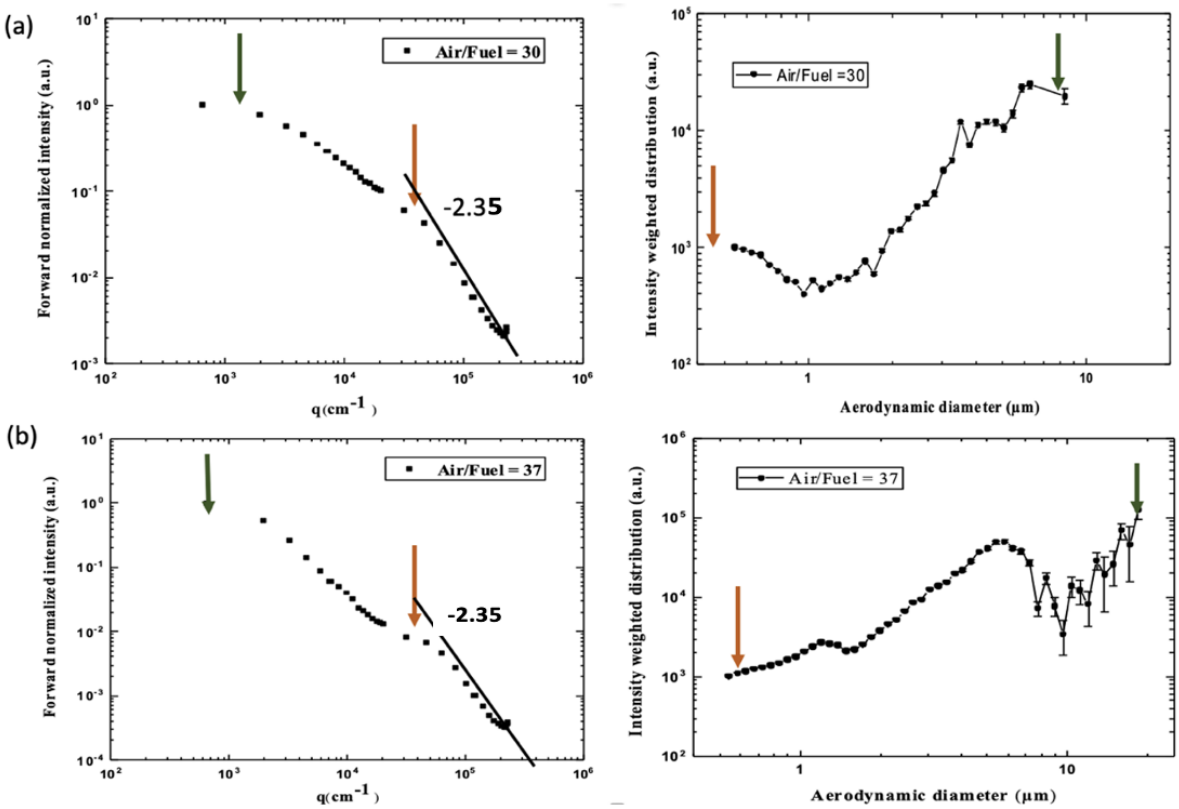
(a)
Air/Fuel = 30
-2.35
Forward normalized intensity (a.u.)
q(cm^{-1})
Air/Fuel =30
Intensity weighted distribution (a.u.)
Aerodynamic diameter (μm)
(b)
Air/Fuel = 37
-2.35
Forward normalized intensity (a.u.)
q(cm^{-1})
Air/Fuel = 37
Intensity weighted distribution (a.u.)
Aerodynamic diameter (μm)

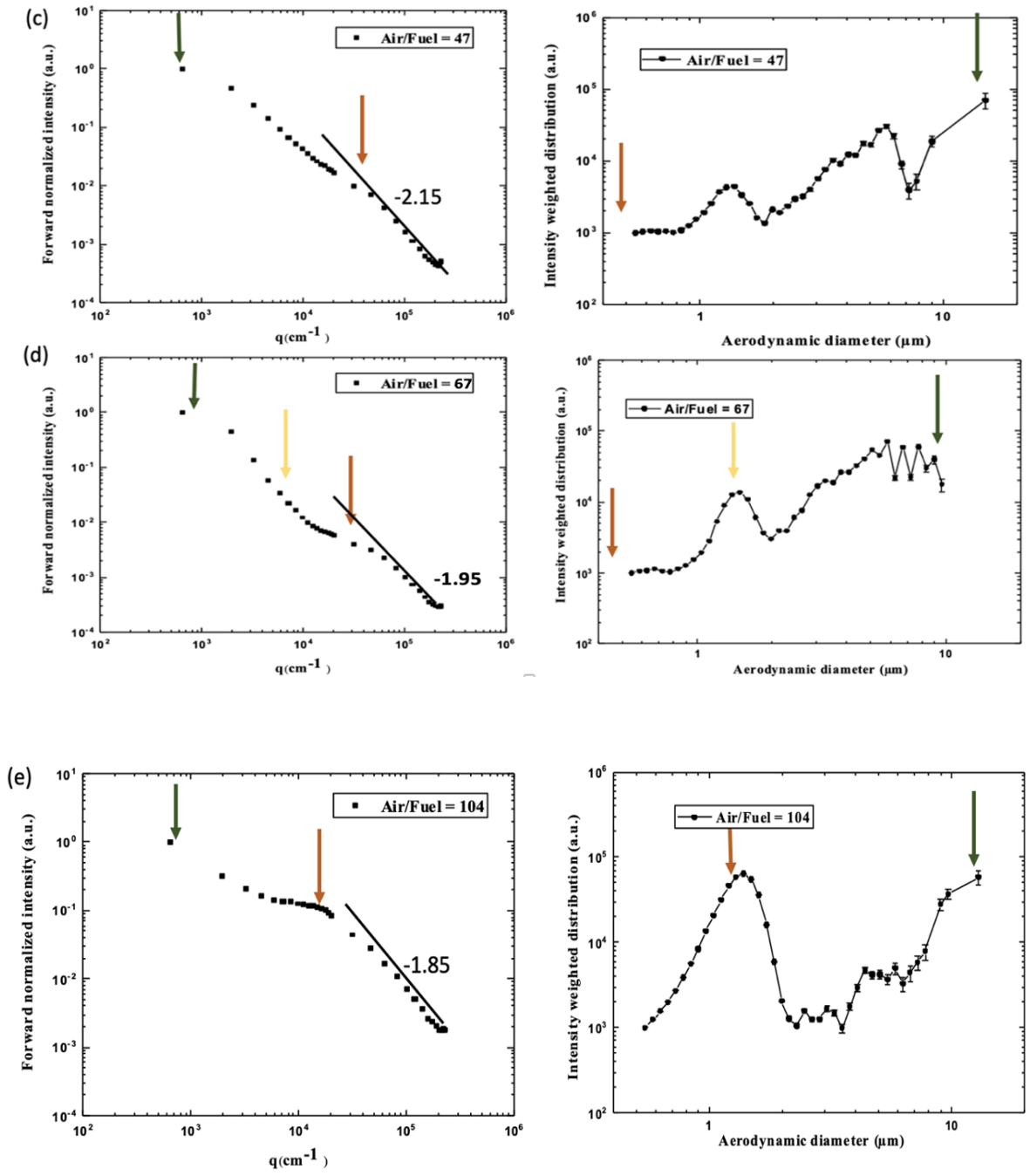

Figure 6.7: *Comparison of Guinier crossover observed experimentally with the intensity weighted distribution generated from APS observed number size distribution. Arrow with the same color indicates the experimentally observed Guinier crossover with the* q^{-1} *on number size distribution.*

6.3.2 Pre-mixed Burner

It has been observed that the amount of soot generated by a pre-mixed burner depends on the amount of fuel and oxygen used for the generation. In this study, the flow rates used to generate soot were randomly chosen such that the signal-to-noise ratio would be large enough to measure experimentally. When the flow rates of C_2H_4 , C_3H_8, and O_2 were 50, 50, and 70 ml/minute, respectively, there would not be enough signal-to-noise ratio to measure the scattered light. When we increased the fuel flow rates of C_2H_4 and C_3H_8 to 70 ml/minute, keeping the O_2 flow rate constant, there was a large signal-to-noise ratio to measure scattered light. The result (Fig. 6.8 ($C_2H_4/C_3H_8 = 1$)) showed an anti-correlation at small q in the range 635 cm^{-1} to $\simeq$ 6000 cm^{-1} (i.e., in the angle range 0.32° to 3°) with a power law exponent of -1.8, indicating a fractal dimension of -1.8. This is consistent with the fractal dimension of non-dense soot computed by the diffusion-limited cluster-cluster aggregation (DLCA) process [149–154]. Anti-correlation implies decreasing the intensity with decreasing q value. The anti-correlation might be due to a dense ensemble of many soot particles. In cluster-dense aerosol [41–43, 138, 139, 155–157], there is a possibility that scattered light from one soot particle gets reflected in the backward direction by the other soot particles.

We optimize the flow rates by which we could get the soot from the pre-mixed burner with no anti-correlation at small q. When the flow rates of C_2H_4 and C_3H_8 were 70 and 120 ml/minute with the same flow rate of O_2, we would be able to measure the scattered light from soot particles with no anti-correlations but a fractal dimension of -1.8, shown in Fig. 6.8 ($C_2H_4/C_3H_8 = 0.58$). The light scattering measurements at both fuel flow rates showed an enhancement in the backscattering, similar to that observed for the soot generated by the miniature soot generator.

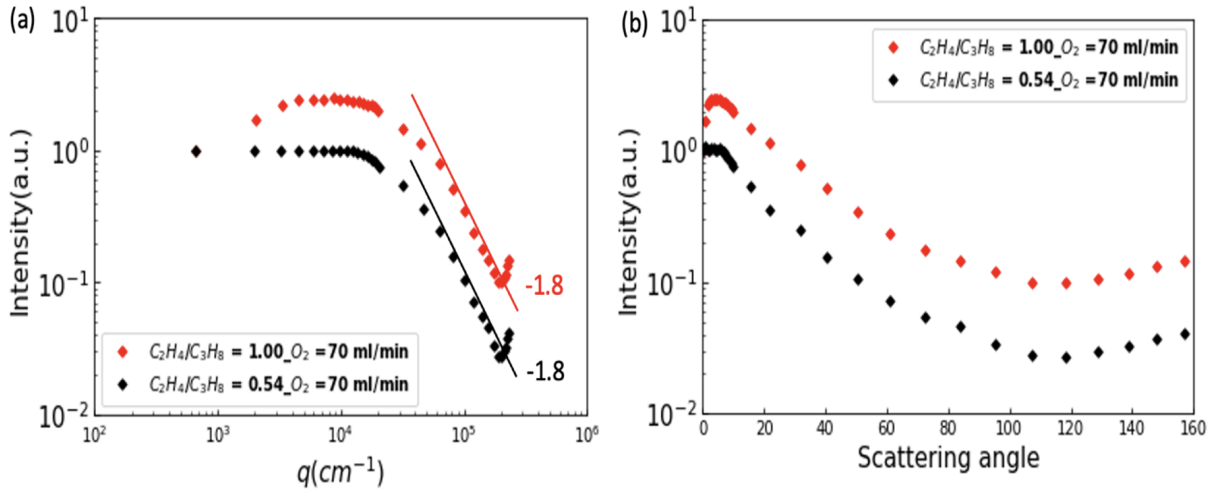

Figure 6.8: *Light scattering of soot produced from the premixed burner at two different fuel flow rates (a) plotted versus scattering wave vector, $q(cm^{-1})$ on a log-log scale, (b) plotted versus the scattering angle, θ.*

To explain this enhancement in the backscattering, we performed theoretical calculations similar to Liu and Mishchenko (2007) [128]. They performed the calculations using the efficient superposition T-matrix method for multisphere clusters in random orientation developed by Mackowski and Mishchenko(1996) [158]. They carried out the systematic study by varying the values of pre-factor, fractal dimension, monomer radius, number of monomers in the aggregates, and two values of refractive index $m = 1.75 + i0.435$ [159] and $m = 2 + i1$ [160] to represent various types of soot aerosols. The light used in their calculations was un-polarized (equivalent to circularly polarized light) with a wavelength of 628 nm. The results showed an enhancement in the backscattering. However, we have been using a vertically polarized incident light having a wavelength of 532 nm. The refractive index used for our calculations was $m = 1.6 + i0.6$ [20], soot refractive index for 532 nm, with a monomer and aggregate size equivalent to the experimentally measured values. The result is shown in Fig. 6.9 for both unpolarized and vertically polarized incident light. We got the result consistent with Liu and Mishchenko for unpolarized light; whereas, for vertically

polarized light, we did not observe an enhancement in the backscattering. Moreover, we performed calculations by considering a single particle (aggregate) at a time but still did not show an enhancement in the backscattering. Thus, we need additional work theoretically and experimentally to explain an enhancement in the backscattering for vertically polarized light. An enhancement in the backscattering might be due to inter-cluster multiple scattering in a cluster dense aerosol.

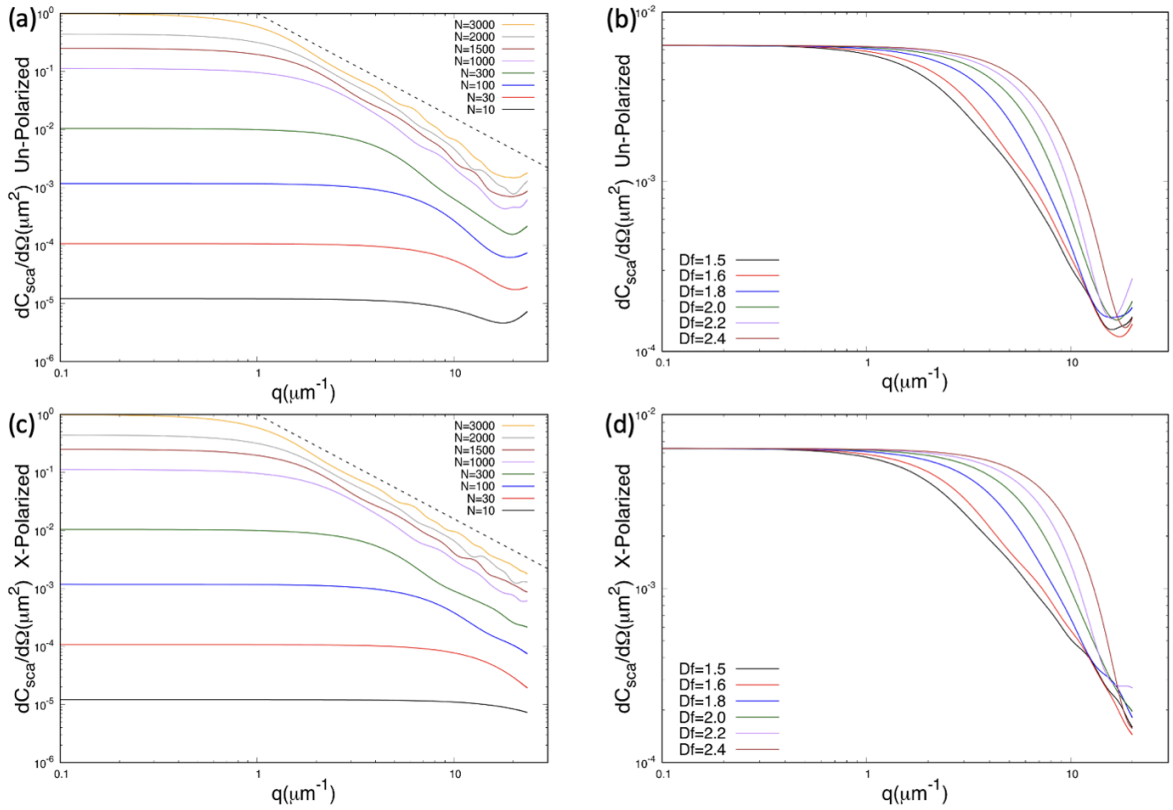

Figure 6.9: *The differential scattering cross section for a soot aggregate for an unpolarized incident light (a) changing the number of monomers in the aggregates (b) changing the fractal dimension of soot particles; for a vertically polarized incident light (c) changing the number of monomers in the aggregates, and (d) changing the fractal dimension of soot. Note that the differential scattering cross section is directly proportional to the scattered intensity.*

We analyzed the freshly produced soot particles from the premixed burner using a TEM (Fig. 6.10). The size distribution and morphology of the soot images seen on the TEM were consistent with the light scattering results (Guinier inferred size and fractal dimension). The TEM images showed a size distribution with no superaggregates, consistent with the size distribution measured by the APS as shown in Fig. 6.11. Figure 6.11 shows the APS measured number size distribution and corresponding intensity weighted distribution. The intensity weighted calculations showed that larger particles, presented even in one (≈ 3 μm) in thousand small (≈ 0.6 μm), contribute more to the light scattering. A large uncertainty could occur at the larger tail end of the number particle size distribution measurement, affecting the intensity weighted distribution considerably. The Guinier inferred diameter for $C_2H_4/C_3H_8 = 0.54$ would be calculated at around 1.12μm, consistent with the intensity weighted distribution (Fig. 6.11).

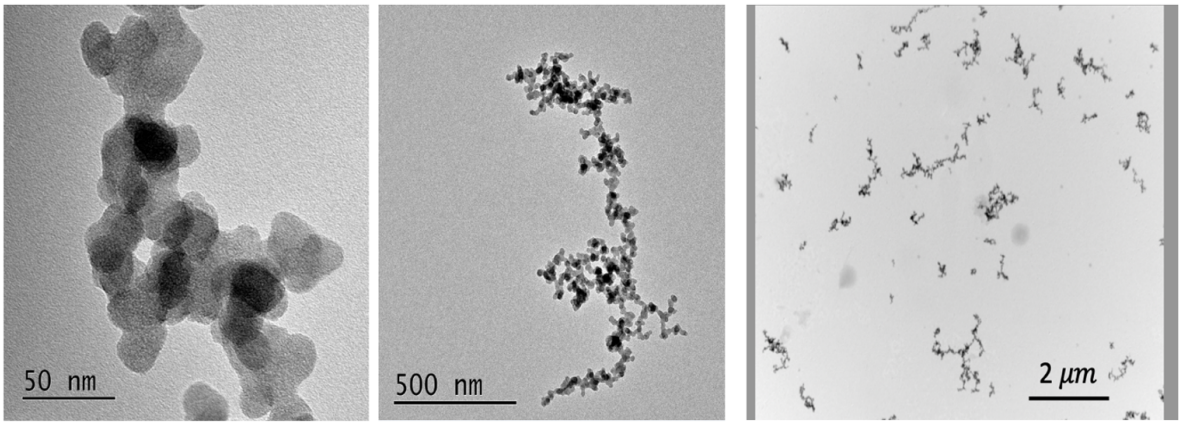

Figure 6.10: *TEM images for soot particles generated by pre-mixed burner.*

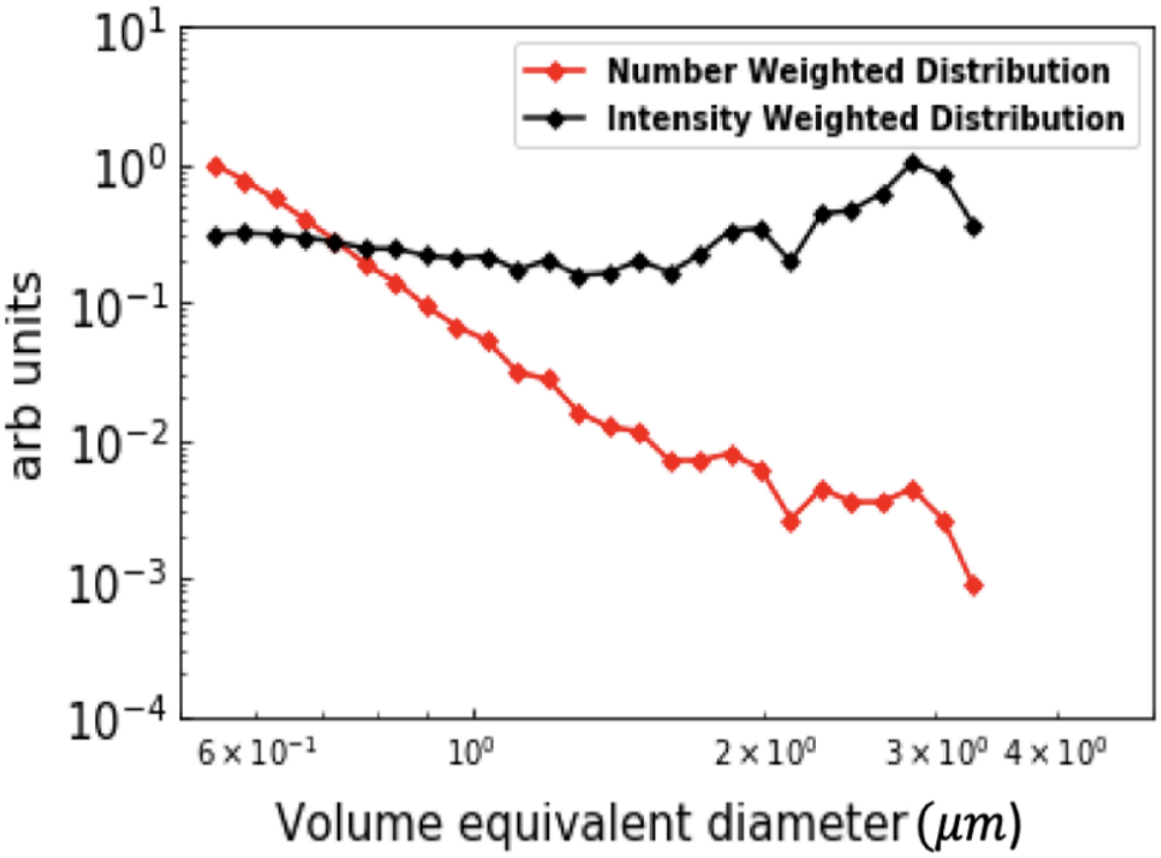

Figure 6.11: *Particle number distribution for soot particles generated for C_2H_4/C_3H_8 = 0.54, measured with the APS 3321 and transformed intensity weighted distribution with a weighting factor of D^4.*

6.4 Conclusion

From this work, we have learned that soot morphology and their size distribution depend on how they have been generated and the fuel flow rates used. The soot generated from the miniature soot generator took a long time to reach the scattering volume, enough to condense water vapor into droplets. The inferred size via the Guinier regime and a power-law exponent from the light scattering result indicates the condensed and large soot, consis-

tent with the TEM images. Whereas soot generated from the premixed burner reaches the scattering volume within a short time interval, not enough to condense. The light scattering inferred power-law exponent and Guinier size were consistent with TEM images. The premixed generated soot fractal aggregates are well described by diffusion-limited cluster-cluster aggregation. The soot morphology and size distribution depend directly on the time interval between soot generation and light scattering measurements.

During light scattering from soot particles generated by a miniature soot generator, we observed water droplets inside the soot-carrying tube within a very short interval of time at a low air/ fuel ratio. However, at a high air/fuel ratio, we could barely see water droplets forming inside the aerosol tube even after a long time. We did a stoichiometry calculation to determine dew point temperature that could predict the possibility of water vapor condensation to form a water droplet. Many parameters are needed to characterize the soot particles, viz aggregate size, monomer size, pre-factor, number of monomers presented in the aggregate, and fractal dimension. So, one needs to specify all these parameters accurately to compare the experimentally measured light scattering result with the theoretical calculations. Thus, accurate determination of each parameter involved in the calculations is of upmost importance. Moreover, we established correlations between water vapor condensation and the backscattering enhancement. Overall, experimentally measured enhancement in the backscattering for vertically polarized incident light would require more theoretical and experimental considerations.

Chapter 7

Linear Depolarization Ratio Measurements of Particles with Diverse Shapes, Sizes, and Refractive Indices

7.1 Introduction

Polarimetry measures the degree of polarization after scattering incident light from aerosol particles. The polarization characteristics depend on the particle's shape, size, and optical constants. Polarimetric observations of aerosols have been widely used to retrieve information on aerosol size and the refractive index [161, 161–163]. Linear depolarization ratio measurement is an important phenomenon used to characterize the aerosol and cloud particles, especially the data at the perfect backscattering yield important information about the particle. These data were used in lidar and remote sensing to characterize atmospheric aerosols in the earth's atmosphere [161, 163, 164, 164–169].

Depolarization is a measure of particles' non-sphericity. The non-sphericity and inhomogeneity of the particles will introduce depolarized components into the scattering. The degree of depolarization depends on the amount and complexity of the particles' deviation from the spherically symmetric shape and the particles' size. Depolarization arises predominantly from internal reflections. It is also helpful to detect whether the scattering is multiple or single. This is because the multiple scattering results in finite depolarization whereas single scattering does not. It is the multiple scattering that leads to depolarization. The light used for the experiment is vertically polarized, and the linear depolarization ratio for this incident light is

$$\rho_v = I_{VH}/I_{VV} \tag{7.1}$$

This is also known as the linear polarization ratio, μ_L [8]. In Eq. 7.1, I_{VH} and I_{VV} are the intensity of scattered light measured with a linear horizontal and a linear vertical polarizer for vertically polarized incident light, respectively. If there is no multiple scattering, $I_{VH} = 0$ so $\rho_v = 0$. However, multiple scattering will lead to a finite depolarization, $\rho_v > 0$.

The linear depolarization ratio can also be measured by measuring the ratio of the cross-polarized to the co-polarized scattered intensity, represented by μ_L

$$\mu_L = \frac{I_{cross-pol}}{I_{co-pol}} \tag{7.2}$$

"Co-polarized" means the incident and detected polarizations are parallel, and "cross-polarized" means the incident and detected polarizations are perpendicular to each other. For Rayleigh particles of any shape, and particles with spherical symmetry, we expect $\rho_v = 0$, i.e., the scattered light is completely polarized in the same direction as that of incident polarizations [18].

In this chapter, we reported the measurement of the degree of linear depolarization ratio from aerosolized, micron-sized particles with diverse shapes, sizes, and refractive indices. That includes irregular and nearly spherical Aluminum abrasive (Al_2O_3), Arizona road

dust, Silicon dioxide (SiO_2), Molybdenum disulfide (MoS_2) particles. Hence, we performed the linear depolarization ratio measurements for a wide range of particles with diverse micro-physical properties. The measurements were performed at a wavelength of 532 nm, covering the scattering angle range from 0.32° (extreme forward scattering) to 177.6° (near perfect backscattering). The qualitative comparison of measured data with the theoretical calculations was carried out with the model computations using spheroids and Gaussian random spheres.

7.2 Results

Figure 7.1 shows depolarization ratio measurements for nearly spherical silica (SiO_2) of two size distributions and molybdenum disulfide (MoS_2) particles. The refractive index for silica and molybdenum disulfide particles were $m = n + i\kappa = 1.46 + i0$ and m = 3 + i1.5, respectively. For spherical particles, the depolarization is zero since the matrix elements F_{11} equals F_{22}. But in our measurements (Fig. 7.1(a)), we see the depolarization reaches a maximum of around 15%, which could not be considered an experimental error. The interesting point is that depolarization seems to be size-independent. That might be due to the nearly spherical shape of the silica particles. The microscopic pictures of these particles were shown in 3.1. However, the linear depolarization ratio for molybdenum disulfide particles (Fig. 7.1(b)) measured smaller than silica although the MoS_2 particles are irregular in nature (Fig. 3.6). That might be due to the high values of the imaginary part of the refractive index, killing the depolarizability of the particles.

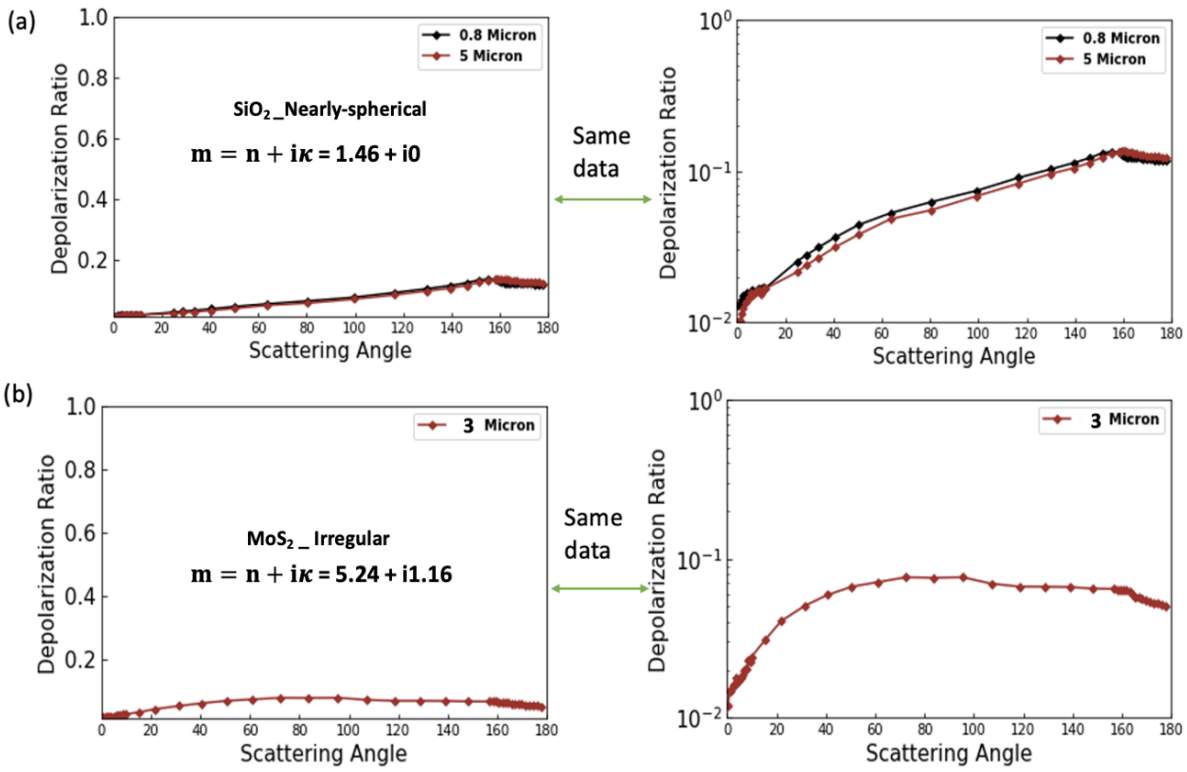

Figure 7.1: *Linear depolarization ratio for (a) nearly spherical silica (SiO_2) particles and (b) irregular molybdenum disulfide (MoS_2)particles.*

Figure 7.2 shows the measured linear depolarization ratios for four different aluminum abrasive grits particles and Arizona road dust particles. The linear depolarization ratio for all these dust particles showed a similar change in the values versus the scattering angle. The results show that at the extreme forward scattering regime, there is a negligibly small depolarization. In this regime, the scattering is dominated by diffraction, eliminating the possible internal reflections that cause the depolarization. With an increasing the scattering angle, the depolarization ratio also increases, and after reaching the maximum value at a certain angle in the side scattering regime, it starts to fall. Furthermore, the results show the linear depolarization ratio dependency on particle size, shape, and refractive index. More data are required to get a clear understanding of the linear depolarization ratio for aerosol particles. Note that the sizes indicated in Fig. 7.2 are the median size. The results suggest

that as the particle size grows, so does the linear depolarization ratio for a given particle with the same optical constant.

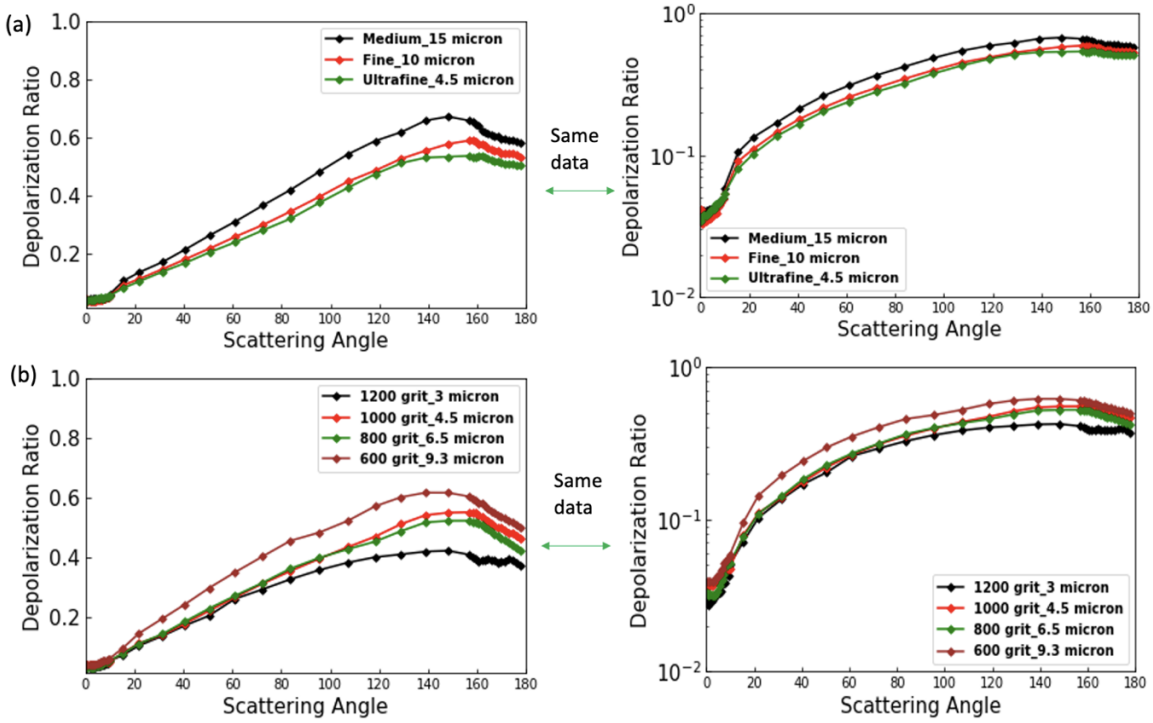

Figure 7.2: *Linear depolarization ratio for (a) Arizona road dust particles, and (b) Aluminum abrasive (Al_2O_3) particles. It is measured for vertically polarized incident light of wavelength 532 nm.*

Figure 7.3 shows the linear depolarization ratio, calculated from the measured scattering data presented by the Amsterdam-Granada group [31]. They have measured light scattering from various irregularly shaped particles at two different wavelengths, 441.6 nm, and 632.8 nm. They did not measure scattering by using vertically polarized incident light as we did at KSU; instead, they measured different scattering matrices using unpolarized light. From those tabulated (measured) values of different scattering matrices [26, 30, 33], we performed a simple algebra to get linear depolarization ratio values is shown in Fig. 7.3. Their measured values ranged from 3° to 177°. The general trend of change in linear depolarization ratio

values versus the scattering angle is similar to that we measured at KSU, shown in Figs. 7.1 and 7.2.

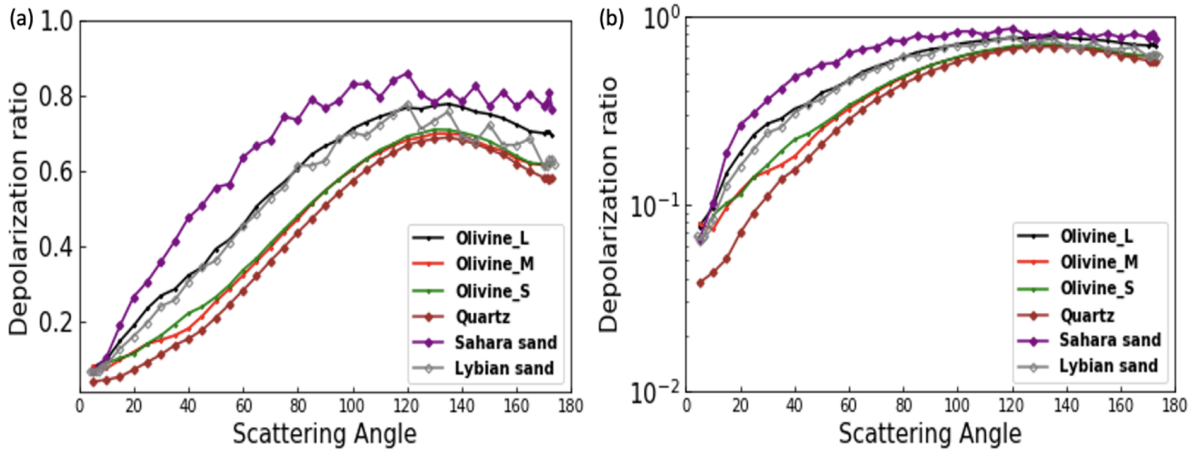

Figure 7.3: *Linear depolarization ratio for different dust aerosol particles presented in (a) linear, (b) semi-log scale versus the scattering angle, as reported by the Amsterdam-Granada group. Olivine L, Olivine M, Olivine S, Quartz measured at $\lambda = 441.6$ nm. Sahara and Lybian sand were measured at $\lambda = 632.8$ nm.*

We used a numerically exact T-matrix method to calculate the measured depolarization ratio from different dust particles with diverse micro-physical properties. First, we simulate our particles, assuming the irregular dust particles to be smooth spheroids and nearly spherical dust particles by Gaussian Random spheres. We further assume that spheroids and Gaussian random spheres are randomly oriented and form a statistically isotropic and mirror-symmetric ensemble. Note that we are looking for a general pattern of linear depolarization ratio due to scattering with changing the particles' size, shape, and refractive index, not a one-to-one correspondence comparison.

Figure 7.4 shows the linear depolarization ratio calculations as a function of the particle's effective radius (ranges from submicron to micron) for a spheroidal-shaped particle with an aspect ratio of 2 for two different refractive indices $m = 1.33$ and $m = 1.76$. The forward scattering regime is dominated by diffraction, giving little or no depolarization.

The depolarization increases with an increase in scattering angle, θ as the contribution from diffraction is dominated by internal scattering and surface reflection in the side and backscattering regime. The linear depolarization ratio versus the scattering angle shows a similar pattern for both refractive index values. For both the refractive indices, the linear depolarization ratio for the particles with a size less than the wavelength of light used was almost independent of the scattering angle. The calculated values were predominantly small, with the highest value not even reaching 1%. As the particle size grows, so does the linear depolarization ratio, randomly but not monotonically. The linear depolarization ratio would reach a maximum of around $40-50\%$ for most cases while reaching near 100% in some cases. However, for most cases, the maximum linear depolarization ratio lies around 120°, in the side scattering angle regime. Overall, the compared linear depolarization ratio values for both refractive indices indicate that one cannot get a coherent describable pattern. Each data value shows a peculiar variation with scattering angle, θ.

The linear depolarization ratios at two refractive indices show a contrasting difference in the backscattering regime, where there is an abrupt decrease when $\theta > 160^{\circ}$, in LDR values for $m = 1.76$ compared to $m = 1.33$. In addition to this, LDR values at the backscattering regime are randomly evolved just like the phase function [24] as it is highly sensitive to the particles' microphysical properties. However, the general trend is that LDR values are negligibly small at the forward scattering regime, significant and definitive values at the side scattering regime that generally falls at the backscattering regime. The overall results suggest that as the particle size grows, so does the polarization but not monotonically with the particle size.

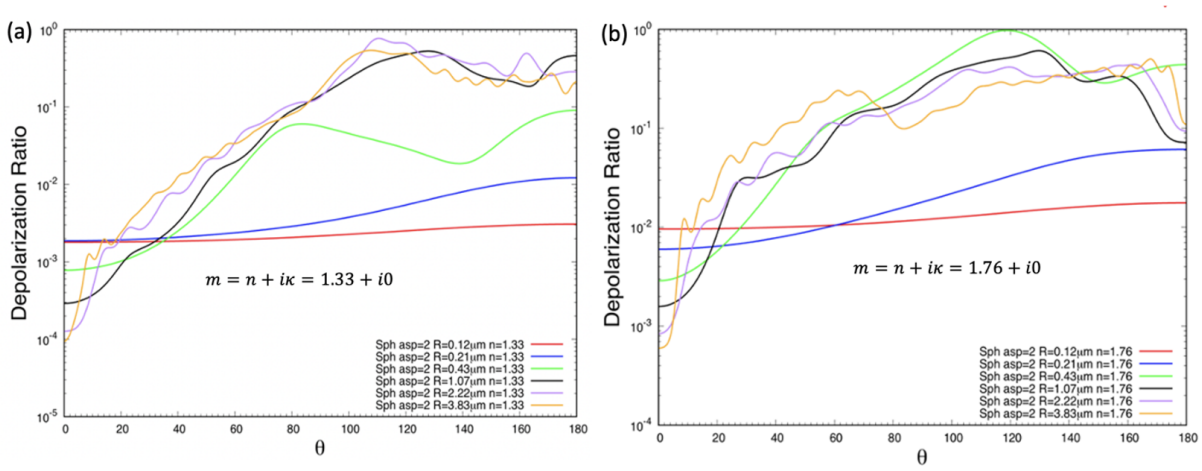

Figure 7.4: *Depolarization ratio calculations for spheroidal-shaped particles with varying sizes for an aspect ratio of 2 and refractive index of (a) $m = 1.33$ and (b) $m = 1.76$. The calculation was carried out for vertically polarized incident light.*

Figure 7.5(a) shows the linear depolarization ratio as a function of shape effects. For this, we chose a sphere with a radius of 3 m such that asphericity changes from 1% to 20%, keeping the same refractive index $m = 1.5$ and a particle size of r = 3 μm. The results show that LDR tends to increase with increasing the asphericity. Figure 7.5(b) shows the calculations for linear depolarization ratio for a fixed real ($m = 1.33$) but varying imaginary part of the refractive index, which is quantified by a parameter κKR, called relative skin depth [66]. The results shows that with increasing the value of κkR, the LDR tends to decrease. The decrease in LDR values might be due to absorption that causes to reduce the total number of internal reflections, causing a lesser depolarization ratio. These results were similar to that calculated by Liu and Mishchenko [170].

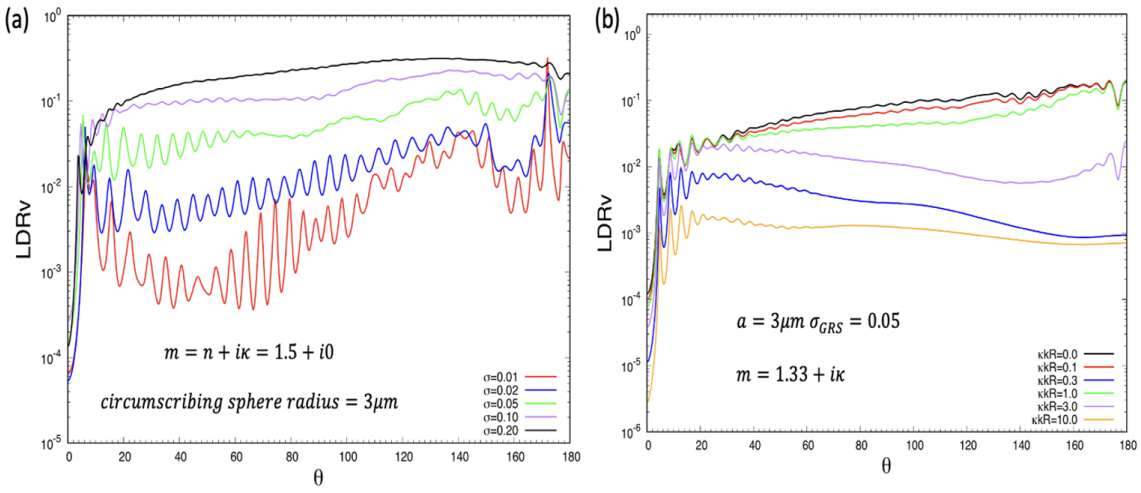

Figure 7.5: *Linear depolarization ratio calculations for (a) Gaussian random spheres with a change in the asphericity for a fixed size $r = 3\ \mu m$ and a refractive index $m = 1.5 + i0$, (b) for a fixed real ($m = 1.33$) but changing imaginary part of the refractive index, i.e., changing the parameter, κkR.*

.

7.3 Conclusion

The non-zero linear depolarization ratio values indicate the presence of non-spherical aerosols and are highly sensitive to particles' shape, sizes, and refractive index. The linear depolarization ratio tends to increase with particle size and decreases with increasing the absorption which is quantified by the parameter, κkR, the relative skin depth. Furthermore, the depolarization decreases with increasing refraction. The larger absorption and refraction cause the incident light to get reflected from the outer surface of the particles, reducing the number of internal reflections and hence, the linear depolarization ratio. It is understood that a large real part of the refractive index obstructs the incident light from penetrating the particles so that the total number of internal reflections within the particle decreases. That results in a decrease in the linear depolarization ratio values.

The measured and calculated data showed a similar linear depolarization pattern versus the scattering angle with identical micro-physical properties of the particles. At the forward scattering regime, the linear depolarization ratio is negligibly small. We propose that the weak depolarization at the forward scattering is due to diffraction. The linear depolarization increases as the angle increases and reaches the maximum at the side scattering, which generally drops at the backscattering regime. Overall, the measured and calculated data on linear depolarization ratio show size, shape, and refractive index dependence.

Chapter 8

The Sensitivity of Light Backscattering with the Change in the Size and Refractive Index

8.1 Introduction

The angular distribution of light scattered by a particle is the most fundamental manner in which to describe the scattering. This distribution is typically given in terms of the scattered intensity, which is proportional to the differential scattering cross-section as a function of the scattering angle. In this chapter, we demonstrated how backscattering behaves with the change in the forward scattering regime. Again, in this work, we plotted and analyzed the data with both Q-space and θ-space perspectives [25, 45]. Q-space finds the trend that distinguishes forward and side scattering while θ-space illustrates entirely different functionalities in the backscattering regime. The whole scattering angle is divided into the following three regimes: 1). The Forward Scattering Lobe: This regime has a constant intensity (q and θ independent) when qR $<$ 1 and ends in the Guinier regime near qR $\simeq$ 1 ($\theta\approx$ $\lambda/2\pi$R), where R is the effective radius of the particle. This regime is

diffraction-dominated, hence only weakly dependent on particle refractive index and shape. 2). The Side Scattering Regime: This regime is characterized by emerging power laws with q and includes the refraction hump. This regime contains a cross-over from diffraction to refraction-dominated. 3). The Backscattering Regime: This regime begins when the scattering begins to increase relative to the side scattering with increasing angle and hence q. This regime includes the generalized rainbows and the glory. This regime separates itself due to its complex functionalities on size and refractive index and is a mix of both refraction and wave interference.

These regimes have been observed but not emphasized in some of our previous work [44–46]. Here we use experimental data and theoretical calculations to illustrate this new description. A detailed explanation for the experimental setup can be found in [25].

8.2 Results

We measured the scattered light from nearly spherical water droplets generated by a 6-jet collision nebulizer. The Mie theory was used to fit the measured scattering data. The fit assumed that the scattering originated from an ensemble of spherical water droplets that obeyed a log-normal distribution. For this, we introduce P(r), which is the unnormalized log-normal size distribution given by [19, 20]

$$P(r) = exp(-ln^2(\frac{r}{r_0})/2ln^2\sigma) \tag{8.1}$$

where r_0 is the most probable radius and σ is the geometric width of the size distribution.

Figure 8.1 shows a comparison between Mie calculations and experimental results, plotted in Q-space and the conventional θ-space. Most importantly, we fitted Mie theory to the measured‘ scattering data with the best possible combination of size distribution such that the Guinier regime perfectly matches with one another at the forward scattering regime (Fig. 8.1(d)) along with the nearest matching at the side and backscattering regime. The

best combination for the size distribution was a weighted mean radius of 1.25 micron with a geometric width of 1.45 for a log-normal distribution, provided that the refractive index of water is $m = 1.33$. Note that the fit is quite good in the forward and side scattering regimes when viewed in either Q-space or θ-space; see Figs. 8.1(a) and 8.1(c), respectively. However, Fig. 8.1(b) shows that the fit is poor in the backscattering regime. Another interesting point we observed (Fig. 8.1(d)) is that the theory showed a dip at an angle $\theta \approx 10^{\circ}$ in θ-space (correspondingly at q $\approx$ 20,000 cm^{-1} in Q-space) but not observed experimentally. We understood that the lack of dip for our experimentally observed data might be due to the non-sphericity of water droplets, consistent with the results seen for slightly aspherical particles [171].

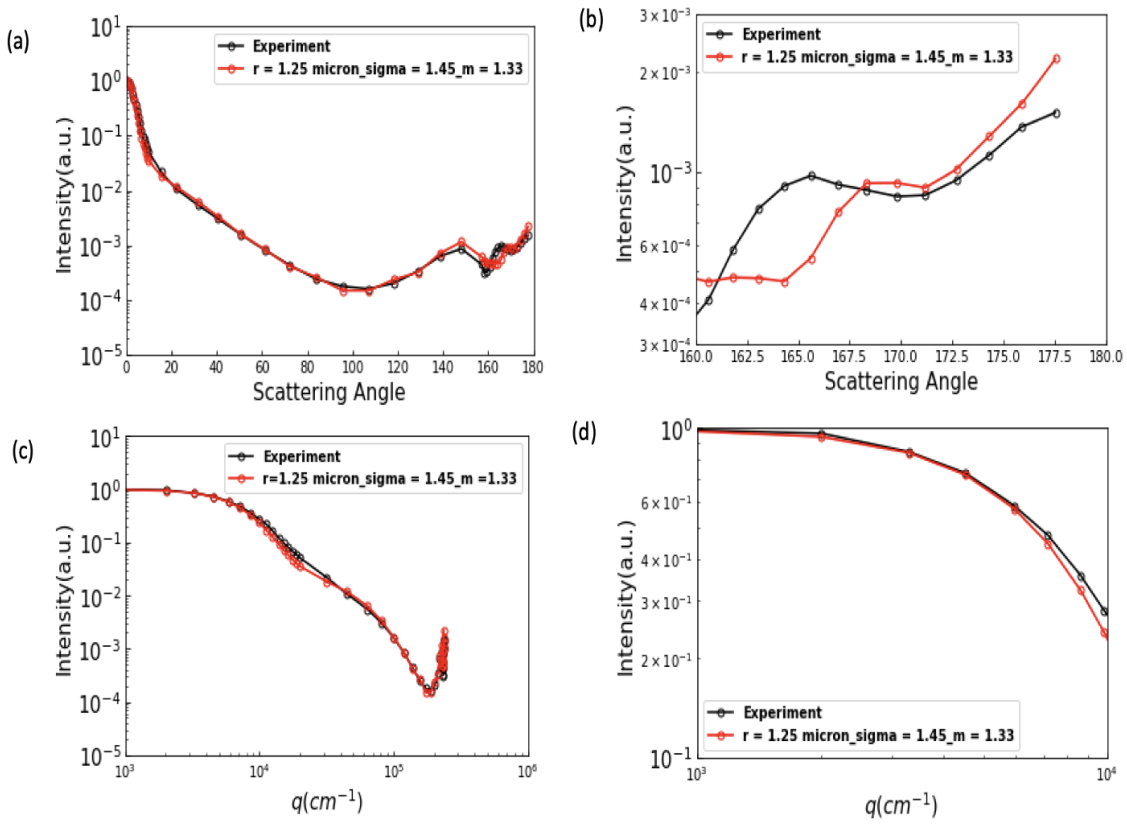

Figure 8.1: *A comparison between Mie calculations and experimental results plotted both in Q-space and the conventional θ-space. The data are normalized to 1.0 at the smallest angle or q. Fitting our experimental data over the entire angular range, forward, side, and backscattering regimes, with the theoretical Mie code, averaged over the size distribution, yielded the best fit weighted mean radius of $r_0 = 1.25\mu m$ with a geometric width of $\sigma = 1.45$ for a log-normal distribution.*

.

To understand the poor matching at the back, we did a systematic study by changing the size distribution and refractive index. The sensitivity of the backscattering regime with size distribution is demonstrated systematically in Figs. 8.2 and 8.3. The size distribution was changed in two ways: (1) the most probable size by 2.5% (Fig. 8.2) and (2) the width of

the size distribution by the same amount (Fig. 8.3), keeping the refractive index constant at $m = 1.33$. Both calculations show similar results: well explained, ordered forward scattering regime and disordered and randomly evolved backscattering. Both Figs. 8.2 and 8.3 show the Guinier regime towards the smaller q (hence, θ) for larger particle size distribution. It is the Guinier regime that indicates the size of the particle, i.e., the Guinier regime at smaller q indicates the larger size particle and vice-versa. In light scattering, larger particles contribute more to the scattering than the smaller particles. This implies that the forward scattering is well explained and ordered (8.2(d) and 8.3 (d)), unlike the backscattering regime (8.2(b) and 8.3 (b)).

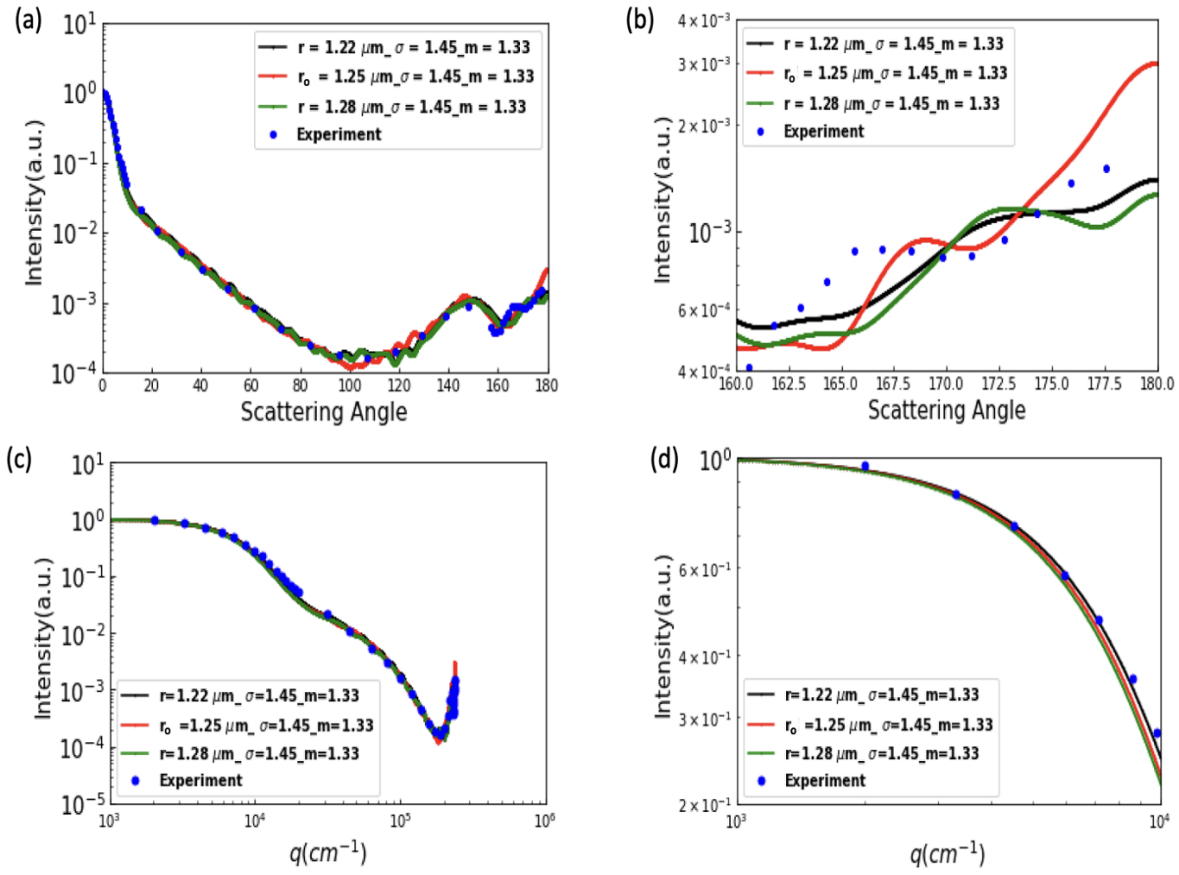

Figure 8.2: *Comparison of the measured forward normalized light scattering intensity with theoretical Mie calculations for a 2.5% relative change in the weighted mean radius of* $r_0 = 1.25\mu m$ *for a constant geometric width of* $\sigma = 1.45$ *and a refractive index of* $m = 1.33$*. Part (a) is plotted linearly as a function of scattering angle,* θ*. Part (b) is a magnified graph for the backscattering regime (*θ*-space). Part (c) plots the same data versus q (*cm^{-1}*) in a log-log scale called Q-space analysis. Part (d) is a magnified graph for the forward scattering regime (Q-space).*

.

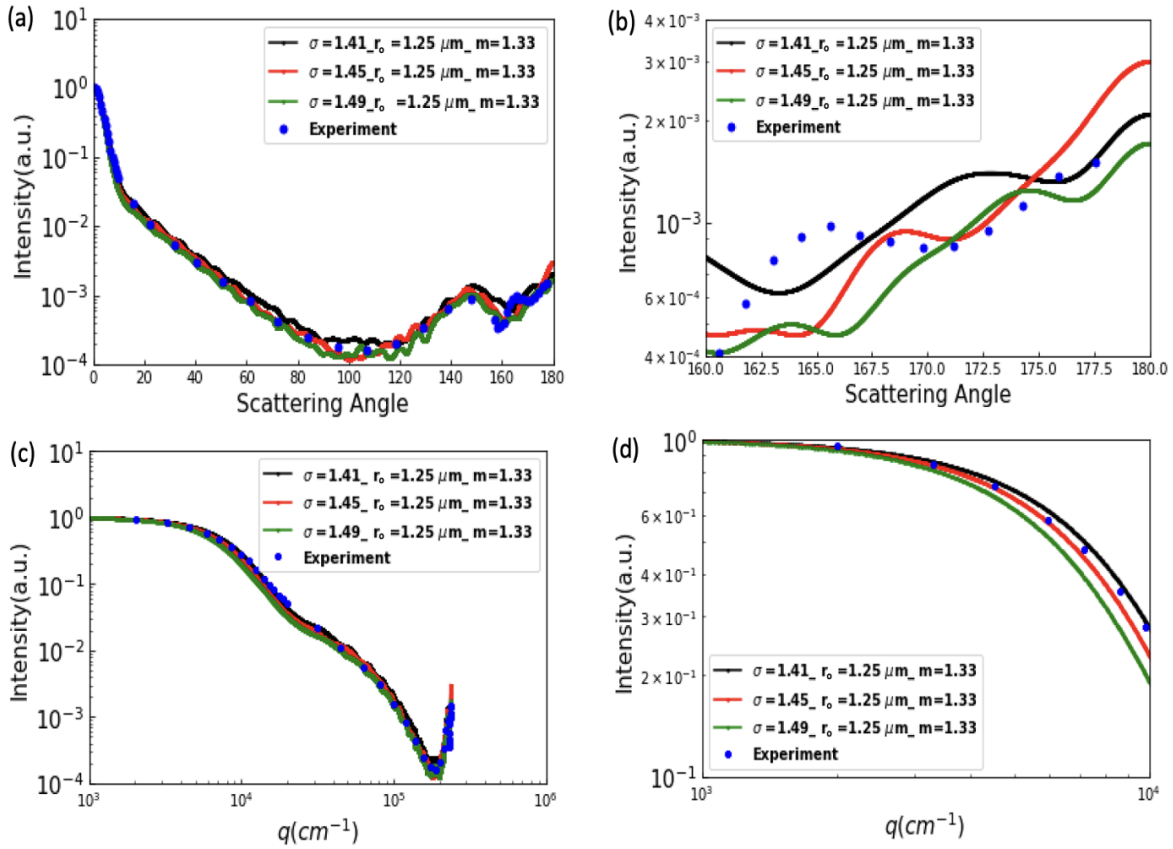

Figure 8.3: *Comparison of the measured forward normalized light scattering data with theoretical Mie calculation with a weighted mean radius of* $r_0 = 1.25\mu m$ *and refractive index of* $m = 1.33$ *for a 2.5% relative change in the geometric width of* $= 1.45$. *Part (a) is plotted linearly as a function of scattering angle,* θ. *Part (b) is a magnified graph for the backscattering regime (*θ*-space). Part (c) plots the same data versus* $q(cm^{-1})$ *in a log-log scale called Q-space analysis. Part (d) is a magnified graph for the forward scattering regime (Q-space). The intensity axis of Figs. (b) and (d) are scaled equivalently for comparison.*

.

During the generation of water droplets from the nebulizer, the temperature inside the nebulizer was decreased, leading to a small–but significant–change in the refractive index of water. We demonstrated how such a small change in the refractive index affected the

scattered intensity at the backscattering regime. The refractive index of water depends on its temperature, and the wavelength of light used [172, 173]. With the data provided in [173], we have shown calculations for five different values of the refractive indices corresponding to the temperatures 10°C, 20°C, 30°C, 40°C, and 50°C. Figure 8.4 demonstrates how a small change in the refractive index causes a noticeable difference in the scattering pattern at the backscattering regime. In these calculations, we used a fixed size distribution of a weighted mean radius of 1.25 micron with a geometric width of 1.45 for varying the values of refractive indices. We got a result similar to Figs. 8.2 and 8.3, a describable forward and chaotic backscattering regime. The overlapping at the forward scattering regime indicates that forward scattering regime depends on the size distribution and little or no dependency on the particle's refractive index (Fig. 8.4(d)). The overlapping at the forward scattering regime was expected since we used the same size distributions for all calculations. Still, the backscattering regime shows dependencies sensitive to small refractive index changes and non-systematic dependency on the refractive index (Fig. 8.4(b)). That illustrates the sensitivity of the backscattering regime with the change in the refractive index values.

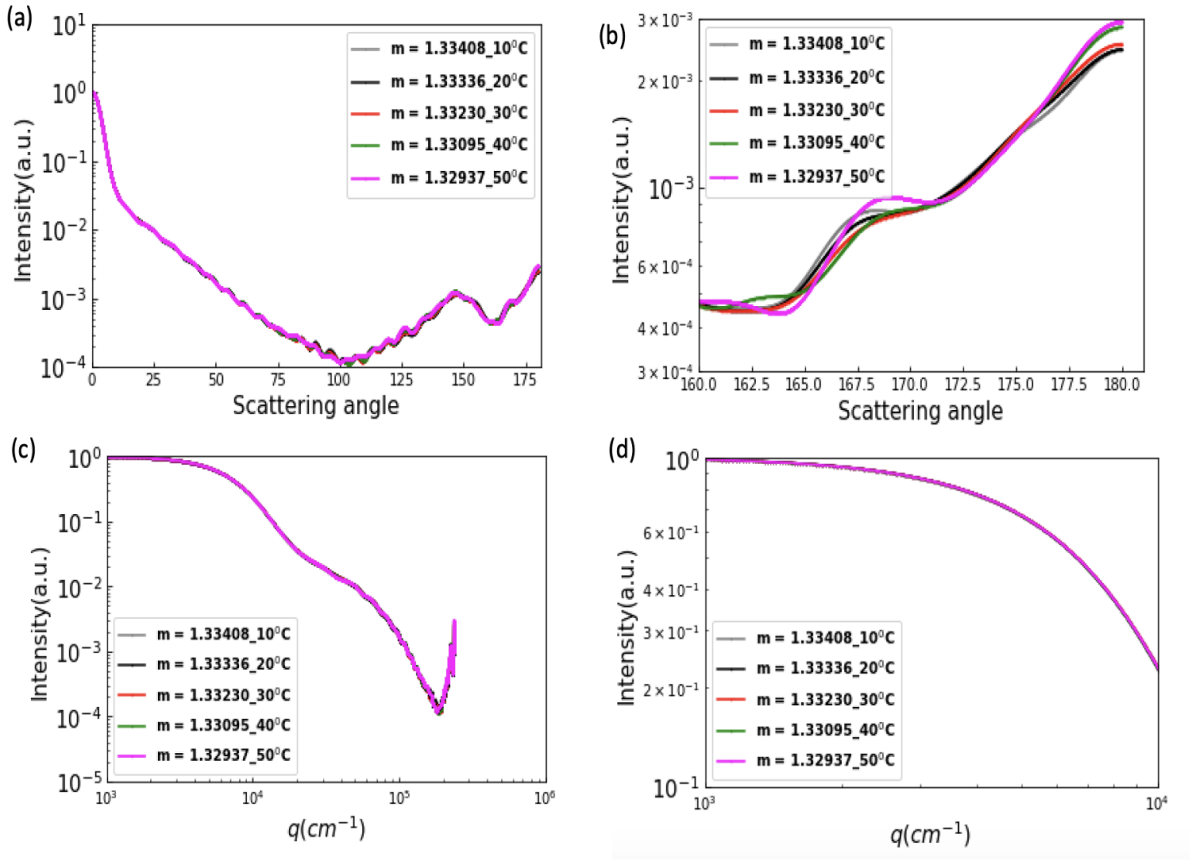

Figure 8.4: *Comparison of the measured forward normalized light scattering data with theoretical Mie calculation with a weighted mean radius of* $r_0 = 1.25\mu m$ *and a geometric width of* $\sigma = 1.45$ *for a log-normal distribution for different refractive indices corresponding to different temperatures. Part (a) is plotted linearly as a function of scattering angle,* θ*. Part (b) is a magnified graph for the backscattering regime (*θ*-space). Part (c) plots the same data versus* $q\ (cm^{-1})$ *in a log-log scale called Q-space analysis. Part (d) is a magnified graph for the forward scattering regime (Q-space). The intensity axis of Figs. (b) and (d) are scaled equivalently for comparison.*

.

8.3 Conclusion

This work demonstrated that the forward regime has simple dependence on size and a minor dependence on the refractive index. The side regime has describable dependencies on both size and refractive index. The backscattering regime also depends on the size and refractive index but in a much more extreme and chaotic manner. Overall, this work demonstrates the sensitivity of backscattering with the change in the particle size and refractive index. These results put forth an idea for dividing and studying the whole angular scattering range into forward, side, and backscattering regimes. Detailed work would be needed to understand this proposed idea clearly.

Chapter 9

Conclusions and Future Work

We presented the light scattering study of different aerosol particles with diverse sizes, shapes, and refractive indices. We used our own built experimental setup to measure the scattering from an extreme forward scattering regime (0.32°) to a backscattering regime (177.6°) [19, 25]. The ability to measure such a small angle engenders the need for logarithmic plotting of the data versus the independent scattering variable. That introduces using a scattering wave vector, q such that $q = (4\pi/\lambda)Sin(\theta/2)$, where λ is the optical wavelength and θ is the scattering angle, called the Q-space analysis. But this analysis method compresses the backscattering data showing no functionality. This required plotting the data versus the scattering angle, θ. With the application of these two methods, one can get a comprehensive description of the light scattering. This setup measured the scattered light through 31 different channels simultaneously, but 45 channels overall, with advantages over other setups [26, 35–39]. Our setup was divided into three regimes, namely: forward, side, and backscattering regime. Separate calibration techniques were applied to calibrate each regime. This setup can measure all six independent scattering matrix elements needed to get complete information about the scatterer.

The measured light scattering data were compared with the Mie calculations, calculated by using the number size distributions measured by the aerodynamic particle sizer (APS)

at the scattering volume. The results agreed well for nearly spherical particles. Still, there was good agreement for irregular particles at the forwards scattering regime but, poor agreement at the side and backscattering regime. The light scattering inferred sizes obtained by applying the Guinier analysis to the measured light scattering data were compared with the intensity weighted size distributions. The comparison showed that Guinier's analysis of light scattering yields intensity weighted mean sizes of reasonable accuracy for any shape and refractive index. This highlighted the implications of intensity weighting of the size distributions. Most importantly, this intensity weighting demonstrated the contributions of larger particle size presented in the scattering volume to the total scattered intensity. This implies that using a number distribution determined from an APS or similar aerosol measuring instrument to determine the light scattering size could be fraught with error.

The light scattering results from non-fractal hematite and fractal soot aggregates showed an enhancement in the backscattering despite large values of the imaginary part of the refractive index. The backscattering enhancement in the non-fractal hematite aggregate was due to the internal multiple scattering between the grains within the aggregate. In addition, we presented dimensional analysis to estimate the extent of multiple scattering. We found a correlation between the average number of scattering events within the aggregate and the enhancement in the backscattering. In contrast, a similar analysis for soot particles did not show the enhancement. The backscattering enhancement in the soot might be due to water-coated, dense soot, as suggested by TEM pictures. For the dense soot, the total scattering could be contributed by inter-cluster in addition to intra-cluster multiple scattering. Furthermore, many parameters are needed to characterize the soot particle: aggregate size, monomer size, pre-factor, number of monomers presented in the aggregate, and fractal dimension. So, one needs to specify all these parameters to compare the experimentally measured light scattering result with the theoretical calculations. Thus, accurately determining each parameter involved in the calculations is of utmost importance. Overall, experimentally measured enhancement in the backscattering would require more considera-

tion of theoretical and experimental work.

We also demonstrated sensitivity of backscattering with particles' shape, size, and refractive index. Although there was a perfect agreement on the forward scattering regime, there is still a significant disagreement on the side and backscattering regime. Therefore, we proposed that to measure the backscattering, one needs to measure the forward scattering simultaneously to determine the Guinier inferred size for characterizing atmospherically available particles.

The setup used throughout this dissertation consists of three separate optical arrangements and two 16-channel detectors. The scattered light was collected at 31 different channels simultaneously but 45 channels overall. In the future, we can add another detector so that scattered light could be collected in 45 different channels simultaneously. Moreover, we could replace the forward detector by replacing the current 16 channels detector by a detector with 512 channels that would allow the detection of the scattered light even smaller than the smallest forward scattering angle of 0.32° with higher resolution. That would provide more data points for Guinier's analysis to apply and characterize the larger size particles more precisely.

Furthermore, we could replace the off-axis parabolic mirror with a beam splitter that would allow us to get to exactly 180° but this also incurs the problem of the laser beam spots on the beam splitter. These can be bright enough to overwhelm the backscattering. Additionally, single-particle scattering could be measured by replacing the currently used detectors with highly sensitive detectors. We can use a photomultiplier (PMT) tube at an angle of around $\simeq 12°$ to determine the absolute scattering cross sections. That will allow us to measure the absolute scattering by calibration with gases of known Rayleigh ratios which was previously done in our lab [129, 137, 174] following D'Alessio [174]. Calibration to obtain an absolute scattering cross section will give an unprecedented comparison to theory.

Once the setup built including, 180°, one could perform laboratory measurements of the scattering intensity I(θ), degree of linear polarization, P_l, linear depolarization ratio LDR,

μ_l, and other matrix elements for a wide range of particle types using an angular range of $\simeq 0.3°$ to $\simeq 180°$. The perfect backscattering (180°) linear depolarization ratio would be useful for the optical characterization of morphologically complex atmospheric particles that contain a variety of mineral dust, bioaerosols, pollen grains, soot particles, and interstellar dust particles. Despite significant advancements in theoretical work for understanding the linear depolarization ratio, lidar, and remote sensing, there is a dearth of laboratory data with which to vet the theory. Laboratory lidar measurements could answer the questions regarding aerosol like what kind, how distributed, and how it changes.

Bibliography

[1] John Tyndall. *Faraday as a Discoverer*. D. Appleton, 1868.

[2] John W Strutt. Xv. on the light from the sky, its polarization and colour. *The London, Edinburgh, and Dublin Philosophical Magazine and Journal of Science*, 41 (271):107–120, 1871.

[3] Gustav Mie. Beiträge zur optik trüber medien, speziell kolloidaler metallösungen. *Annalen der physik*, 330(3):377–445, 1908.

[4] M Kerker. The scattering of light and other electromagnetic radiation. *The scattering of light and other electromagnetic radiation*, 1969.

[5] Hendrik Christoffel Hulst and Hendrik C van de Hulst. *Light scattering by small particles*. Courier Corporation, 1981.

[6] Craig F Bohren and Donald R Huffman. Absorption and scattering of light by small particles. *Absorption and Scattering of Light by Small Particles*, page 544, 1998.

[7] Michael I Mishchenko, Larry D Travis, and Andrew A Lacis. *Scattering, absorption, and emission of light by small particles*. Cambridge university press, 2002.

[8] Michael I Mishchenko, Larry D Travis, and Andrew A Lacis. *Multiple scattering of light by particles: radiative transfer and coherent backscattering*. Cambridge University Press, 2006.

[9] Otto Kratky and Günther Porod. Röntgenuntersuchung gelöster fadenmoleküle. *Recueil des Travaux Chimiques des Pays-Bas*, 68(12):1106–1122, 1949.

[10] André Guinier, Gérard Fournet, and Kenneth L Yudowitch. Small-angle scattering of x-rays. 1955.

[11] Otto Glatter, Otto Kratky, and HC Kratky. *Small angle X-ray scattering*. Academic press, 1982.

[12] Stephen W Lovesey. Theory of neutron scattering from condensed matter. 1984.

[13] CM Sorensen and DJ Fischbach. Patterns in mie scattering. *Optics Communications*, 173(1-6):145–153, 2000.

[14] Matthew J Berg, Christopher M Sorensen, and Amit Chakrabarti. Patterns in mie scattering: evolution when normalized by the rayleigh cross section. *Applied optics*, 44(34):7487–7493, 2005.

[15] Christopher M Sorensen. Q-space analysis of scattering by particles: A review. *Journal of Quantitative Spectroscopy and Radiative Transfer*, 131:3–12, 2013.

[16] Prakash Gautam, Justin B Maughan, and Christopher M Sorensen. Q-space analysis of experimentally observed light scattering by hematite and molybdenum disulfide particles.

[17] Justin Birdwell Maughan. *Q-Space Analysis of the Orientationally Averaged Light Scattering by Particles*. Kansas State University, 2020.

[18] Craig F Bohren and Donald R Huffman. *Absorption and scattering of light by small particles*. John Wiley & Sons, 2008.

[19] Yuli Wang Heinson. *Light scattering studies of irregularly shaped particles*. Kansas State University, 2016.

[20] CM Sorensen. Light scattering by fractal aggregates: a review. *Aerosol Science & Technology*, 35(2):648–687, 2001.

[21] William R Heinson, Amitabha Chakrabarti, and Christopher M Sorensen. A new parameter to describe light scattering by an arbitrary sphere. *Optics Communications*, 356:612–615, 2015.

[22] CM Sorensen and D Shi. Guinier analysis for homogeneous dielectric spheres of arbitrary size. *Optics communications*, 178(1-3):31–36, 2000.

[23] William R Heinson, Amitabha Chakrabarti, and Christopher M Sorensen. Crossover from spherical particle mie scattering to circular aperture diffraction. *JOSA A*, 31 (11):2362–2364, 2014.

[24] Brendan M Heffernan, Yuli W Heinson, Justin B Maughan, Amitabha Chakrabarti, and Christopher M Sorensen. Backscattering measurements of micron-sized spherical particles. *Applied Optics*, 55(12):3214–3218, 2016.

[25] Prakash Gautam and Christopher M Sorensen. A wide range (0.32°–177.6°), multi-angle light scattering setup and concomitant analysis method. *Review of Scientific Instruments*, 92(11):113105, 2021.

[26] O Munoz, H Volten, JF De Haan, W Vassen, and JW Hovenier. Experimental determination of scattering matrices of olivine and allende meteorite particles. *Astronomy and Astrophysics*, 360:777–788, 2000.

[27] O Munoz, H Volten, JF De Haan, W Vassen, and JW Hovenier. Experimental determination of scattering matrices of randomly oriented fly ash and clay particles at 442 and 633 nm. *Journal of Geophysical Research: Atmospheres*, 106(D19):22833–22844, 2001.

[28] O Munoz, H Volten, JF De Haan, W Vassen, and JW Hovenier. Experimental determination of the phase function and degree of linear polarization of el chichon and pinatubo volcanic ashes. *Journal of Geophysical Research: Atmospheres*, 107(D13): ACL–4, 2002.

[29] O Munoz, H Volten, JW Hovenier, B Veihelmann, WJ Van Der Zande, LBFM Waters, and William I Rose. Scattering matrices of volcanic ash particles of mount st. helens, redoubt, and mount spurr volcanoes. *Journal of Geophysical Research: Atmospheres*, 109(D16), 2004.

[30] O Muñoz, H Volten, JW Hovenier, Timo Nousiainen, K Muinonen, D Guirado, F Moreno, and LBFM Waters. Scattering matrix of large saharan dust particles: Experiments and computations. *Journal of Geophysical Research: Atmospheres*, 112 (D13), 2007.

[31] O Muñoz, F Moreno, D Guirado, DD Dabrowska, H Volten, and JW Hovenier. The amsterdam–granada light scattering database. *Journal of Quantitative Spectroscopy and Radiative Transfer*, 113(7):565–574, 2012.

[32] O Muñoz, H Volten, JW Hovenier, M Min, Yu G Shkuratov, JP Jalava, WJ Van der Zande, and LBFM Waters. Experimental and computational study of light scattering by irregular particles with extreme refractive indices: hematite and rutile. *Astronomy & Astrophysics*, 446(2):525–535, 2006.

[33] H Volten, O Munoz, E Rol, JF De Haan, W Vassen, JW Hovenier, K Muinonen, and T Nousiainen. Scattering matrices of mineral aerosol particles at 441.6 nm and 632.8 nm. *Journal of Geophysical Research: Atmospheres*, 106(D15):17375–17401, 2001.

[34] H Volten, O Muñoz, JR Brucato, JW Hovenier, L Colangeli, LBFM Waters, and WJ Van der Zande. Scattering matrices and reflectance spectra of forsterite particles with different size distributions. *Journal of Quantitative Spectroscopy and Radiative Transfer*, 100(1-3):429–436, 2006.

[35] Arlon J Hunt and Donald R Huffman. A new polarization-modulated light scattering instrument. *Review of Scientific Instruments*, 44(12):1753–1762, 1973.

[36] Bernard W Bell and William S Bickel. Single fiber light scattering matrix: an experimental determination. *Applied Optics*, 20(22):3874–3876, 1981.

[37] Daniel B Curtis, Brian Meland, Murat Aycibin, Nathan P Arnold, Vicki H Grassian, Mark A Young, and Paul D Kleiber. A laboratory investigation of light scattering from representative components of mineral dust aerosol at a wavelength of 550 nm. *Journal of Geophysical Research: Atmospheres*, 113(D8), 2008.

[38] Brandon Redding, Yong-Le Pan, Chuji Wang, and Hui Cao. Polarization-resolved near-backscattering of airborne aggregates composed of different primary particles. *Optics Letters*, 39(14):4076–4079, 2014.

[39] Alain Miffre, Danaël Cholleton, and Patrick Rairoux. Laboratory evaluation of the scattering matrix elements of mineral dust particles from 176.0 up to 180.0-exact backscattering angle. *Journal of Quantitative Spectroscopy and Radiative Transfer*, 222:45–59, 2019.

[40] Christopher M Sorensen, Justin B Maughan, and Amitabha Chakrabarti. The partial light scattering cross section of spherical particles. *JOSA A*, 34(5):681–684, 2017.

[41] W Kim, CM Sorensen, and A Chakrabarti. Universal occurrence of soot superaggregates with a fractal dimension of 2.6 in heavily sooting laminar diffusion flames. *Langmuir*, 20(10):3969–3973, 2004.

[42] Wongyo Kim, Christopher M Sorensen, Danny Fry, and Amitabha Chakrabarti. Soot aggregates, superaggregates and gel-like networks in laminar diffusion flames. *Journal of aerosol science*, 37(3):386–401, 2006.

[43] R Dhaubhadel, A Chakrabarti, and CM Sorensen. Light scattering study of aggregation kinetics in dense, gelling aerosols. *Aerosol Science and Technology*, 43(11): 1053–1063, 2009.

[44] Yuli Wang, Amitabha Chakrabarti, and Christopher M Sorensen. A light-scattering study of the scattering matrix elements of arizona road dust. *Journal of Quantitative Spectroscopy and Radiative Transfer*, 163:72–79, 2015.

[45] Prakash Gautam, Justin B Maughan, Jan Ilavsky, and Christopher M Sorensen. Light scattering study of highly absorptive, non-fractal, hematite aggregates. *Journal of Quantitative Spectroscopy and Radiative Transfer*, 246:106919, 2020.

[46] Prakash Gautam and Christopher M Sorensen. A light-scattering study of highly refractive, irregularly shaped mos2 particles. *Journal of Quantitative Spectroscopy and Radiative Transfer*, 242:106757, 2020.

[47] Fabio Ferri. Use of a charge coupled device camera for low-angle elastic light scattering. *Review of scientific instruments*, 68(6):2265–2274, 1997.

[48] Joshua A Hubbard. *A study of aerodynamic deaggregation mechanisms and the size control of nanoactive™ aerosol particles*. PhD thesis, Kansas State University, 2006.

[49] Eugene Hecht. Optics 4ed, 2002.

[50] C Oh and CM Sorensen. Scaling approach for the structure factor of a generalized system of scatterers. *Journal of Nanoparticle Research*, 1(3):369–377, 1999.

[51] Oleg Dubovik, Brent Holben, Thomas F Eck, Alexander Smirnov, Yoram J Kaufman, Michael D King, Didier Tanré, and Ilya Slutsker. Variability of absorption and optical properties of key aerosol types observed in worldwide locations. *Journal of the atmospheric sciences*, 59(3):590–608, 2002.

[52] Pramod Adhikari and John F Mejia. Influence of aerosols on clouds, precipitation and freezing level height over the foothills of the himalayas during the indian summer monsoon. *Climate Dynamics*, 57(1):395–413, 2021.

[53] Jasper F Kok, David A Ridley, Qing Zhou, Ron L Miller, Chun Zhao, Colette L Heald, Daniel S Ward, Samuel Albani, and Karsten Haustein. Smaller desert dust cooling effect estimated from analysis of dust size and abundance. *Nature Geoscience*, 10(4): 274–278, 2017.

[54] Pramod Adhikari and John F Mejia. Impact of transported dust aerosols on precipitation over the nepal himalayas using convection-permitting wrf-chem simulation. *Atmospheric Environment: X*, page 100179, 2022.

[55] Haley E Redmond, Kathy D Dial, and Jonathan E Thompson. Light scattering and absorption by wind blown dust: Theory, measurement, and recent data. *Aeolian research*, 2(1):5–26, 2010.

[56] Daniel A Lack, Edward R Lovejoy, Tahllee Baynard, Anders Pettersson, and AR Ravishankara. Aerosol absorption measurement using photoacoustic spectroscopy: Sensitivity, calibration, and uncertainty developments. *Aerosol science and technology*, 40 (9):697–708, 2006.

[57] AR Beal and HP Hughes. Kramers-kronig analysis of the reflectivity spectra of 2h-mos2, 2h-mose2 and 2h-mote2. *Journal of Physics C: Solid State Physics*, 12(5):881, 1979.

[58] Chanyoung Yim, Maria O'Brien, Niall McEvoy, Sinéad Winters, Inam Mirza, James G Lunney, and Georg S Duesberg. Investigation of the optical properties of mos2 thin films using spectroscopic ellipsometry. *Applied Physics Letters*, 104(10):103114, 2014.

[59] Hui Zhang, Yaoguang Ma, Yi Wan, Xin Rong, Ziang Xie, Wei Wang, and Lun Dai. Measuring the refractive index of highly crystalline monolayer mos2 with high confidence. *Scientific reports*, 5(1):1–7, 2015.

[60] William C Hinds. *Aerosol technology: properties, behavior, and measurement of airborne particles*. John Wiley & Sons, 1999.

[61] Ian H Malitson. Interspecimen comparison of the refractive index of fused silica. *Josa*, 55(10):1205–1209, 1965.

[62] DL Jaggard, C Hill, RW Shorthill, D Stuart, M Glantz, F Rosswog, B Taggart, and S Hammond. Light scattering from particles of regular and irregular shape. *Atmospheric Environment (1967)*, 15(12):2511–2519, 1981.

[63] Michael I Mishchenko, Larry D Travis, Ralph A Kahn, and Robert A West. Modeling phase functions for dustlike tropospheric aerosols using a shape mixture of randomly oriented polydisperse spheroids. *Journal of Geophysical Research: Atmospheres*, 102 (D14):16831–16847, 1997.

[64] CM Sorensen, N Lu, and J Cai. Fractal cluster size distribution measurement using static light scattering. *Journal of Colloid and Interface Science*, 174(2):456–460, 1995.

[65] Paula K Hudson, Elizabeth R Gibson, Mark A Young, Paul D Kleiber, and Vicki H Grassian. Coupled infrared extinction and size distribution measurements for several clay components of mineral dust aerosol. *Journal of Geophysical Research: Atmospheres*, 113(D1), 2008.

[66] George Wang, Amitabha Chakrabarti, and Christopher M Sorensen. Effect of the imaginary part of the refractive index on light scattering by spheres. *JOSA A*, 32(7): 1231–1235, 2015.

[67] Christopher M Sorensen, Justin B Maughan, and Hans Moosmüller. Spherical particle absorption over a broad range of imaginary refractive index. *Journal of Quantitative Spectroscopy and Radiative Transfer*, 226:81–86, 2019.

[68] Yuli W Heinson, Amitabha Chakrabarti, and Christopher M Sorensen. A light-scattering study of al2o3 abrasives of various grit sizes. *Journal of Quantitative Spectroscopy and Radiative Transfer*, 180:84–91, 2016.

[69] CM Sorensen. Q-space analysis of scattering by dusts. *Journal of Quantitative Spectroscopy and Radiative Transfer*, 115:93–95, 2013.

[70] Irina N Sokolik and Owen B Toon. Incorporation of mineralogical composition into models of the radiative properties of mineral aerosol from uv to ir wavelengths. *Journal of Geophysical Research: Atmospheres*, 104(D8):9423–9444, 1999.

[71] Daniel P Veghte, Justin E Moore, Lasse Jensen, and Miriam Arak Freedman. Influence of shape on the optical properties of hematite aerosol. *Journal of Geophysical Research: Atmospheres*, 120(14):7025–7039, 2015.

[72] XL Zhang, GJ Wu, CL Zhang, TL Xu, and QQ Zhou. What is the real role of iron oxides in the optical properties of dust aerosols? *Atmospheric Chemistry and Physics*, 15(21):12159–12177, 2015.

[73] Konrad Kandler, Lothar Schütz, Carmen Deutscher, M Ebert, H Hofmann, S Jäckel, R Jaenicke, P Knippertz, K Lieke, A Massling, et al. Size distribution, mass concentration, chemical and mineralogical composition and derived optical parameters of the boundary layer aerosol at tinfou, morocco, during samum 2006. *Tellus B: Chemical and Physical Meteorology*, 61(1):32–50, 2009.

[74] Joseph M Prospero, Joanna E Bullard, and Richard Hodgkins. High-latitude dust over the north atlantic: inputs from icelandic proglacial dust storms. *science*, 335 (6072):1078–1082, 2012.

[75] A Banin, T Ben-Shlomo, L Margulies, DF Blake, RL Mancinelli, and AU Gehring. The nanophase iron mineral (s) in mars soil. *Journal of Geophysical Research: Planets*, 98(E11):20831–20853, 1993.

[76] Richard V Morris and Howard V Lauer Jr. Matrix effects for reflectivity spectra of dispersed nanophase (superparamagnetic) hematite with application to martian spectral data. *Journal of Geophysical Research: Solid Earth*, 95(B4):5101–5109, 1990.

[77] Jan Ilavsky, Fan Zhang, Ross N Andrews, Ivan Kuzmenko, Pete R Jemian, Lyle E Levine, and Andrew J Allen. Development of combined microstructure and structure characterization facility for in situ and operando studies at the advanced photon source. *Journal of applied crystallography*, 51(3):867–882, 2018.

[78] Hans J Herrmann. Geometrical cluster growth models and kinetic gelation. *Physics Reports*, 136(3):153–224, 1986.

[79] John David Jackson. Classical electrodynamics, 1999.

[80] Marvin R Querry. *Optical constants of minerals and other materials from the millimeter to the ultraviolet*. Chemical Research, Development & Engineering Center, US Army Armament ..., 1987.

[81] B Meland, PD Kleiber, VH Grassian, and MA Young. Visible light scattering study at 470, 550, and 660 nm of components of mineral dust aerosol: Hematite and goethite. *Journal of Quantitative Spectroscopy and Radiative Transfer*, 112(6):1108–1118, 2011.

[82] Justin B Maughan and Christopher M Sorensen. Application of the scaling approach to particles having simple, fundamental shapes, in the rayleigh–debye–gans diffraction limit. *Journal of Quantitative Spectroscopy and Radiative Transfer*, 222:190–195, 2019.

[83] Christopher M Sorensen, Yuli W Heinson, William R Heinson, Justin B Maughan, and Amit Chakrabarti. Q-space analysis of the light scattering phase function of particles with any shape. *Atmosphere*, 8(4):68, 2017.

[84] Yuriy Shkuratov, Sergey Bondarenko, Andrey Ovcharenko, Carle Pieters, Takahiro Hiroi, Hester Volten, Olga Muñoz, and Gorden Videen. Comparative studies of the reflectance and degree of linear polarization of particulate surfaces and independently scattering particles. *Journal of Quantitative Spectroscopy and Radiative Transfer*, 100 (1-3):340–358, 2006.

[85] Evgenij Zubko, Yuriy Shkuratov, Michael Mishchenko, and Gorden Videen. Light scattering in a finite multi-particle system. *Journal of Quantitative Spectroscopy and Radiative Transfer*, 109(12-13):2195–2206, 2008.

[86] Kari Lumme and Antti Penttilä. Model of light scattering by dust particles in the solar system: applications to cometary comae and planetary regoliths. *Journal of Quantitative Spectroscopy and Radiative Transfer*, 112(11):1658–1670, 2011.

[87] Victor P Tishkovets, Elena V Petrova, and Michael I Mishchenko. Scattering of electromagnetic waves by ensembles of particles and discrete random media. *Journal of Quantitative Spectroscopy and Radiative Transfer*, 112(13):2095–2127, 2011.

[88] Elena V Petrova and Victor P Tishkovets. Light scattering by aggregates of varying porosity and the opposition phenomena observed in the low-albedo particulate media. *Journal of Quantitative Spectroscopy and Radiative Transfer*, 112(13):2226–2233, 2011.

[89] Michael I Mishchenko, Li Liu, Daniel W Mackowski, Brian Cairns, and Gorden Videen. Multiple scattering by random particulate media: exact 3d results. *Optics Express*, 15(6):2822–2836, 2007.

[90] Michael I Mishchenko, Janna M Dlugach, Maxim A Yurkin, Lei Bi, Brian Cairns, Li Liu, R Lee Panetta, Larry D Travis, Ping Yang, and Nadezhda T Zakharova. First-principles modeling of electromagnetic scattering by discrete and discretely heterogeneous random media. *Physics Reports*, 632:1–75, 2016.

[91] Daniel W Mackowski and Michael I Mishchenko. A multiple sphere t-matrix fortran code for use on parallel computer clusters. *Journal of Quantitative Spectroscopy and Radiative Transfer*, 112(13):2182–2192, 2011.

[92] Tahereh Mokhtari, Christopher M Sorensen, and Amit Chakrabarti. Multiple-

scattering effects on static light-scattering optical structure factor measurements. *Applied optics*, 44(36):7858–7861, 2005.

[93] Bruce T Draine and Piotr J Flatau. Discrete-dipole approximation for scattering calculations. *Josa a*, 11(4):1491–1499, 1994.

[94] K Lumme and J Rahola. Light scattering by porous dust particles in the discrete-dipole approximation. *The Astrophysical Journal*, 425:653–667, 1994.

[95] Maxim A Yurkin and Alfons G Hoekstra. The discrete dipole approximation: an overview and recent developments. *Journal of Quantitative Spectroscopy and Radiative Transfer*, 106(1-3):558–589, 2007.

[96] PC Waterman. The t-matrix revisited. *JOSA A*, 24(8):2257–2267, 2007.

[97] MI Mishchenko. Light scattering by randomly oriented axially symmetric particles. *JOSA A*, 8(6):871–882, 1991.

[98] Michael I Mishchenko and Larry D Travis. T-matrix computations of light scattering by large spheroidal particles. *Optics communications*, 109(1-2):16–21, 1994.

[99] Dingeman J Wielaard, Michael I Mishchenko, Andreas Macke, and Barbara E Carlson. Improved t-matrix computations for large, nonabsorbing and weakly absorbing nonspherical particles and comparison with geometrical-optics approximation. *Applied optics*, 36(18):4305–4313, 1997.

[100] Michael I Mishchenko and Larry D Travis. Light scattering by polydisperse, rotationally symmetric nonspherical particles: Linear polarization. *Journal of Quantitative Spectroscopy and Radiative Transfer*, 51(5):759–778, 1994.

[101] Foeke Kuik, Johan F de Haan, and Joop W Hovenier. Single scattering of light by circular cylinders. *Applied optics*, 33(21):4906–4918, 1994.

[102] Alberto Mugnai and Warren J Wiscombe. Scattering from nonspherical chebyshev particles. 3: Variability in angular scattering patterns. *Applied optics*, 28(15):3061–3073, 1989.

[103] Tom Rother, Karsten Schmidt, Jochen Wauer, Valery Shcherbakov, and Jean-Francois Gayet. Light scattering on chebyshev particles of higher order. *Applied optics*, 45(23): 6030–6037, 2006.

[104] Ping Yang and Kuo-Nan Liou. Light scattering and absorption by nonspherical ice crystals. In *Light scattering reviews*, pages 31–71. Springer, 2006.

[105] Karri Muinonen, Evgenij Zubko, Jani Tyynelä, Yurij G Shkuratov, and Gorden Videen. Light scattering by gaussian random particles with discrete-dipole approximation. *Journal of Quantitative Spectroscopy and Radiative Transfer*, 106(1-3):360–377, 2007.

[106] Steven C Hill, A Clyde Hill, and Peter W Barber. Light scattering by size/shape distributions of soil particles and spheroids. *Applied optics*, 23(7):1025–1031, 1984.

[107] Matthew J Berg, Yuli W Heinson, Osku Kemppinen, and Stephen Holler. Solving the inverse problem for coarse-mode aerosol particle morphology with digital holography. *Scientific Reports*, 7(1):1–9, 2017.

[108] Justin Jacquot Kielar, Pascal Lemaitre, Carole Gobin, Wu Yingchun, Emmanuel Porcheron, Sebastien Coetmellec, Gerard Grehan, and Marc Brunel. Simultaneous interferometric in-focus and out-of-focus imaging of ice crystals. *Optics Communications*, 372:185–195, 2016.

[109] Matthew J Berg and Gorden Videen. Digital holographic imaging of aerosol particles in flight. *Journal of Quantitative Spectroscopy and Radiative Transfer*, 112(11):1776–1783, 2011.

[110] Ramesh Giri, Claudia Morello, Yuli W Heinson, Osku Kemppinen, Gorden Videen, and Matthew J Berg. Generation of aerosol-particle light-scattering patterns from digital holograms. *Optics Letters*, 44(4):819–822, 2019.

[111] M Kök. Abrasive wear of al2o3 particle reinforced 2024 aluminium alloy composites fabricated by vortex method. *Composites Part A: applied science and manufacturing*, 37(3):457–464, 2006.

[112] Roger J Perry, Arlon J Hunt, and Donald R Huffman. Experimental determinations of mueller scattering matrices for nonspherical particles. *Applied Optics*, 17(17):2700–2710, 1978.

[113] Owen B Toon and James B Pollack. A global average model of atmospheric aerosols for radiative transfer calculations. *Journal of Applied Meteorology and Climatology*, 15(3):225–246, 1976.

[114] Robert A West, Lyn R Doose, Andrew M Eibl, Martin G Tomasko, and Michael I Mishchenko. Laboratory measurements of mineral dust scattering phase function and linear polarization. *Journal of Geophysical Research: Atmospheres*, 102(D14):16871–16881, 1997.

[115] Foeke Kuik. Single scattering of light by ensembles of particles with various shapes. *Ph. D. Thesis*, 1992.

[116] Donald W Schuerman. *Light scattering by irregularly shaped particles*. Springer, 1980.

[117] Alberto Mugnai and Warren J Wiscombe. Scattering from nonspherical chebyshev particles. i: cross sections, single-scattering albedo, asymmetry factor, and backscattered fraction. *Applied optics*, 25(7):1235–1244, 1986.

[118] Miroslaw Jonasz and Georges Fournier. *Light scattering by particles in water: theoretical and experimental foundations*. Elsevier, 2011.

[119] Warren J Wiscombe and Alberto Mugnai. Scattering from nonspherical chebyshev particles. 2: Means of angular scattering patterns. *Applied Optics*, 27(12):2405–2421, 1988.

[120] Craig F Bohren and Shermila Brito Singham. Backscattering by nonspherical particles: A review of methods and suggested new approaches. *Journal of Geophysical Research: Atmospheres*, 96(D3):5269–5277, 1991.

[121] Tami C Bond and Robert W Bergstrom. Light absorption by carbonaceous particles: An investigative review. *Aerosol science and technology*, 40(1):27–67, 2006.

[122] Nicole AH Janssen, Gerard Hoek, Milena Simic-Lawson, Paul Fischer, Leendert Van Bree, Harry Ten Brink, Menno Keuken, Richard W Atkinson, H Ross Anderson, Bert Brunekreef, et al. Black carbon as an additional indicator of the adverse health effects of airborne particles compared with pm10 and pm2. 5. *Environmental health perspectives*, 119(12):1691–1699, 2011.

[123] Rituraj Niranjan and Ashwani Kumar Thakur. The toxicological mechanisms of environmental soot (black carbon) and carbon black: focus on oxidative stress and inflammatory pathways. *Frontiers in immunology*, 8:763, 2017.

[124] Jeff Tollefson. Soot a major contributor to climate change. *Nature News*, 15, 2013.

[125] Swarup China, Neila Salvadori, and Claudio Mazzoleni. Effect of traffic and driving characteristics on morphology of atmospheric soot particles at freeway on-ramps. *Environmental science & technology*, 48(6):3128–3135, 2014.

[126] Surabi Menon, James Hansen, Larissa Nazarenko, and Yunfeng Luo. Climate effects of black carbon aerosols in china and india. *Science*, 297(5590):2250–2253, 2002.

[127] Katherine M Manfred, Rebecca A Washenfelder, Nicholas L Wagner, Gabriela Adler, Frank Erdesz, Caroline C Womack, Kara D Lamb, Joshua P Schwarz, Alessandro

Franchin, Vanessa Selimovic, et al. Investigating biomass burning aerosol morphology using a laser imaging nephelometer. *Atmospheric chemistry and physics*, 18(3):1879–1894, 2018.

[128] Li Liu and Michael I Mishchenko. Effects of aggregation on scattering and radiative properties of soot aerosols. *Journal of Geophysical Research: Atmospheres*, 110(D11), 2005.

[129] CM Sorensen, J Cai, and N Lu. Light-scattering measurements of monomer size, monomers per aggregate, and fractal dimension for soot aggregates in flames. *Applied Optics*, 31(30):6547–6557, 1992.

[130] Daniel W Mackowski. A simplified model to predict the effects of aggregation on the absorption properties of soot particles. *Journal of Quantitative Spectroscopy and Radiative Transfer*, 100(1-3):237–249, 2006.

[131] Robert A West. Optical properties of aggregate particles whose outer diameter is comparable to the wavelength. *Applied optics*, 30(36):5316–5324, 1991.

[132] HX Zhang, CM Sorensen, ER Ramer, BJ Olivier, and JF Merklin. In situ optical structure factor measurements of an aggregating soot aerosol. *Langmuir*, 4(4):867–871, 1988.

[133] Michael I Mishchenko, Li Liu, and Daniel W Mackowski. T-matrix modeling of linear depolarization by morphologically complex soot and soot-containing aerosols. *Journal of Quantitative Spectroscopy and Radiative Transfer*, 123:135–144, 2013.

[134] CM Sorensen, J Cai, and N Lu. Test of static structure factors for describing light scattering from fractal soot aggregates. *Langmuir*, 8(8):2064–2069, 1992.

[135] JNCM Cai, N Lu, and CM Sorensen. Comparison of size and morphology of soot ag-

gregates as determined by light scattering and electron microscope analysis. *Langmuir*, 9(11):2861–2867, 1993.

[136] N Lu and CM Sorensen. Depolarized light scattering from fractal soot aggregates. *Physical Review E*, 50(4):3109, 1994.

[137] C Oh and CM Sorensen. Light scattering study of fractal cluster aggregation near the free molecular regime. *Journal of Aerosol Science*, 28(6):937–957, 1997.

[138] Christopher M Sorensen, Wongyo Kim, Dan Fry, Dan Shi, and Amitabha Chakrabarti. Observation of soot superaggregates with a fractal dimension of 2.6 in laminar acetylene/air diffusion flames. *Langmuir*, 19(18):7560–7563, 2003.

[139] Rajan K Chakrabarty, Hans Moosmüller, Mark A Garro, and Christopher B Stipe. Observation of superaggregates from a reversed gravity low-sooting flame. *Aerosol Science and Technology*, 46(1):i–iii, 2012.

[140] Matthew J Berg and Christopher M Sorensen. Internal fields of soot fractal aggregates. *JOSA A*, 30(10):1947–1955, 2013.

[141] Fengshan Liu, Jérôme Yon, Andrés Fuentes, Prem Lobo, Gregory J Smallwood, and Joel C Corbin. Review of recent literature on the light absorption properties of black carbon: Refractive index, mass absorption cross section, and absorption function. *Aerosol Science and Technology*, 54(1):33–51, 2020.

[142] Hans Moosmüller, Ramesh Giri, Christopher M Sorensen, and Matthew J Berg. Black metal nanoparticles from abrasion processes in everyday life: Bicycle drivetrains and rock-climbing ropes. *Optics Communications*, 479:126413, 2021.

[143] Ramin Dastanpour, Ali Momenimovahed, Kevin Thomson, Jason Olfert, and Steven Rogak. Variation of the optical properties of soot as a function of particle mass. *Carbon*, 124:201–211, 2017.

[144] Yuli W Heinson, Justin B Maughan, Jiachen Ding, Amitabha Chakrabarti, Ping Yang, and Christopher M Sorensen. Q-space analysis of light scattering by ice crystals. *Journal of Quantitative Spectroscopy and Radiative Transfer*, 185:86–94, 2016.

[145] Christopher B Stipe, Brian S Higgins, Donald Lucas, Catherine P Koshland, and Robert F Sawyer. Inverted co-flow diffusion flame for producing soot. *Review of scientific instruments*, 76(2):023908, 2005.

[146] Mohsen Kazemimanesh, Alireza Moallemi, Kevin Thomson, Greg Smallwood, Prem Lobo, and Jason S Olfert. A novel miniature inverted-flame burner for the generation of soot nanoparticles. *Aerosol Science and Technology*, 53(2):184–195, 2019.

[147] RA Dobbins and CM Megaridis. Morphology of flame-generated soot as determined by thermophoretic sampling. *Langmuir*, 3(2):254–259, 1987.

[148] Jason Olfert and Steven Rogak. Universal relations between soot effective density and primary particle size for common combustion sources. *Aerosol Science and Technology*, 53(5):485–492, 2019.

[149] Raymond D Mountain, George W Mulholland, and Howard Baum. Simulation of aerosol agglomeration in the free molecular and continuum flow regimes. *Journal of Colloid and Interface Science*, 114(1):67–81, 1986.

[150] Daniel W Mackowski. Electrostatics analysis of radiative absorption by sphere clusters in the rayleigh limit: application to soot particles. *Applied optics*, 34(18):3535–3545, 1995.

[151] MV Berry and IC Percival. Optics of fractal clusters such as smoke. *Optica Acta: International Journal of Optics*, 33(5):577–591, 1986.

[152] Raymond D Mountain and GW Mulholland. Light scattering from simulated smoke agglomerates. *Langmuir*, 4(6):1321–1326, 1988.

[153] Remi Jullien and Robert Botet. Aggregation and fractal aggregates. *Ann. Telecomm.*, 41:343–short, 1987.

[154] Christopher M Sorensen and Gregory C Roberts. The prefactor of fractal aggregates. *Journal of colloid and interface science*, 186(2):447–452, 1997.

[155] CM Sorensen, WB Hageman, TJ Rush, H Huang, and C Oh. Aerogelation in a flame soot aerosol. *Physical Review Letters*, 80(8):1782, 1998.

[156] CM Sorensen and WB Hageman. Two-dimensional soot. *Langmuir*, 17(18):5431–5434, 2001.

[157] D Fry, A Chakrabarti, W Kim, and CM Sorensen. Structural crossover in dense irreversibly aggregating particulate systems. *Physical Review E*, 69(6):061401, 2004.

[158] Daniel W Mackowski and Michael I Mishchenko. Calculation of the t matrix and the scattering matrix for ensembles of spheres. *JOSA A*, 13(11):2266–2278, 1996.

[159] Guillaume A D'Almeida, Peter Koepke, and Eric P Shettle. *Atmospheric aerosols: global climatology and radiative characteristics*. A Deepak Pub, 1991.

[160] Kirk A Fuller, William C Malm, and Sonia M Kreidenweis. Effects of mixing on extinction by carbonaceous particles. *Journal of Geophysical Research: Atmospheres*, 104(D13):15941–15954, 1999.

[161] Kenneth Sassen. The polarization lidar technique for cloud research: A review and current assessment. *Bulletin of the American Meteorological Society*, 72(12):1848–1866, 1991.

[162] Claus Weitkamp. *Lidar: range-resolved optical remote sensing of the atmosphere*, volume 102. Springer Science & Business, 2006.

[163] AA Kokhanovsky, AB Davis, B Cairns, O Dubovik, OP Hasekamp, I Sano, S Mukai, VV Rozanov, P Litvinov, T Lapyonok, et al. Space-based remote sensing of atmospheric aerosols: The multi-angle spectro-polarimetric frontier. *Earth-Science Reviews*, 145:85–116, 2015.

[164] Kenneth Sassen. Polarization in lidar. In *Lidar*, pages 19–42. Springer, 2005.

[165] Michael Kahnert and Emma Andersson. How much information do extinction and backscattering measurements contain about the chemical composition of atmospheric aerosol? *Atmospheric Chemistry and Physics*, 17(5):3423–3444, 2017.

[166] Romain Ceolato and Matthew J Berg. Aerosol light extinction and backscattering: A review with a lidar perspective. *Journal of Quantitative Spectroscopy and Radiative Transfer*, 262:107492, 2021.

[167] SR Pal and AI Carswell. Polarization properties of lidar backscattering from clouds. *Applied optics*, 12(7):1530–1535, 1973.

[168] Alain Miffre, Danaël Cholleton, Tahar Mehri, and Patrick Rairoux. Remote sensing observation of new particle formation events with a (uv, vis) polarization lidar. *Remote Sensing*, 11(15):1761, 2019.

[169] Albert Ansmann and Detlef Müller. Lidar and atmospheric aerosol particles. In *Lidar*, pages 105–141. Springer, 2005.

[170] Li Liu and Michael I Mishchenko. Spectrally dependent linear depolarization and lidar ratios for nonspherical smoke aerosols. *Journal of Quantitative Spectroscopy and Radiative Transfer*, 248:106953, 2020.

[171] Justin B Maughan, Christopher M Sorensen, and Amitabha Chakrabarti. Q-space analysis of light scattering by gaussian random spheres. *Journal of Quantitative Spectroscopy and Radiative Transfer*, 174:14–21, 2016.

[172] G Abbate, U Bernini, E Ragozzino, and F Somma. The temperature dependence of the refractive index of water. *Journal of Physics D: Applied Physics*, 11(8):1167, 1978.

[173] Alexey N Bashkatov and Elina A Genina. Water refractive index in dependence on temperature and wavelength: a simple approximation. In *Saratov Fall Meeting 2002: Optical Technologies in Biophysics and Medicine IV*, volume 5068, pages 393–395. SPIE, 2003.

[174] Antonio D'Alessio. Laser light scattering and fluorescence diagnostics of rich flames produced by gaseous and liquid fuels. In *Particulate Carbon*, pages 207–259. Springer, 1981.